

GROUND-BASED PHOTOMETRIC IMAGING OF LIGHTNING
EMP-INDUCED TRANSIENT LUMINOUS EVENTS

A DISSERTATION
SUBMITTED TO THE DEPARTMENT OF ELECTRICAL
ENGINEERING
AND THE COMMITTEE ON GRADUATE STUDIES
OF STANFORD UNIVERSITY
IN PARTIAL FULFILLMENT OF THE REQUIREMENTS
FOR THE DEGREE OF
DOCTOR OF PHILOSOPHY

Robert Troy Newsome

November 2010

© Copyright by Robert Troy Newsome 2011
All Rights Reserved

I certify that I have read this dissertation and that, in my opinion, it is fully adequate in scope and quality as a dissertation for the degree of Doctor of Philosophy.

(Umran Inan) Principal Adviser

I certify that I have read this dissertation and that, in my opinion, it is fully adequate in scope and quality as a dissertation for the degree of Doctor of Philosophy.

(Nikolai Lehtinen)

I certify that I have read this dissertation and that, in my opinion, it is fully adequate in scope and quality as a dissertation for the degree of Doctor of Philosophy.

(Sigrid Close
Aeronautics and Astronautics)

Approved for the University Committee on Graduate Studies

Abstract

With around 2000 thunderstorms active on the planet’s surface at any given time, lightning is one of Earth’s more prevalent natural phenomena. Each lightning return stroke radiates a wideband electromagnetic pulse (EMP), and it has long been known that fields radiated by lightning return strokes have far-reaching effects. In the Earth-ionosphere waveguide, lightning-radiated fields can propagate efficiently to great distances, being detectable at ranges in excess of several thousands of kilometers. Additionally, they can propagate through the magnetized plasma of the ionosphere and enter the magnetosphere as whistler-mode waves where they can interact with geomagnetically trapped charged particles in the Earth’s radiation belts.

In 1989, an entirely new class of lightning return stroke field effects was discovered in the form of large and brilliant but brief lightning-associated optical flashes in the upper atmosphere, collectively known as transient luminous events (TLEs). Elves, the most abundant kind of TLE, are rapidly expanding rings of light produced by lightning EMP-heating of the lower ionosphere. Centered above their parent lightning return strokes at 85–90 km altitudes, elves can expand to diameters of several hundreds of kilometers on sub-millisecond timescales. However, their very short lifetimes make elves difficult to observe, and most in-the-field studies of elves have featured instruments requiring manual triggering that allow for detailed study of captured events but necessarily involve high rates of missed detections.

In this work, we present three years of elve observations made by a new free-running (non-triggered), ground-based, high-speed photometric imaging instrument called PIPER. This instrument is unique among ground-based instruments in that it does not require triggering and can observe nearly all elve activity within its field of

view as it tracks a storm across the horizon over its several-hour lifetime. PIPER is a multi-wavelength, 64-anode photometer array composed of two horizontally-oriented and two vertically-oriented 16-anode photometer arrays. With a sampling rate of 25 kHz, the array provides ample time-resolution for resolving elves and adequate spatial resolution for discriminating elves from other transient optical phenomena (sprites, cloud flashes, meteors, etc.).

We develop an algebraic technique for reconstructing the geometry of a particular elve from its photometric array observation. We then present aggregate observations of elves from four different multi-week summer observation campaigns and investigate many features of bulk elve activity that have not hitherto been possible to investigate with previous data sets. These features include peak storm-time elve production rates, the storm-to-storm and within-storm variability in elve production rates, elve production probability dependence on lightning return stroke parameters and local time of night, and distributions of elve geometric parameters. We also present observations of an unusual (and very infrequently reported) category of elves we call “elve doublets” and interpret their causative mechanism in terms of the EMP radiated from compact intracloud discharges.

Acknowledgements

There are many people besides myself who deserve credit for the production of this dissertation. Before launching into the work itself, I would like to take a few pages to express my sincerest appreciation to them.

First and most of all, I would like to thank my advisor, Prof. Umran Inan, for welcoming me into the Very Low Frequency Group many years ago and for providing countless opportunities for research in the years that followed, often in far-away and interesting places. The contagious enthusiasm and energy, as well as excellence, with which Umran pursues his work has often made it easier for me to stay excited about my own work and see it through to the end. It has been a tremendous privilege and honor to work with him.

Additionally I would like to thank Dr. Nikolai Lehtinen and Prof. Sigrid Close for their time reading and reviewing this dissertation and Prof. John Gill for serving as the chair of my defense committee. Their input in these final stages of the Ph.D. has served to strengthen the quality of this dissertation. Moreover, in the wake of Umran's sabbatical this last year, Dr. Jack Doolittle and Dr. Dave Lauben have been generous in meeting with me weekly, reviewing my progress, and offering their insight on how best to wind down and finish my work. Their time and input has been greatly appreciated.

Working in the VLF Group at Stanford the past five years has been an extraordinary privilege and experience, and one that I will certainly never forget. There are a number of office- and lab-mates to whom I am deeply indebted for years of help and support. Chief among them is Dr. Robert Marshall. When I came into the VLF Group, he had just finished designing the PIPER instrument and graciously let me

help him build and deploy it in a variety of far-flung places, eventually culminating in this dissertation. He also taught me how to run observation campaigns and do field work and was endlessly patient in answering my questions as I got caught up to speed on a variety of topics. In recent years, Nick LaVassar has helped to shoulder much of the PIPER- and optics-related field work load, for which I am also very appreciative. My work has also benefitted from conversations and interactions with many other former and current VLF Group members, including (but not necessarily limited to) Dr. Toru Adachi, Dr. Brant Carlson, Forrest Foust, Dr. Morris Cohen, Prof. Robb Moore, Kevin Graf, Dr. Ryan Said, Dr. Max Klein, Ben Cotts, Dan Golden, Denys Piddychiy, Dr. Praj Kulkarni, and several others. Jeff Chang has been a great help with engineering work, especially relating to field work in Alaska and Antarctica. Dan Musetescu has helped manage all the data my field work generates, including help with the incredibly tedious task of plowing through terabytes of PIPER data looking for TLE signatures. I am extremely grateful to Shaolan Min and Helen Niu for all of their administrative support over the years.

Outside of Stanford, I would like to thank in particular those that hosted and assisted with the summer TLE observation campaigns that furnished the data on which this dissertation is based. Dr. Walt Lyons (FMA Research, Inc.) hosted us at the Yucca Ridge Field Site near Fort Collins, Colorado in 2007 (my first TLE observation campaign) and then graciously came back out of retirement from the TLE community to host us again in 2009. His passion for TLEs and meteorology is infectious, and I learned much about sprite-hunting just by watching him hunt sprites. In 2008, Prof. William Winn (New Mexico Tech) hosted me at Langmuir Laboratory atop the 10,000+ foot South Baldy Peak near Socorro, New Mexico. I am also grateful to Dr. Geoff McHarg (United States Air Force Academy) for lending me his high-speed camera (as well as his insight into making TLE observations) each summer.

Lastly, I would like to thank my family for their tremendous love, support, and encouragement throughout my life: my parents Creech and Jan and my brothers Paul and Daniel. I could not have asked for better people to be raised by and with. All of my life, they have been excited about what I was doing—even when they did not

fully understand what I was doing—just because it was I that was doing it. I am truly grateful; this work is dedicated to them.

ROBERT T. NEWSOME

Stanford, California

November 5, 2010

This work has been funded by a Texas Instruments Stanford Graduate Fellowship and Office of Naval Research Grants N00014-03-1-0333 and N00014-09-1-0443 to Stanford University. Construction of the PIPER instrument was funded by the High Frequency Active Auroral Research Projects Agency (HAARP) and the Defense Advanced Research Projects Agency (DARPA) under ONR Grants N00014-05-1-0854 and N00014-06-1-1036 to Stanford University.

Contents

Abstract	iv
Acknowledgements	vi
1 Introduction	1
1.1 The Near-Earth Electromagnetic Environment	2
1.1.1 The Atmosphere	3
1.1.2 The Ionosphere	5
1.1.3 The Magnetosphere	7
1.2 Lightning	8
1.2.1 Cloud-to-Ground Discharges	8
1.2.2 In-Cloud Discharges	12
1.3 Transient Luminous Events	14
1.3.1 Sprites	15
1.3.2 Elves	16
1.3.3 Jets	18
1.4 Review of Past Work	18
1.4.1 Observations	19
1.4.2 Modeling	21
1.5 Contributions of This Work	23
1.6 Thesis Organization	24
2 Elves	26
2.1 The Return Stroke Electromagnetic Pulse	26

2.1.1	Return Stroke Current Models	27
2.1.2	Radiated Fields: General Features	32
2.1.3	Radiated Fields: Model-Dependent Features	35
2.2	EMP Propagation in the Lower Ionosphere	38
2.3	Photon Production and Ionospheric Modification	47
2.4	Ionospheric Relaxation Chemistry	52
3	Photometric Imaging of Elves	59
3.1	The PIPER Instrument	59
3.1.1	The Photometric Imaging Concept	60
3.1.2	Instrument Details	61
3.1.3	Field of View	64
3.1.4	Example Data	65
3.2	High-Speed Imaging of Elves	70
3.3	Elve Photon Emission Profiles	72
3.4	Recovering Photon Emission Profiles	74
3.4.1	Approach	75
3.4.2	Noise Rejection	77
3.4.3	Summary	81
3.5	Practical Considerations in Profile Recovery	81
3.5.1	Inaccurately Known Viewing Geometry	82
3.5.2	Elevation Angle Estimation	84
3.5.3	Observable Sensitivity Analysis	86
3.6	Examples of Reconstructed Emission Profiles	87
4	Aggregate Elve Observations	90
4.1	Observation Campaigns	91
4.1.1	Equipment and Techniques	91
4.1.2	Yucca Ridge, 2007	93
4.1.3	Langmuir Lab, 2008	94
4.1.4	Yucca Ridge, 2009	95
4.1.5	Summary	95

4.2	Occurrence Maps	98
4.3	Occurrence Rates	100
4.4	Elve Activity vs. Local Time of Night	104
4.5	Elve Production Probability vs. Peak Current	107
4.6	Geometric Parameter Distributions	113
4.7	Conclusions	114
5	Elve Doublets	116
5.1	Introduction	116
5.2	Observations	116
5.2.1	Doublets in PIPER Data	117
5.2.2	The Fly’s Eye	122
5.2.3	Trans-Ionospheric Pulse Pairs	123
5.3	Investigation	124
5.3.1	Source Orientation	124
5.3.2	Multiple-Source Causative Mechanisms	125
5.3.3	Reflection Causative Mechanisms	126
5.3.4	Compact Intracloud Discharges	127
5.4	Summary	129
6	Summary and Suggestions for Future Work	131
6.1	Summary	132
6.2	Suggestions for Future Work	134
A	Photon Emission Profile Construction Details	136
A.1	Forming A	136
A.2	Forming D_u	140

List of Tables

1.1	Peak radiated electric field strengths	12
2.1	Return stroke current models	30
2.2	Inelastic electron-neutral collisions in the lower ionosphere	50
2.3	Photon production processes in the lower ionosphere	51
2.4	Collisional quenching processes in the lower ionosphere	51
3.1	Examples of reconstructed elve photon emission profiles	87
4.1	Summary of three years of elve observation campaigns	97
4.2	Peak elve occurrence rates at different time scales	103
4.3	Selection of the form of the peak current dependence	110
4.4	Elve production probability model parameters	111
5.1	Elve singlet and doublet observations by storm	119
5.2	Nominal elve separations in time for elve doublet events	120
5.3	Potential multiple-source causative mechanisms for elve doublets . . .	126

List of Figures

1.1	The near-Earth electromagnetic environment	2
1.2	The neutral atmosphere	4
1.3	The ionosphere	6
1.4	The thundercloud and lightning discharge	9
1.5	Transient luminous events	14
1.6	Sprite formation	16
1.7	Elve mechanism	17
2.1	Channel base current waveforms	28
2.2	Return stroke current models	31
2.3	Integration over return stroke channel current	36
2.4	Radiated E fields: TL model vs. MTLE model	39
2.5	Characteristic frequencies in the lower nighttime ionosphere	43
2.6	Refraction indices in the lower nighttime ionosphere	45
2.7	EMP propagation into the lower nighttime ionosphere	46
2.8	Rates of EMP-driven optical excitation and electron density modification	52
2.9	Simulated elve photon production and electron density modification	53
2.10	Five-species model of ionospheric chemistry	55
2.11	Altitude profiles of rates of ionospheric chemistry processes.	56
2.12	Ionospheric relaxation after an ionization event	57
2.13	Ionospheric relaxation after an attachment event	58
3.1	PIPER	60
3.2	Photometric imaging concept	61

3.3	PIPER instrument details	62
3.4	PIPER field of view definitions	65
3.5	Example PIPER data	67
3.6	Example video-rate camera data	68
3.7	More PIPER data examples	69
3.8	The photon delay effect	71
3.9	Photon delay effect in high speed imaging of elves	73
3.10	The photon emission profile of an elve	74
3.11	Formation of x , y , A , y_s , and A_s	75
3.12	Formation of region of interest maps	80
3.13	Definition of viewing geometry parameters	82
3.14	Viewing geometry sensitivity analysis	83
3.15	Estimating θ_0 from data	85
3.16	Observable sensitivity analysis	86
3.17	Examples of reconstructed elve photon emission profiles	88
4.1	Breakdown of PIPER elve observations by auxiliary measurements	96
4.2	Maps of elve activity during each campaign	99
4.3	Storm-time elve occurrence rates	101
4.4	Within-storm variability in the elve occurrence rate on August 2, 2008	103
4.5	Elve activity vs. local time of night	105
4.6	The logistic regression function	109
4.7	Elve production probability dependence on CG peak current	111
4.8	Modeled elve production probability dependence on CG peak current	112
4.9	Geometric parameter distributions	113
5.1	Another example of an elve doublet in PIPER data	117
5.2	Distributions of elve singlet and elve doublet counts per storm	118
5.3	Normalized VLF sferics associated with elve doublets	121
5.4	Possible observation of an elve doublet by the Fly's Eye instrument	122
5.5	IC production of elve doublets through ground reflection	128

A.1	Definition of viewing geometry parameters	137
A.2	Formation of x , y , A , y_s , and A_s	141

Chapter 1

Introduction

Contrary to most casual expectations, thunderstorms and lightning are among Earth's more frequently occurring phenomena. Lightning does not occur uniformly distributed over space and time but rather appears spatially and temporally clustered in regions of active thunderstorms. While it may take days for the next thunderstorm to pass through a casual observer's neighborhood (or years, in the case of the San Francisco Bay Area), at any given moment there are on average 2000 active thunderstorms on the surface of the planet [*Rakov and Uman, 2003*, p. 10], with ~ 45 lightning discharges striking the ground somewhere on the Earth each second [*Christian et al., 2003*]. Each lightning discharge radiates a wideband electromagnetic pulse (EMP), a portion of which propagates into upper atmosphere regions (the ionosphere) where it can interact with large populations of charged particles. When considered over the timescales of the lifetime of a thunderstorm, one would expect bulk lightning activity to play a significant role in the the dynamics of charged particle populations in the lower ionosphere.

Elves, a particular manifestation of the direct interaction between lightning and the lower ionosphere, were first discovered in the early 1990s. Elves are very rapidly expanding rings of light centered high above a lightning discharge at ionospheric altitudes, commonly accompanied by modification of the ionospheric electron density. While elves have been studied both from the ground and from space, most studies have focused on examining individual events or globally averaged trends. Due to

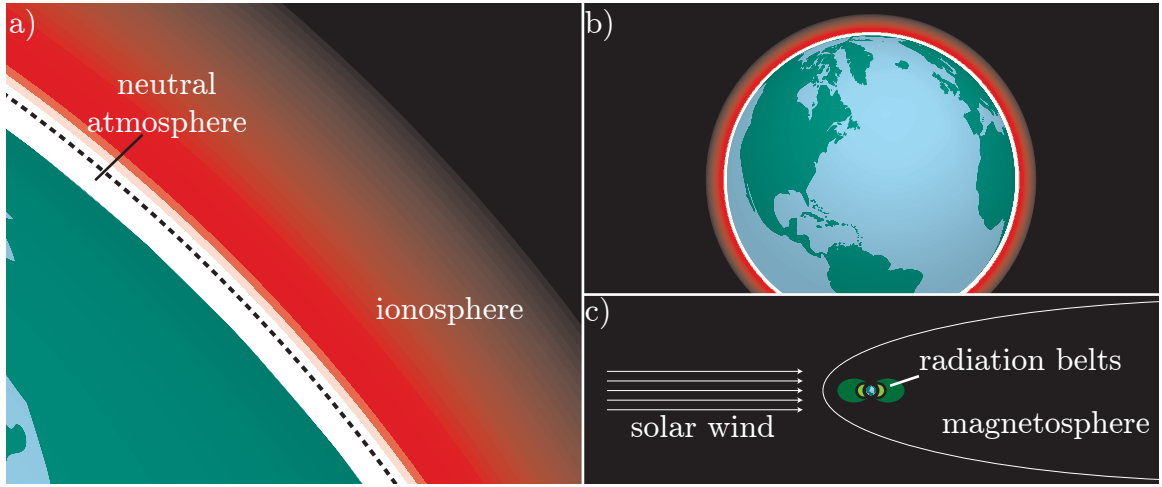


Figure 1.1: (a) The neutral atmosphere (0–100 km altitude, shown in white) and the ionosphere (100–1000 km, with electron density in shades of red) shown against the curvature of the Earth. (b) The Earth and its neutral atmosphere and ionosphere drawn radially to scale. (c) The Earth’s magnetosphere, with the magnetopause and radiation belts shown roughly to scale.

previous difficulties in imaging elves efficiently from a stationary point on the ground as a storm is tracked across the horizon, few studies have looked at aggregate elve behavior on a per-storm basis. In this work, we overcome these difficulties with a free-running, ground-based, photometric array approach to elve imaging and present three years of field observations and analysis of aggregate elve behavior on per-storm timescales.

1.1 The Near-Earth Electromagnetic Environment

In this chapter, we provide a brief and broad description of the context against which we set our work. We begin with a review of the near-Earth electromagnetic environment, including the neutral atmosphere, the ionosphere, and the magnetosphere. These regions are illustrated schematically (and roughly to scale) in Figure 1.1.

1.1.1 The Atmosphere

Although lightning-radiated electromagnetic waves do not significantly interact with the Earth's lower neutral atmosphere on their way to the ionosphere, we include its description here as an understanding of the neutral atmosphere aids in understanding the ionosphere (the outer, ionized portion of the atmosphere). The atmosphere extends from the Earth's surface out to several hundred kilometer altitudes and, for altitudes less than 100 km, is mostly composed of neutral particles. Considering the neutral temperature profile (Figure 1.2a, taken from the 1990 MSISE Atmosphere Model for a summer day in the United States Great Plains [[Hedin, 1991](#)]), we can divide the atmosphere into several layers:

1. the troposphere (0–15 km, characterized by temperatures decreasing with altitude) where all weather occurs, bounded above by the tropopause
2. the stratosphere (15–45 km, characterized by temperatures increasing with altitude) where the ozone layer takes up nearly all the incident solar extreme ultraviolet (EUV) radiation, bounded above by the stratopause
3. the mesosphere (45–90 km, characterized by temperatures again decreasing with altitude), bounded above by the mesopause
4. the thermosphere (>90 km, characterized by temperatures again increasing with altitude due to direct solar heating)

Below the mesopause, thermal gradients result in continual mixing of the constituent neutral species that compose the atmosphere so that the atmospheric composition is relatively constant with altitude (78% N₂, 21% O₂, 1% Ar). Near the mesopause, photodissociation of O₂ results in increased amounts of atomic oxygen O not found at lower altitudes (Figure 1.2b). It is primarily these species (N₂, O₂, and O) that participate in photon production in an elve. The neutral density profiles shown in Figure 1.2b are again taken from the 1990 MSISE Atmosphere Model for a summer day in the United States Great Plains.

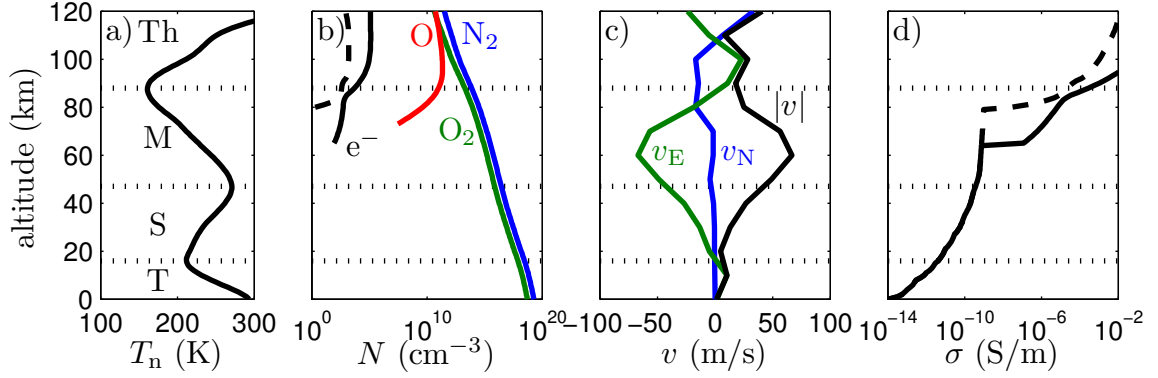


Figure 1.2: (a) Neutral $|v|$, v_E , v_W temperature profile, defining the troposphere (T), stratosphere (S), mesosphere (M), and thermosphere (Th). (b) Neutral density profiles and ionospheric electron density profiles (day is solid black, night is dashed black). (c) Neutral wind velocity profile, including the northward component (blue), the eastward component (green), and the magnitude (black). (d) Conductivity profile. All profiles are representative of summer nights at mid-latitudes in the northern hemisphere (i.e., the United States Great Plains region).

Unlike in the troposphere, where weather patterns drive neutral winds in a largely erratic and unpredictable way, the neutral winds at higher altitudes follow more predictable patterns amenable to modeling. We show the neutral wind velocity profile taken from the HWM93 model for a United States Great Plains summer day in Figure 1.2c [Hedin *et al.*, 1996]. In this geographic region of the summer mesosphere, there is a strong, prevailing neutral wind in the northwest direction with a speed around 70 m-s^{-1} . At the altitudes at which elves occur (80–90 km), the prevailing neutral wind speed is closer to 20 m-s^{-1} . A particle carried by the neutral wind at elve altitudes would take nearly 4 hours to cross a typical elve diameter of 250 km.

Even at low altitudes, the Earth’s nighttime atmosphere is not a perfect insulator. Continual ionization from cosmic rays and the Earth’s own radioactivity produce small background levels of ions and free electrons that give rise to the nonzero conductivity of the atmosphere. At these altitudes, high neutral densities mean short lifetimes for electrons, and the conductivity is primarily the result of ion conductivity. At higher altitudes (near the mesopause and above), the conductivity is dominated by the presence of large quantities of free electrons in the ionosphere and it sharply

increases relative to the conductivity at lower altitudes. Figure 1.2d shows the atmospheric conductivity profile, again for the United States Great Plains region on a summer day. The conductivity is a sum of the Hale model for ion conductivity at lower altitudes [Hale, 1984] and the electron conductivity contribution for free electron densities taken from the IRI-2001 Ionosphere Model at higher altitudes [Bilitza, 2001] (shown in Figure 1.2b). The sharp transition in conductivity at the base of the ionosphere forms the top “wall” of the so-called Earth-ionosphere waveguide (the other wall being the surface of the Earth itself). Electromagnetic waves with frequencies not high enough to easily penetrate the ionosphere propagate very efficiently in the region between these two walls. For reference, the conductivity of the Earth’s surface (often assumed to be a good conductor) is often taken to be $\sigma_E \simeq 10^{-3} \text{ S}\cdot\text{m}^{-1}$ [Rakov and Uman, 2003, p. 7].

1.1.2 The Ionosphere

At all altitudes in the Earth’s atmosphere, various ionization processes can produce populations of charged particles (ions and free electrons). At lower altitudes (<50 km), ionization is produced primarily from the Earth’s radioactivity and incoming cosmic rays, leaving negligibly small populations of charged particles in an otherwise neutral atmosphere. At higher altitudes, however, direct solar photoionization of atmospheric neutrals leads to significant populations of ions and free electrons that strongly interact with electromagnetic waves. This region (altitudes spanning 50 km out to the atmosphere’s poorly-defined outer edge) is called the ionosphere.

Above the mesopause, the thermal gradients that drive atmospheric mixing become less important and neutral constituents diffuse in altitude until they reach hydrostatic equilibrium. Thus, above the mesopause, atmospheric composition varies with altitude (with composition dominated by heavier molecules at lower altitudes and lighter atoms at higher altitudes) and different photochemical processes in turn dominate at different altitudes. This variation in photochemistry with altitude gives rise to the “layers” or “regions” of the ionosphere. The D-region features ionization

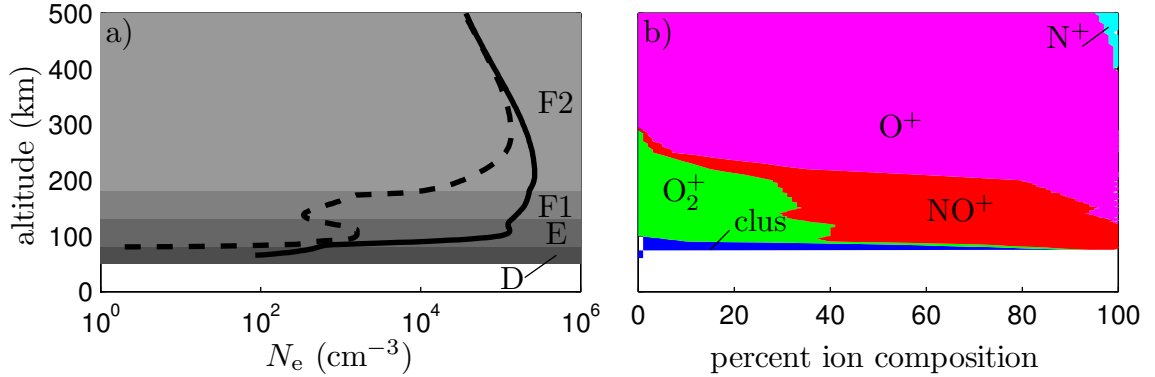


Figure 1.3: (a) Free electron density in the ionosphere at daytime (solid) and night-time (dashed line), with the D-, E-, F1-, and F2-layers highlighted. (b) Area graph of the ionospheric ion composition (by percent) at each altitude (i.e., at each altitude, the distribution of ions that make up the ionosphere at that altitude is shown).

of NO molecules as well as increased formation of negative ions through electron attachment to O and O_2 . The E-region features ionization of O atoms and O_2 and N_2 molecules to produce O^+ , O_2^+ , and N_2^+ ions. The F1- and F2-layers feature primarily ionization of O atoms to produce O^+ ions. The electron density as modeled by IRI-2001 for a summer day and night over the United States Great Plains regions is shown in Figure 1.3a.

Solar photoionization of the atmosphere maintains the charged particle populations of the ionosphere in the day. At night, recombination of ions and free electrons outpaces ionization and the populations of charged particles decrease, resulting in a nightly collapse of the ionosphere. In some layers (particularly the D- and F1-layers), the recombination rate is fast enough that the layer disappears altogether within a few hours after dusk. In other layers (the E-layer and especially the F2-layer), the recombination rate is slow enough that the layers persist through the night. We postpone a detailed review of D-region ionospheric chemistry until Section 2.4.

The state of the ionosphere is quite dynamic and can vary dramatically over different geographical regions and under different solar conditions. As the elve observation campaigns of this work were made in the United States Great Plains regions during the summers of the extended solar minimum of 2007-2009, we will only consider in

this work (unless otherwise noted) a mid-latitude summer ionosphere under quiet solar conditions.

1.1.3 The Magnetosphere

Beyond the Earth's atmosphere and ionosphere lies the magnetosphere, the region around the Earth in which charged particle motion and electromagnetic wave propagation are dominated by the Earth's geomagnetic field. The magnetosphere (whose boundary is defined by the transition to space dominated by the solar wind) is very large, extending to ~ 10 Earth radii in the sunward direction and several hundreds of Earth radii in the anti-sunward direction, and features large populations of energetic charged particles stably trapped in the Earth's magnetic field (the Van Allen radiation belts).

While this work is not directly concerned with the magnetosphere, there are a few magnetospheric phenomena which affect the Earth's D-region ionosphere worth noting. At high latitudes, geomagnetic storms can trigger auroral injection of high energy charged particles from the magnetosphere down into the lower ionosphere and atmosphere. In addition to producing brilliant displays of light (the northern and southern lights), collisions between these charged particles and atmospheric neutrals produce ionization, substantially changing the electron (and ion) density profile at the altitudes of interest in this work.

Of more interest at mid-latitudes are lightning-induced electron precipitation (LEP) events, which similarly increase the electron density profile of the lower ionosphere/upper atmosphere. Because the ionosphere is a magnetized plasma, a portion of the ELF/VLF wave energy in a lightning EMP leaks through the ionosphere and enters the magnetosphere as a whistler wave. Once in the magnetosphere, the whistler can undergo wave-particle interactions with the trapped radiation belt particles it encounters there, resulting in modification of their orbital trajectories and eventual "precipitation" into the upper atmosphere through gyroresonant pitch angle scattering. Once in the atmosphere, these high energy radiation belt particles increase the electron density profile through impact ionization with atmospheric neutrals. More

details on this phenomenon can be found in [Peter \[2007\]](#).

1.2 Lightning

Lightning has long been a subject of human fascination, but more recently in the last several hundred years, lightning has also become a subject of scientific inquiry. While our scientific understanding of the lightning discharge is still incomplete, much can now be said about the different kinds of lightning discharges and their morphological features. Broadly speaking, there are two categories of lightning: cloud-to-ground discharges (CGs) and in-cloud discharges (ICs).

Before giving a brief description of CGs and ICs, it is important to describe the nature of the thunderclouds that produce them. While variation from thundercloud to thundercloud is substantial, typical thunderclouds form at altitudes between ~ 5 and ~ 15 km. While the atmosphere in which thunderclouds form is electrically neutral, convective charge separation processes within a thundercloud are capable of maintaining layers of differently charged regions. A common model for the charge distribution within a thundercloud involves three vertically stacked charge layers: a main positive layer toward the top of the cloud, a main negative layer in the middle, and a smaller lower positive layer at the bottom (see Figure 1.4) [[Rakov and Uman, 2003](#), p. 68]. Sometimes, a thin fourth layer of screening negative charge at the very top of the cloud is also included. In real thunderclouds, the charge distribution can often be more complicated with additional layers and pockets of charge. However, all lightning-producing thunderclouds exhibit the same feature of separated regions of charge which drive strong electric fields (within the cloud, between clouds, and between the cloud and the ground) that aid in the initiation of lightning discharges. The discharges themselves act as the charge neutralization mechanism for the cloud.

1.2.1 Cloud-to-Ground Discharges

As cloud-to-ground discharges affect humans more directly than in-cloud discharges (and are easier to directly observe than in-cloud discharges), they have received more

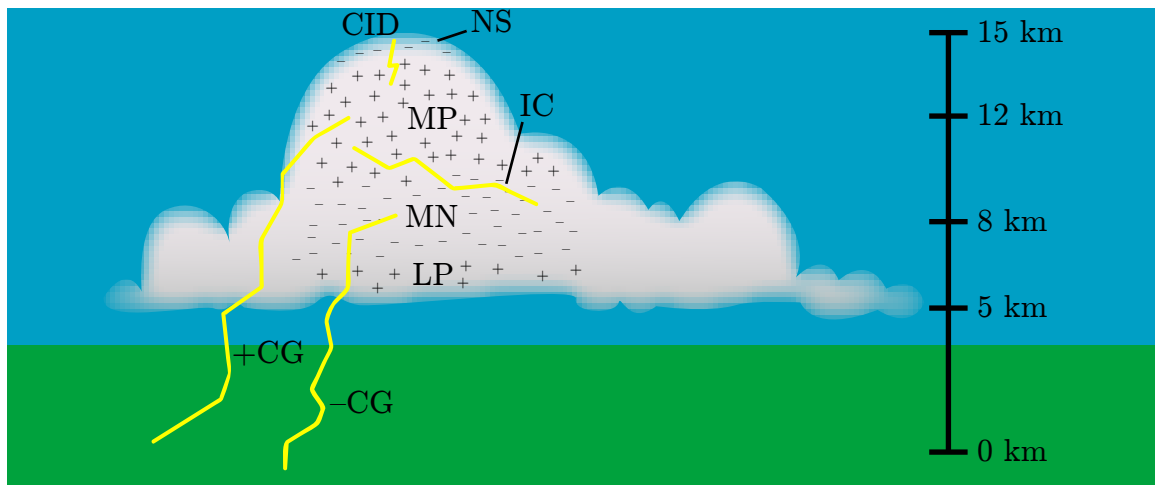


Figure 1.4: A cartoon showing various features of a thundercloud and its associated lightning discharges. Typical thundercloud charge layers include a negative screening (NS) layer at the top, a main positive (MP) layer above a main negative (MN) layer, and a smaller lower positive (LP) layer at the bottom. Negative and positive cloud-to-ground discharges ($-CGs$ and $+CGs$) remove charge from the MN and MP layers to ground. Most in-cloud discharges (ICs) form horizontally along the boundary of the MN layer, although compact intracloud discharges (CIDs) are oriented vertically near the top of the cloud.

attention from the scientific community and have been described more completely. Cloud-to-ground discharges can be labelled by the polarity of charge they effectively lower from the thundercloud to the ground: +CGs lower positive charge to the ground (more often, they actually raise negative charge from the ground to the cloud) while –CGs lower negative charge to the ground. In nature, –CGs are far more common (especially over oceans), making up around 90% of all CGs [*Rakov and Uman, 2003*, p. 4].

A typical –CG begins in the thundercloud with a poorly understood initiation event in the main negative charge layer which triggers the development of a “leader” out of the cloud toward the ground below. The leader is an electrically conductive channel formed in the neutral air that is connected back to the thundercloud charge reservoir. Leaders are self-propagating: as they form, charge from the thundercloud above moves down the channel and is deposited along the leader, raising the electric field ahead of the leader high enough to ionize the neutral air and extend the leader channel further downward. As the leader propagates, it branches often and appears as a slowly extending fan of conductive channels emanating from the cloud. As one of these channels nears the large reservoir of charge on the ground, a second leader begins propagating upward from the ground to meet it.

When the two leaders attach, they form a low-resistance conducting channel from the thundercloud to the ground and all the charge deposited in the leader channels begins moving rapidly along it. This part of the lightning discharge, dubbed the “return stroke”, is the most violent part of the the discharge and is responsible for most of the human injury and property damage caused by lightning. The return stroke delivers a very large electric current from the cloud to the ground very quickly, rapidly heating the conductive channel along which it moves and efficiently launching an electromagnetic wave (the EMP) as well as an acoustic shock wave (thunder). After the return stroke, there may be subsequent leader formations along the same decaying channels that initiate subsequent return strokes. Most multiple-return-stroke –CGs involve 3 to 5 return strokes, but –CG discharges with up to 26 return strokes have been recorded [*Rakov and Uman, 2003*, p. 190]. The human eye is not capable of registering the discrete return stroke events and sees the entire process (multiple

return strokes and all) as a single discharge (although discharges featuring very many return strokes may appear to the eye to flicker to some degree).

The differences between $-CGs$ and $+CGs$ are more than just the polarity of the charge lowered to the ground. While $-CGs$ typically lower negative charge from the main negative charge layer of a thundercloud to ground through possibly multiple return strokes, $+CGs$ lower positive charge from the main positive charge layer to ground through usually a single return stroke. Often, the single $+CG$ return stroke features an additional post-stroke continuing current that persists for tens to hundreds of millisecond and facilitates removal of large quantities of charge from the cloud. For this reason, and because the main positive charge layer sits toward the top of most thunderclouds, $+CGs$ can achieve much larger return-stroke peak currents and thundercloud charge moment changes than $-CGs$. However, because positive charge in the main positive charge layer is more easily neutralized through in-cloud discharges between the main positive and negative layers rather than through $+CG$ discharges, $+CGs$ occur much less frequently than $-CGs$. There are some particular types of thunderstorms, however, which exhibit non-typical charge structures that readily produce $+CGs$. Mesoscale convective systems (MCSs), for instance, typically have a low-altitude main positive charge layer below the main negative charge layer and are frequently associated with $+CG$ and sprite production [[Williams, 1998](#)].

The EMP radiated by a lightning return stroke (which can produce an elve at ionospheric altitudes if strong enough) propagates efficiently in the waveguide formed by the conducting Earth and the ionosphere. At great distances along the ground, the propagating EMP is often called a “sferic” (short for “atmospheric”); at high altitudes it is simply called an EMP. The peak strength of the electric field in a sferic is well correlated with the peak current in the lightning return stroke. [Krider \[1992\]](#) showed that $E_{100} \simeq 0.3I_p$ for a return stroke with a front speed of half the speed of light, where E_{100} is the peak electric field at 100 km distance along the ground (measured in $V\cdot m^{-1}$) and I_p is the peak electric current in the lightning return stroke (measured in kA). [Table 1.1](#) shows the E_{100} values for a number of different return stroke peak currents. At higher altitudes, E_{100} values decrease relative to E_{100} values on the ground. We expand greatly on this topic in [Section 2.1](#).

Table 1.1: Peak radiated electric field strengths for lightning return strokes of various peak current magnitudes, and the percentage of return strokes exceeding these magnitudes (from Tables 4.4 and 5.1 of [Rakov and Uman \[2003\]](#)).

I_p (kA)	E_{100} (V-m ⁻¹)	exceeded by
5	1.5	95% of +CGs
15	4.5	95% of −CGs
30	9	50% of −CGs
35	10.5	50% of +CGs
80	24	5% of −CGs
250	75	5% of +CGs

1.2.2 In-Cloud Discharges

While ICs occur much more often than CGs, they are also much more difficult to observe directly. Conventional approaches to studying CGs rely on combining radio observations (providing an electromagnetic view of the channel development) with photographic documentation of the physical channel development. As most of an IC discharge occurs deep within a thundercloud, photographic observation of IC channel formation and structure is rare. Most of our scientific understanding of ICs results only from remote electric and magnetic field observations during an IC discharge. Moreover, from the point of view of an IC discharge as an “electrodeless” discharge (as opposed to a CG discharge), it is not surprising that ICs exhibit a large degree of variability in their spatial structure and form. This makes it more difficult to apply *a priori* assumptions about channel shape and orientation in interpreting remote field observations.

Nevertheless, study of the remote fields produced by ICs does shed light on their physical nature. Most ICs exhibit two stages. In the first stage (called the “active” stage), breakdown events similar to those that start −CGs begin near the lower or upper boundary of the thundercloud’s main negative charge layer. A stepped leader carries negative charge into a positive charge region. The leader may propagate vertically (often upwards) or horizontally or a combination of the two. Eventually, the newly formed channel loses contact with its source reservoir of negative charge and the first stage ends. The second stage (the “final” stage) is characterized by a

redistribution of charge from deeper in the source charge region toward the former channel’s point of origin. This view of an IC can be thought of as a small, inverted CG without a return stroke (with the in-cloud positive charge region playing the role of the ground). It has been noted that ICs in small, developing storms seem to be predominantly vertically oriented while ICs in large, aged storm systems seem to be predominantly horizontally oriented [*Liu and Krehbiel, 1985*].

The leader channel that forms during an IC can reach several to tens of kilometer lengths over the course of its several hundred millisecond lifetime. As there is no return stroke process associated with ICs, the radiated fields are typically not as strong as those radiated by CGs. Most of the radiated field frequency content is in the VHF–UHF portion of the spectrum due to the short size of the leader steps.

Compact Intracloud Discharges

The active stage of an IC discharge typically radiates stronger electromagnetic fields than the final stage, albeit the fields radiated from an IC discharge are usually not as strong as those radiated by a CG return stroke. There is, however, a less common class of discharge within the active stage of an IC that radiates strong electromagnetic fields over a wide frequency range which is of particular interest in this work. These discharges were initially labelled “narrow bipolar pulses” (NBPs) or “narrow bipolar events” (NBEs) due to the shape of the electric field waveform measured in association with them [*Willett et al., 1989*], but in this work we prefer the use of the term “compact intracloud discharges” (CIDs) to distinguish the causative discharge from the mere description of the fields it can produce on the ground at some distances.

CIDs are among the strongest sources of RF radiation in thunderstorm environments [*Vine, 1980*], radiating 10 times more strongly in the VHF band than other lightning processes [*Smith et al., 1999*]. Even at VLF/LF frequencies, CID-radiated fields strengths are comparable to those of CG return strokes [*Nag et al., 2010*]. CID spatial scales are estimated to be 300 m to 3 km and vertically oriented [*Smith et al., 1999; Eack, 2004; Hamlin et al., 2007*] at in-cloud altitude of 6 km to 15 km [*Light and Jacobson, 2002*] or higher [*Nag et al., 2010*]. CIDs typically make up about 1%

of all lightning activity [*Lapp and Saylor, 2007*], but at least one compact storm in the United States Great Plains region has been observed to produce CIDs at rates as high as 92 CID-min^{-1} [*Suszcynsky and Lay, 2009*].

1.3 Transient Luminous Events

Until recently, it was thought that the dazzling display of light offered by a thunderstorm was confined to the lightning activity in the thunderstorm clouds and between the clouds and the ground. This understanding changed in 1989 with the first scientific documentation of a brilliant optical flash well above a thunderstorm [*Franz et al., 1990*], following years of intermittent but persistent verbal reports of such high-altitude flashes by pilots and others [*Vaughan and Vonnegut, 1989*, and references therein]. Publication of the photograph of the flash stoked a great amount of scientific interest in the subject of lightning-associated high-altitude (above cloud) flashes, and within a few years a menagerie of different kinds of flashes were discovered. The different kinds of flashes were given fanciful names like “sprites” and “elves” to reflect their fleeting and hard-to-catch nature (and to steer clear of names suggesting causative mechanisms which had not yet been pinned down) [*Sentman et al., 1995*], and the entire category of flashes came to be known as Transient Luminous Events (TLEs). Examples of various kinds of TLEs are shown in Figure 1.5.

In this work, we are mainly concerned with elves, but we provide here a brief summary of all TLEs. We present them in the order in which they were first experimentally discovered.

1.3.1 Sprites

Sprites are large, brief, and often highly-structured bursts of light occurring high above thunderstorms in response to CGs that remove large amounts of charge from the upper portions of the cloud [*Boccippio et al., 1995*]. A single sprite can span altitudes from 50 km up to 90 km [*Sentman et al., 1995*], with a width more than ten kilometers at its widest point [*Lyons, 1994*]. Often, the highest parts of a sprite

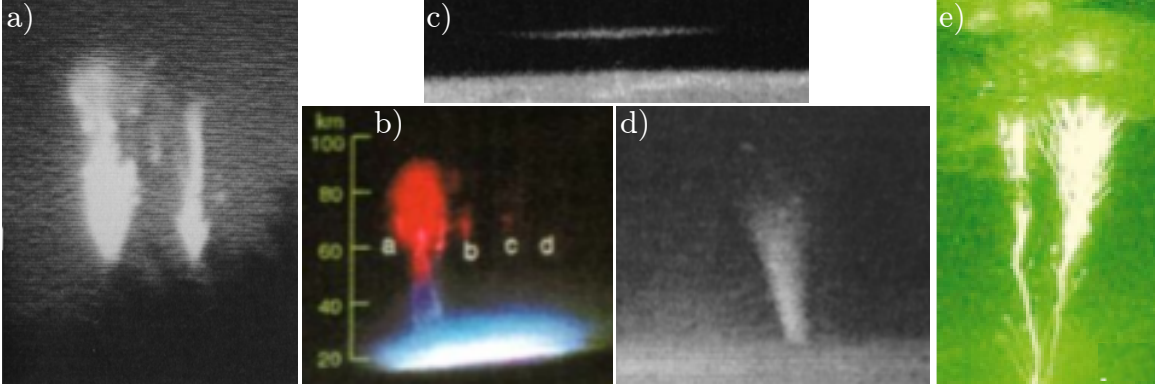


Figure 1.5: Examples of various transient luminous events: (a) the first recorded sprite (from Figure 1 of [Franz *et al.*, 1990]), (b) the first color recording of a sprite (from Figure 1 of [Sentman *et al.*, 1995]), (c) the first recorded elve (from Figure 2 of [Boeck *et al.*, 1992]), (d) a jet (from Figure 3 of [Wescott *et al.*, 1995]), (e) the first recording of a rare gigantic jet (from Figure 2 of [Pasko *et al.*, 2002])

feature a diffuse, red glow (called a halo) [Barrington-Leigh *et al.*, 2001] while the lower parts of a sprite feature highly structured streamers of a blue color [Gerken *et al.*, 2000]. However, halos can appear without streamers and streamers can appear without halos. Sprites occur as a response to intense cloud-to-ground discharges and may appear displaced up to 100 km and 100s of milliseconds from their causative CGs. Sprites last for several milliseconds to several tens of milliseconds, long enough to be barely perceptible to the human eye. The first published photograph of a sprite is shown in Figure 1.5a, and the first color photograph of a sprite is shown in Figure 1.5b.

The theory of sprite formation was first proposed by Wilson [1924] and is well described by Pasko *et al.* [1997]; we present only a sketch of it in Figure 1.6. Sprite initiation is directly associated with the magnitude of the change in the thundercloud charge moment achieved by a cloud-to-ground lightning discharge. In Figure 1.6, we consider two CGs: the first removes 10 C of charge from the cloud at a 5 km altitude while the second removes 50 C of charge from the cloud at a 12 km altitude. When a CG alters a thundercloud's charge configuration, it sets up a quasi-electrostatic field in the vicinity of the cloud (denoted by the quasi-electrostatic field profiles E_1 and E_2 in Figure 1.6) to which free charges in the upper atmosphere may respond.

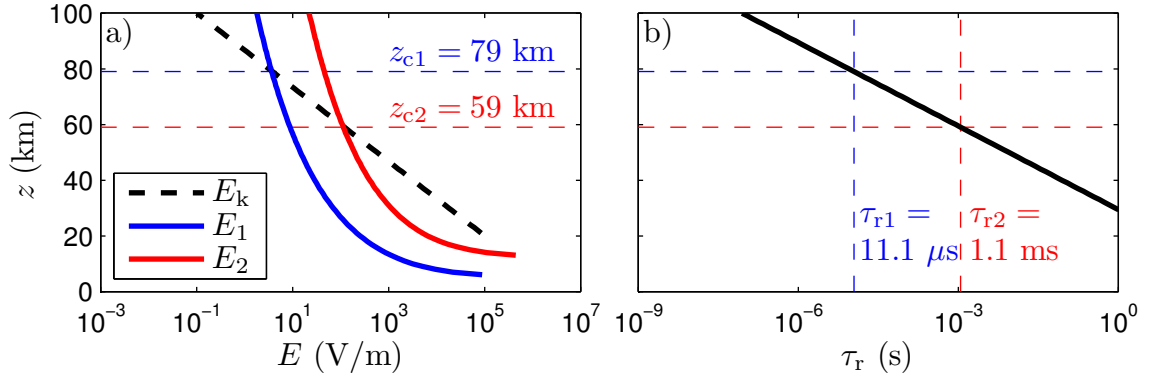


Figure 1.6: A sketch of the mechanism for sprite initiation. (a) Quasi-electrostatic field profiles setup up by CGs that remove 5 C from 5 km altitude (E_1) and 50 C from 12 km altitude (E_2), along with the atmospheric breakdown electric field threshold (E_k). (b) Associated electrostatic field relaxation time constants for each CG at the CG's critical altitude (where the electrostatic field initially exceeds the breakdown field threshold).

At all altitudes, the quasi-electrostatic field strength relaxes exponentially (with a time constant τ_r inversely proportional to the conductivity at that altitude) as free charges respond to the field (Figure 1.6b). In the stratosphere above the cloud, the conductivity is low and the quasi-electrostatic field is long-lasting (τ_r is large). At high altitudes (especially at ionospheric altitudes), the conductivity is high and the quasi-electrostatic field is screened out very quickly (τ_r is small).

The initial strength of the quasi-electrostatic dipole field falls off with altitude z as z^{-3} . Meanwhile, the atmospheric breakdown field threshold (E_k , which is proportional to atmospheric density) falls off exponentially with altitude (ultimately more quickly than the quasi-electrostatic field). Thus, there is a critical altitude beyond which the quasi-electrostatic field strength initially exceeds the atmospheric breakdown threshold (denoted by z_{c1} and z_{c2} for the two CGs of Figure 1.6). If the charge moment change is small, this altitude is very high and free charges screen the field almost as quickly as it appears. But if the charge moment change is large, the critical altitude is in the mesosphere, where lower conductivity allows the field to persist long enough to drive breakdown and initiate streamers, which give rise to the visible sprite phenomena.

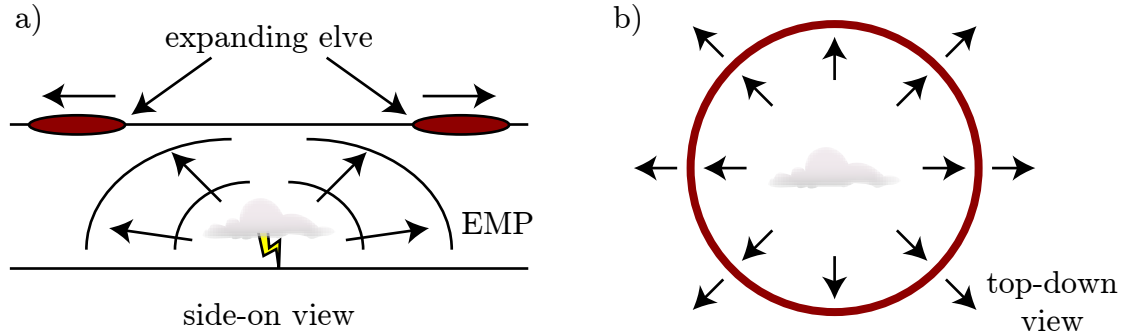


Figure 1.7: (a) Side-on view of a lightning return stroke producing an expanding EMP which in turn produces an elve as it encounters the bottom edge of the D-region ionosphere. (b) Top-down view of the same thing.

1.3.2 Elves

Elves are rapidly expanding rings of light centered well above a causative CG return stroke: where CG-producing thunderclouds reach altitudes of ~ 15 km, the elves that result from CGs appear at the base of the ionosphere at altitudes of 80–90 km. Primarily red in color [Taratenko *et al.*, 1992], elves expand radially outward with an apparent speed faster than light and can attain diameters several hundreds of km across on timescales faster than 1 ms [Inan *et al.*, 1996]. Figure 1.7 shows side-on and top-down schematic views of an expanding elve in relation to its causative CG. The first observed elve is shown in Figure 1.5c.

Elves result from EMP-heating of free electrons in the lower ionosphere [Inan *et al.*, 1991; Taratenko *et al.*, 1993a,b]. As the EMP radiated by a CG return stroke enters altitudes of the lower ionosphere where significant populations of free electrons can be found, the energy carried in the EMP is partially transferred to the free electrons through electron heating (i.e., increasing of the mean kinetic energy of the free electron population through field-driven acceleration). As the neutral density at these altitudes is still large relative to the electron density, the newly acquired kinetic energy acquired by the electrons is further transferred to atmospheric neutrals through electron-neutral collisions, resulting in significant populations of neutrals in non-ground energy states due to electron impact excitation. As these neutrals relax,

they produce photons which make up the elve. Because the cooling rates of heated electrons is very fast (on the order of microseconds), the entire process (EMP to heated electrons to excited neutrals to photon production) is nearly instantaneous on the timescale in which the EMP passes through the region [[Taranenko et al., 1993a](#)], and the optical phenomena of the elve can be interpreted as a direct signature of the EMP interaction with the ionosphere. Most of the photons produced by this mechanism are from the first positive band of molecular nitrogen (N_2 1P), although other optical bands (N_2 2P, N_2^+ 1N, N_2^+ Meinel, O_2^+ 1N) also play a role [[Taranenko et al., 1993b](#)].

We offer an expanded review of theoretical and experimental work done on elves later in this chapter (Section 1.4) and a detailed description of their causative mechanism in Chapter 2.

1.3.3 Jets

Where sprites and elves are directly caused by (but distinct from) lightning, jets could be considered simply to be an unusual kind of lightning. Jets are associated with upward-directed lightning rising out of cloud tops into the clear air above, and they vary greatly in size. Blue in color, the smallest jets are called blue starters and extend only a few kilometers from the cloud top into the clear air above [[Wescott et al., 1996](#)]. Blue jets (as distinct from blue starters) extend much further into the stratosphere (to altitudes in the neighborhood of 40 km) and have a conical shape [[Wescott et al., 1995](#)]. Both starters and jets occur relatively frequently (around the same rate as sprites). Gigantic jets, which reach altitudes as high as 80 km and establish a direct electrical condition between a thundercloud and the ionosphere [[Pasko et al., 2002](#)], appear to occur much less often. In a recent three-year satellite study of TLEs where over 5000 elves and around 600 sprite were observed, only 13 gigantic jets were observed, predominantly over oceans [[Chen et al., 2008](#)].

A photograph of one of the first observed jets is shown in Figure 1.5d, and the first photographed gigantic jet is shown in Figure 1.5e. We refer the reader interested in further details on blue starters, blue jets, and gigantic jets to the review paper by

Pasko [2008].

1.4 Review of Past Work

In this section, we provide a review of past work on elves, including both observational efforts and development of the theory behind them.

1.4.1 Observations

The first theoretical suggestion of the elve phenomenon actually preceded the first observations. *Inan et al.* [1991], in investigating perturbations of VLF signals along VLF transmitter-receiver paths in direct response to cloud-to-ground lightning events [*Inan et al.*, 1988], hypothesized the lightning EMP-heating mechanism as a possible cause of D-region electron density modification and noted the possibility of photon production and the potential for optical detection of the such events. The following year, the first elve observation (from the Space Shuttle, using a 60 field-s⁻¹ video-rate camera) was reported [*Boeck et al.*, 1992]. The elve appeared as a sudden, single-field brightening of the airglow layer along the limb of the Earth in immediate response to a lightning discharge. Although thousands of lightning discharges were examined during the same mission, the reported elve was the only one observed.

Despite intense efforts in the following years to document more and more examples of TLEs, the first ground-based observations of an elve were not made until the summer of 1995 [*Fukunishi et al.*, 1996]. The observations were made from the Yucca Ridge Field Site near Ft. Collins, Colorado with a vertically-oriented array—specially designed around the predictions of *Inan et al.* [1991]—of three high-speed (15 μ s time resolution) photometers triggered on sprite observations, and 18 elves were observed in a two-week period. In addition to documenting the short <1 ms lifetime of the elve, these observations served to confirm that elves and sprites were indeed two separate phenomena, and it was in *Fukunishi et al.* [1996] that the plural term “elves” (a belabored acronym of “emissions of light from VLF perturbations from EMP sources”) was coined.

The following summer (July 1996), Stanford University deployed a novel photometric array instrument called the Fly’s Eye at the Yucca Ridge Field Site and directly observed and confirmed the rapid lateral expansion involved in elves [*Inan et al.*, 1997]. The Fly’s Eye consisted of 9 high-speed (30 μ s time resolution) photometers arrayed horizontally, with a co-aligned video-rate camera for triggering on visual sprite observations. Typical expansion rates were around 3.1 times the speed of light, in direct agreement with the lightning EMP-heating mechanism. Subsequent deployment of the Fly’s Eye the following year (August 1997) at Langmuir Laboratory near Socorro, New Mexico demonstrated several more points of agreement with the lightning EMP-heating mechanism [*Barrington-Leigh and Inan*, 1999]:

- Elves are produced by both +CGs and –CGs (whereas sprites are normally produced only by +CGs)
- Elves have large lateral extents of 200–700 km across
- Elves are relatively abundant, with 39 observed in a single 7-hour period

During the winters of 1998–1999, 1999–2000, and 2000–2001, *Takahashi et al.* [2003] observed elves in winter thunderstorms over Japan using a vertically-oriented 16-anode photometer array. Like others before them, their instrument was manually triggered (likely on visual sightings of sprites in video-rate camera feeds) and reported elve features similar to those already seen, albeit in a very different meteorological context to that of the summer mesoscale convective systems in the United States Great Plains. They reported elve occurrence rates comparable to those of sprites, with a maximum of 26 elve observations from a single storm. More elve observations in similar winter thunderstorm conditions over the Mediterranean during the winter of 2005–2006 were published by *Ganot et al.* [2007]. These observations confirmed that elves are readily produced under a variety of meteorological conditions.

In October of 2003, the ISUAL (Imager for Sprites and Upper Atmospheric Lightning) instrument launched on board the Taiwanese FORMOSAT-2 satellite, beginning an era of global, long-term, and systematic TLE observations from space [*Chern et al.*,

2003]. The ISUAL payload consists of an image-intensified CCD camera (100 frame- s^{-1} in continuous mode, 650 frame- s^{-1} in burst mode), a six-channel spectrophotometer (10 kHz sampling rate at all times), and a 16-anode, vertically-oriented photometer array (2–20 kHz sampling rate at all times), all of which are triggered automatically (rather than manually as in prior ground-based instruments). The FORMOSAT-2 satellite maintains a ~ 900 km polar, sun-synchronized orbit with 14 orbital periods per day, and the ISUAL payload maintains a ~ 1000 km field of view along the limb of the Earth around the local midnight region. Immediately after its launch, ISUAL began observing a surprisingly large number of elves [Frey *et al.*, 2005]. After an initial three years of observations, it was clear that elves were the most commonly occurring TLE on the planet with a globally-average occurrence rate over eight times that of sprites, with a great abundance of elves observed over the oceans [Chen *et al.*, 2008].

Another notable result from the ongoing ISUAL experiment is the direct, optical confirmation of D-region ionization in elves (through measurement of 391.4 nm emissions associated with N_2^+ ions) [Mende *et al.*, 2005]. Further evidence of D-region electron density modification in association with elves has been reported using various VLF remote sensing techniques [Mika *et al.*, 2006; Cheng *et al.*, 2007].

1.4.2 Modeling

Inan *et al.* [1991] used a 1D model of a simple lightning EMP propagating into an magnetized, collisional plasma held in equilibrium to find that lightning EMPs can have a significant heating and ionization effect on the lower ionosphere. Rodriguez *et al.* [1992] continued the work by investigating the effect of the EMP strength and discharge orientation, and Taranenko *et al.* [1992] extended the model to include photon production. These efforts found that lightning EMP could drive a 100–500 factor increase in electron temperature, a near doubling of the electron density through ionization, and bright (although brief) optical emissions in the first two positive bands of

molecular nitrogen. *Taranenko et al.* [1993a,b] modeled both electron density modification and optical emissions in 1D again, this time using a “quasi-stationary” kinetic model (where the plasma distribution was allowed some freedom to stray from Maxwellian and the EMP propagation responded self-consistently to the changing plasma). They found that induced ionization should not be as strong as previously believed for normal-strength EMPs, and that at lower altitudes (<85 km) attachment should dominate over ionization to actually decrease the electron density, leading to a “sharpening” of the ionospheric boundary around 85 km.

Rowland et al. [1995, 1996], and *Fernsler and Rowland* [1996] used a 2D model in Cartesian space with ionization rates taken from laboratory swarm data and investigated the D-region plasma density modification associated with an elve. For normal-strength EMPs, their results were in good agreement with *Taranenko et al.* [1993a], and for very large EMPs they suggested that EMPs could drive breakdown at high altitudes, leading to ionization increases of several orders of magnitude and an effective “lowering” of the height of the ionosphere. *Inan et al.* [1996] used a 2D, quasi-stationary, cylindrically-symmetric model of optical emissions to characterize the spatiotemporal development of the visible elve. They showed that elves should look like rapidly expanding rings and that, when viewed at a long distance from the ground, the rapid expansion would actually appear to have a downward motion in the instrument field of view. *Veronis et al.* [1999] and *Barrington-Leigh et al.* [2001] expanded this work to additionally include lightning quasi-electrostatic fields and used it to interpret Fly’s Eye data, leading to the clarification that “sprite halos” were indeed phenomena distinct from sprites and often confused with elves. *Glukhov and Inan* [1996] used a Monte Carlo code to investigate the applicability of the quasi-stationary assumption used in earlier models and found the assumption valid.

Cho and Rycroft [1998] developed a 2D model in rectangular coordinates to look at elve and sprite initiation by horizontal ICs and extended it to 3D in [*Cho and Rycroft*, 2001]. Although three dimensions allow for inclusion of a realistic geomagnetic field (which produces slight asymmetry in the elve), their model did not consider the presence of the Earth’s magnetic field and mainly used the third dimension to explore

the orientation of the IC discharge. *Rodger et al.* [2001] used the model of *Cho and Rycroft* [1998] to investigate D-region density modification over the lifetime of an entire storm, taking lightning location data over the several-hour lifetime of a real storm and accumulating the associated changes in D-region electron density over time using return-stroke-to-density-change lookup table produced by the model. Their simulation did not carry the state of the perturbed ionosphere over multiple return strokes, though, and thus does not account for the fact that later return strokes launch EMPs into a disturbed ionosphere that changes their propagation behavior.

In 2003, *Nagano et al.* [2003] produced a full-wave 3D model that included a realistic geomagnetic field, noting an appreciable asymmetry in the optical structure of an elve caused by the field. *Kuo et al.* [2007] and *Marshall et al.* [2009] produced 3D finite-difference time-domain (FDTD) models that, unlike the full-wave model of *Nagano et al.* [2003], could self-consistently account for the effect of the dynamically changing D-region plasma on the EMP's upward propagation. The work of *Kuo et al.* [2007] was primarily focused on modeling of optical emissions and has been calibrated against actual ISUAL observations of elves from space; the work of *Marshall et al.* [2009] focuses on both optical emissions and electron density modification. In this work, we make frequent use of the model described by *Marshall et al.* [2009].

1.5 Contributions of This Work

Nearly all of the published observational work on elves to date has involved instruments that fall into one of the following categories:

1. free-running (non-triggered) but low-speed instruments that do not have enough temporal resolution to easily register individual elve events (e.g., video-rate cameras)
2. high-speed instruments that rely on triggering mechanisms (usually a manual triggering mechanism) that allow detailed observations of captured elves but necessarily involved high rates of missed detections (e.g., high-speed cameras, the Fly's Eye)

3. space-based instruments that are confined to orbital trajectories and cannot observe individual storms for more than a few minutes at a time due to orbital constraints (e.g., ISUAL)

Thus, observed elves are usually only a small sampling of the total elve activity within a storm, and there has been a lack of high-detection-rate observations of elve activity made over the course of the several hour lifetimes of storms. This work fills in that gap in observations. The focus of this work is not on case studies of individual events, but rather studies of aggregate elve activity on per-storm timescales as a whole.

A new high-detection-efficiency ground-based photometric imaging instrument called PIPER (discussed at great length in Chapter 3) was deployed by this author at the Yucca Ridge Field Station (summers of 2007 and 2009) and Langmuir Laboratory (summer of 2008). PIPER is a high-speed, multi-anode photometer array with 64 anodes arranged in both horizontal and vertical orientations. Moreover, the instrument is free-running (i.e., non-triggered), which eliminates the trigger bias that plagued earlier ground-based instruments. PIPER has observed large numbers of elves, similar to ISUAL, including 300 elves in one storm [Newsome and Inan, 2010].

The contributions of this work are

- conduction of multiple free-running (non-triggered), high-speed, ground-based elve observation campaigns, resulting in the first long-term, high-detection-efficiency, ground-based data set of elve observations
- development of an algebraic reconstruction technique for recovering the time- and space-dependent photon emission characteristic of elves from multi-axis photometric array observations
- compilation of statistics of elve geometric parameters, including radial extent, initial hole size, duration, and affected area
- determination of the mean and peak storm-time elve occurrence rates and characterization of their storm-to-storm and within-storm variability
- development of an empirical model to assess the dependence of elve production on lightning return stroke peak current and polarity

- recording of the first large-scale observations of rarely-reported “elve doublets” and evaluation of IC-radiated EMPs as a potential causative mechanism

1.6 Thesis Organization

This work is organized into 6 chapters:

1. A broad introduction to the near-Earth electromagnetic environment, lightning, and transient luminous events, as well as a review of past work on elves and the contributions of this work.
2. A detailed review of the theory of elves, including EMP production by lightning return strokes, EMP propagation into the collisional magnetized plasma of the lower ionosphere, elve photon production, ionospheric electron density modification through dissociative attachment and ionization, and ionospheric electron density relaxation through D-region chemistry.
3. A discussion of photometric imaging of elves, the PIPER instrument, and the recovery of an the photon emission profile of an from PIPER data.
4. A presentation of aggregate results and statistics from three years of free-running ground-based photometric imaging observations of elves, including analysis of storm-time occurrence rates and development of an empirical model relating elve production probability to commonly available lightning return stroke parameters.
5. A detailed investigation of elve doublets and their potential CID source mechanism.
6. A summary of this work and suggestions for future work.

Chapter 2

Elves

In this chapter, we give a detailed account of the physical mechanism that produces elves. We review in detail the form of the electromagnetic pulse (EMP) radiated by a return stroke, the behavior of the EMP as it propagates into the lower ionosphere, conversion of EMP energy into emitted photons and modified ionospheric electron density, and the chemistry of ionospheric relaxation following an elve event.

2.1 The Return Stroke Electromagnetic Pulse

A cloud-to-ground return stroke is a large electric current that varies rapidly in time and efficiently radiates an electromagnetic pulse (EMP). In this section, we discuss the return stroke current and the nature of the EMP that it launches.

The leader process that precedes a lightning return stroke forms several tortuous and highly conductive channels that extend from a charge reservoir in the thundercloud toward the ground. As a leader propagates downward, charge from the thundercloud is deposited along the leader channel. As one leader approaches the ground, a separate leader channel begins to extend up from the ground to meet it, and the two leader channels connect tens of meters above the ground in a poorly understood process called attachment [*Rakov and Uman, 2003*, pp. 137–143]. Once the two channels make contact, they form a single highly conductive path from the

thundercloud to the ground, and the charge that was earlier deposited in the channel begins to rapidly flow toward the ground. The large current rapidly heats the plasma inside the lightning channel, producing intense light (the lightning flash) and an acoustic shock wave (thunder). Charge in aborted channel branches flows back up their branches and down the main channel to ground. In a typical $-CG$, around 5 C of charge is lowered to the ground in a 100 μs timescale. Additional charge may be lowered in subsequent return strokes 10s or 100s of milliseconds later [*Rakov and Uman*, 2003, p. 146].

2.1.1 Return Stroke Current Models

The charge motion toward ground is most rapid near the point of attachment and is less rapid higher up in the channel. Thus, the EMP radiated by the return stroke current largely originates from near the ground, and contributions to the EMP from current higher up along the channel play a diminished role. One simple model of return stroke current is that of a single vertically-oriented current element of 500–1000 m height located at the ground carrying a current waveform $I_0(t)$. As this current flows at the base of the lightning channel, we refer to $I_0(t)$ as the channel base current. To calculate the form of the EMP radiated by a return stroke, we ultimately need to know the time rate of change of the current moment $\int I(z, t) dz$ of the lightning channel, and we seek to express the current moment explicitly in terms of the channel base current and a return stroke current model which describes how current in the rest of the channel is related to the current at the base. Popular choices for channel base current waveforms are shown in Figure 2.1 and are described below.

The double exponential channel base current (introduced by *Bruce and Golde* [1941]) is given by

$$I_0(t) = I_g [\exp(-at) - \exp(-bt)] u(t) \quad (2.1)$$

where $u(x) = 1$ if $x \geq 0$ and 0 otherwise. The double exponential waveform is simple and involves only three parameters (I_g , a , and b), but it is non-smooth at $t = 0$ and important values like peak current and peak rate of change of current are complicated

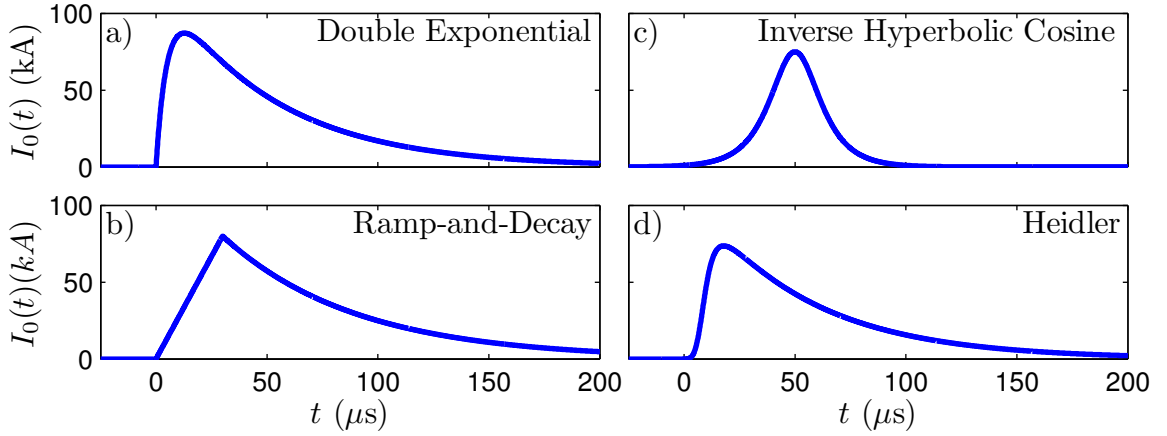


Figure 2.1: Example channel base current waveforms: (a) the double exponential waveform, (b) the ramp-and-decay waveform, (c) the inverse hyperbolic cosine waveform, and (d) the Heidler waveform. See the text for each waveform’s functional form and parameters. For each example, the waveform is plotted with those parameter values listed as “typical” in the text.

functions of the parameters. For example, the peak current I_p is given by

$$I_p = I_g \left(\frac{a}{b} \right)^{\frac{-a}{a-b}} - I_g \left(\frac{a}{b} \right)^{\frac{-b}{a-b}} \quad (2.2)$$

For a strong return stroke, typical values for the parameters might be $I_g = 125$ kA, $a = 0.02 \mu\text{s}^{-1}$, and $b = 0.2 \mu\text{s}^{-1}$. The ramp-and-decay channel base current (a version of which was used by, e.g., [Veronis et al. \[1999\]](#)) is given by

$$I_0(t) = \begin{cases} \frac{I_p}{\tau_r} t u(t) & \text{if } t \leq \tau_r \\ I_p \exp\left(\frac{t - \tau_r}{\tau_f}\right) & \text{otherwise} \end{cases} \quad (2.3)$$

where I_p is the peak current, τ_r is the ramp-up time, and τ_f is the decay time constant. The ramp-and-decay function parameters are more intuitive than the double exponential function parameters, but waveform itself is non-smooth both at the origin and at the peak. Typical values for the parameters might be $I_p = 80$ kA, $\tau_r = 30 \mu\text{s}$, and $\tau_f = 60 \mu\text{s}$. The 3D EMP-ionosphere interaction model of [Marshall et al. \[2009\]](#) used a simple inverse hyperbolic cosine return stroke channel base current given by

$$I_0(t) = \frac{I_p}{\cosh[\alpha(t - t_p)]} \quad (2.4)$$

where I_p is the peak current, t_p is the time of the peak in the current, and α controls the rise and fall time of the current. The inverse hyperbolic cosine waveform has intuitive parameters, is smooth everywhere, and is easy to integrate and differentiate, making it useful in calculating the associated radiation fields analytically. The shape of the waveform, however, is not very realistic, and this model is less useful in non-far-field situations. Typical values for the parameters might be $I_p = 75$ kA, $t_p = 50$ μ s, and $\alpha = 0.1$ μ s⁻¹. A common choice for modeling subsequent return strokes is the Heidler function [Heidler, 1985], given by

$$I_0(t) = \frac{I_g}{\eta} \frac{(t/\tau_1)^n}{(t/\tau_1)^n + 1} \exp(-t/\tau_2) u(t) \quad (2.5)$$

where I_g , τ_1 , τ_2 , and n are parameters and $\eta = \exp(-\tau_1/\tau_2) (n\tau_2/\tau_1)^{1/n}$ is a normalization constant. The Heidler function is smooth everywhere and exhibits realistic rounded edges at the origin and peak, and the peak current and peak rate of change of current are independently controlled by the parameters. However, as the Heidler function is not easily integrable and differentiable, its use in computing analytic descriptions of radiated fields is limited. Typical values for the parameters might be $I_0 = 200$ kA, $\tau_1 = 10$ μ s, $\tau_2 = 50$ μ s, and $n = 4$.

Popular models of lightning stroke currents include current contributions higher up along the lightning channel. Many of these are reviewed in [Rakov and Uman, 2003, ch. 12], and we highlight a few specific ones here. Each model assumes a single vertical channel extending from the cloud altitude H to the ground. For all models, the current flowing in the channel at altitude z' and at time t' is given by

$$I_c(z', t') = \begin{cases} u\left(t' - \frac{z'}{v_f}\right) P(z') I_0\left(t' - \frac{z'}{v}\right) & \text{for } 0 \leq z' \leq H \\ 0 & \text{otherwise} \end{cases} \quad (2.6)$$

where $u(x) = 1$ for $x \geq 0$ and 0 otherwise, $P(z')$ is the height-dependent current attenuation factor, v_f is the upward-propagating return stroke front speed, and v is

the current-wave propagation speed. The prime superscripts denote source locations as opposed to observation locations. As the current develops in the lightning channel, an image current effectively appears below the perfectly conducting plane of the Earth at $z'=0$ (an assumption that is valid since the typical value of the Earth conductivity σ_E is such that $\sigma_E \gg \omega\epsilon_0$ for frequencies ω that correspond to current risetimes) so that the total current $I(z', t')$ involved in launching an EMP is

$$I(z', t') = I_c(|z'|, t') \quad (2.7)$$

where z' can take both positive and negative values.

The transmission line (TL) model [*Uman and McLain, 1969*] assumes that the current which appears at the channel base propagates up the channel without attenuation at the same speed as the propagating return stroke front. The linear modified transmission line (MTLL) and exponential modified transmission line (MTLE) models are the same as the TL model, but with linear and exponentially tapering of the upward propagating current amplitude, respectively. The Bruce-Golde (BG) model [*Bruce and Golde, 1941*] assumes that the current that appears at the channel base potentially appears at the same time at all other heights along the channel but does not actually appear until the upward propagating return stroke front passes through and “uncovers” it. The traveling current source (TCS) model [*Heidler, 1985*] treats the current as being generated at, and propagating downward from, the upward-moving return stroke front location. The differences between these models are highlighted in Figure 2.2, which shows the channel current evolution over time for each model. Table 2.1, reproduced from Table 12.2 of *Rakov and Uman [2003]*, summarizes the different parameter choices for each model.

2.1.2 Radiated Fields: General Features

In this section, we derive the time-domain form of the electromagnetic pulse radiated by a return stroke current. Maxwell’s equations relate fields (the electric field \mathbf{E} and the magnetic field \mathbf{B}) to their sources (charge density ρ and current density \mathbf{J}). In free space, Maxwell’s equations take the form

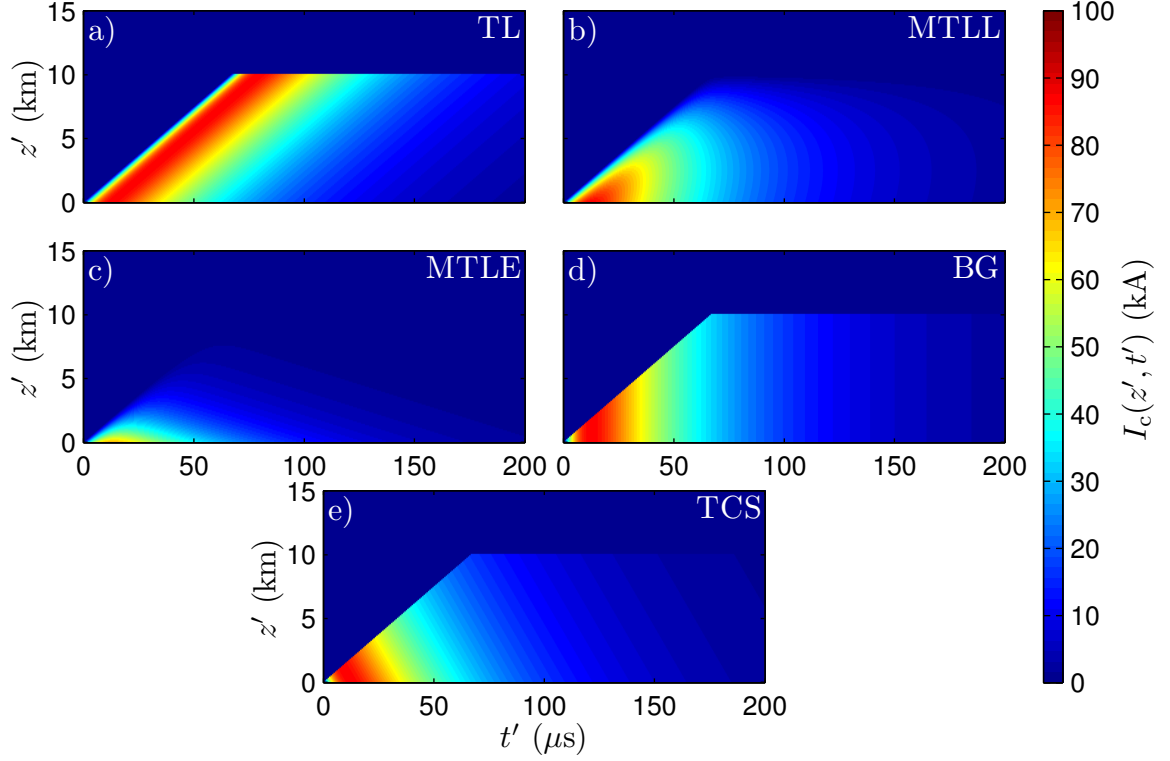


Figure 2.2: Plots of $I_c(z', t')$ for return stroke current models, using a double exponential channel base current waveform with $a = 0.02 \mu\text{s}^{-1}$ and $b = 0.2 \mu\text{s}^{-1}$. For all models, $H = 10 \text{ km}$ and $v_f = 0.5c$. For the MTLE model, $\lambda = 2 \text{ km}$.

Table 2.1: Return stroke current models (reproduced from [[Rakov and Uman, 2003](#), Table 12.2].)

Model	$P(z')$	v
TL	$u(z') - u(H - z')$	v_f
MTLL	$(1 - z'/H) [u(z') - u(H - z')]$	v_f
MTLE	$\exp(-z'/\lambda) [u(z') - u(H - z')]$	v_f
BG	$u(z') - u(H - z')$	∞
TCS	$u(z') - u(H - z')$	$-c$

$$\nabla \cdot \mathbf{E}(\mathbf{r}, t) = \frac{\rho(\mathbf{r}, t)}{\epsilon_0} \quad (2.8)$$

$$\nabla \cdot \mathbf{B}(\mathbf{r}, t) = 0 \quad (2.9)$$

$$\nabla \times \mathbf{E}(\mathbf{r}, t) = -\frac{\partial \mathbf{B}(\mathbf{r}, t)}{\partial t} \quad (2.10)$$

$$\nabla \times \mathbf{B}(\mathbf{r}, t) = \mu_0 \mathbf{J}(\mathbf{r}, t) + \epsilon_0 \frac{\partial \mathbf{E}(\mathbf{r}, t)}{\partial t} \quad (2.11)$$

where ϵ_0 and μ_0 are the free-space electric permittivity and free-space magnetic permeability, respectively. While one can obtain fields from sources using Maxwell's equations directly, it is easier to use the auxiliary electromagnetic potentials (the electric scalar potential Φ and the magnetic vector potential \mathbf{A}). The fields are obtained from the potentials through differentiation

$$\mathbf{E}(\mathbf{r}, t) = -\nabla \Phi(\mathbf{r}, t) - \frac{\partial \mathbf{A}(\mathbf{r}, t)}{\partial t} \quad (2.12)$$

$$\mathbf{B}(\mathbf{r}, t) = \nabla \times \mathbf{A}(\mathbf{r}, t) \quad (2.13)$$

and the potentials are related to each other through the Lorentz gauge

$$\frac{\partial \Phi(\mathbf{r}, t)}{\partial t} = -c^2 \nabla \cdot \mathbf{A}(\mathbf{r}, t) \quad (2.14)$$

We can express $\Phi(\mathbf{r}, t)$ explicitly in terms of $\mathbf{A}(\mathbf{r}, t)$ by integrating (2.14) over time:

$$\Phi(\mathbf{r}, t) = -c^2 \nabla \cdot \int_0^t \mathbf{A}(\mathbf{r}, \tau) d\tau \quad (2.15)$$

If the return stroke is taken to start at $t=0$, then we have assumed that no currents appear in the channel before $t=0$ and that $\mathbf{A}(\mathbf{r}, t)$ is thereby 0 for all $t < 0$. This assumption is not strictly true (the charge already in the channel at $t=0$ moves into the channel before $t=0$ during the downward propagation of the leader), but the currents associated with leader propagation do not play a significant role in producing

elves and we choose to ignore them in calculating the return stroke radiated fields. Thus, the electric and magnetic fields of (2.12) and (2.13) can be obtained directly from $\mathbf{A}(\mathbf{r}, t)$ as

$$\mathbf{E}(\mathbf{r}, t) = c^2 \nabla \nabla \cdot \int_0^t \mathbf{A}(\mathbf{r}, \tau) d\tau - \frac{\partial \mathbf{A}(\mathbf{r}, t)}{\partial t} \quad (2.16)$$

$$\mathbf{B}(\mathbf{r}, t) = \nabla \times \mathbf{A}(\mathbf{r}, t) \quad (2.17)$$

The magnetic vector potential is obtained as a volume integration over the source current density $\mathbf{J}(\mathbf{r}', t')$:

$$\mathbf{A}(\mathbf{r}, t) = \frac{\mu_0}{4\pi} \int_{V'} \frac{\mathbf{J}(\mathbf{r}', t - |\mathbf{r} - \mathbf{r}'|/c)}{|\mathbf{r} - \mathbf{r}'|} dV' \quad (2.18)$$

For our lightning return stroke current models, the source volume V' is a line segment at $x' = y' = 0$ extending from $z' = -H$ to $z' = H$. The top half is the return stroke current channel, and the bottom half (below ground) is the image of the return stroke current channel in the perfectly conducting plane of the Earth at $z' = 0$. The current in the channel $I(z', t')$ is always z' -directed and thus $\mathbf{J}(\mathbf{r}', t') = I(z', t') \hat{\mathbf{z}}$. Because there are no x' - or y' -directed currents, the magnetic vector potential $\mathbf{A}(\mathbf{r}, t)$ has only a z -component:

$$A_z(\mathbf{r}, t) = \frac{\mu_0}{4\pi} \int_{-H}^H \frac{I(z', t - |\mathbf{r} - z'\hat{\mathbf{z}}|/c)}{|\mathbf{r} - z'\hat{\mathbf{z}}|} dz' \quad (2.19)$$

We are interested in the radiated fields at large distances from the return stroke and make use of the far-field approximation to simplify (2.19) further. The far-field approximation involves three assumptions:

1. $|\mathbf{r} - z'\hat{\mathbf{z}}| \simeq r$ when determining magnitudes [i.e., the denominator of (2.19)].
2. $|\mathbf{r} - z'\hat{\mathbf{z}}| \simeq r - z' \cos \theta$ when determining time delays [i.e., the second argument to $I(\cdot)$ in the numerator of (2.19)].

3. All terms with $1/r$ dependence stronger than $1/r$ (i.e., $1/r^2$, $1/r^3$, etc.) are negligible and can be assumed to be 0.

Employing the far-field approximation and adopting the spherical coordinate system, (2.19) further reduces to

$$A_z(r, \theta, t) = \frac{\mu_0}{4\pi r} \int_{-H}^H I\left(z', t - \frac{r}{c} + \frac{\cos \theta}{c} z'\right) dz' \quad (2.20)$$

In spherical coordinates, the components of $\mathbf{A}(r, \theta, t)$ are $A_r(r, \theta, t) = A_z(r, \theta, t) \cos \theta$, $A_\theta(r, \theta, t) = -A_z(r, \theta, t) \sin \theta$, and $A_\phi(r, \theta, t) = 0$. The symmetry of our problem and the form of (2.20), along with the far-field approximation, greatly simplify evaluation of (2.16) and (2.17). Noting that $\partial/\partial\phi \rightarrow 0$, $A_z/r \rightarrow 0$, $\partial A_z/\partial r \rightarrow (-1/c) \partial A_z/\partial t$, $(1/r) \partial(r A_z)/\partial r \rightarrow (-1/c) (\partial A_z/\partial t)$, and $(1/r^2) \partial(r^2 A_z)/\partial r \rightarrow (-1/c) (\partial A_z/\partial t)$, (2.20) in (2.16) and (2.17) yields a simple description of the radiated EMP in the far-field:

$$\mathbf{E}(r, \theta, t) = \sin \theta \frac{\partial A_z(r, \theta, t)}{\partial t} \hat{\theta} \quad (2.21)$$

$$\mathbf{B}(r, \theta, t) = \frac{\sin \theta}{c} \frac{\partial A_z(r, \theta, t)}{\partial t} \hat{\phi} \quad (2.22)$$

A few general features of the radiated EMP emerge. Regardless of which specific return stroke channel current model is assumed, the radiated EMP fields have a $(\sin \theta)/r$ dependence (the $1/r$ dependence being carried by A_z), giving rise to the classic “doughnut”-shaped radiation pattern of a lightning return stroke: fields are largest in directions perpendicular to the return stroke channel (i.e., along the ground and at low elevation angles) and smallest in direction parallel with the return stroke channel (i.e., at very high elevation angles). Additional return stroke model-dependent features of the radiated EMP fields are carried in the $\partial A_z/\partial t$ factor and are considered next.

2.1.3 Radiated Fields: Model-Dependent Features

To find $\partial A_z / \partial t$, which appears in (2.21) and (2.22), in terms of the return stroke model parameters $I_0(t')$, $P(z')$, v_f , and v , we must first evaluate the integral of (2.20). By assuming $P(z')$ in (2.6) is 0 for $z > H$, we can replace H with ∞ in the limits of the integration and, recognizing that the integral can be broken into two parts (the lightning channel and its image), we can proceed as follows:

$$\begin{aligned} A_z(r, \theta, t) &= \frac{\mu_0}{4\pi r} \int_{-\infty}^{\infty} I_c \left(|z'|, t - \frac{r}{c} + \frac{\cos \theta}{c} z' \right) dz' \\ &= \frac{\mu_0}{4\pi r} \int_0^{\infty} I_c \left(z', t - \frac{r}{c} + \frac{\cos \theta}{c} z' \right) dz' \\ &\quad + \frac{\mu_0}{4\pi r} \int_0^{\infty} I_c \left(z', t - \frac{r}{c} - \frac{\cos \theta}{c} z' \right) dz' \end{aligned}$$

Then, substituting (2.6) for $I_c(z', t')$ and changing the variables of integration to $\tau = t - r/c + (z' \cos \theta)/c - z'/v$ and $\tau_1 = t - r/c - (z' \cos \theta)/c - z'/v$, we arrive at

$$\begin{aligned} A_z(r, \theta, t) &= \frac{\mu_0 \tilde{v}}{4\pi r} \int_{-\infty}^{t-r/c} u \left[\tau - \beta \left(t - \frac{r}{c} \right) \right] \tilde{P} \left(t - \frac{r}{c} - \tau \right) I_0(\tau) d\tau \\ &\quad + \frac{\mu_0 \tilde{v}_1}{4\pi r} \int_{-\infty}^{t-r/c} u \left[\tau_1 - \beta_1 \left(t - \frac{r}{c} \right) \right] \tilde{P}_1 \left(t - \frac{r}{c} - \tau_1 \right) I_0(\tau_1) d\tau_1 \end{aligned} \quad (2.23)$$

where

$$\tilde{v} = \frac{vc}{c - v \cos \theta} \quad \tilde{v}_1 = \frac{vc}{c + v \cos \theta} \quad (2.24)$$

$$\beta = \frac{(v - v_f) \tilde{v}}{v_f v + (v - v_f) \tilde{v}} \quad \beta_1 = \frac{(v - v_f) \tilde{v}_1}{v_f v + (v - v_f) \tilde{v}_1} \quad (2.25)$$

$$\tilde{P}(t') = P(\tilde{v}t') \quad \tilde{P}_1(t') = P(\tilde{v}_1 t') \quad (2.26)$$

The new variables \tilde{v} and \tilde{v}_1 denote the effective current wave propagation speeds for

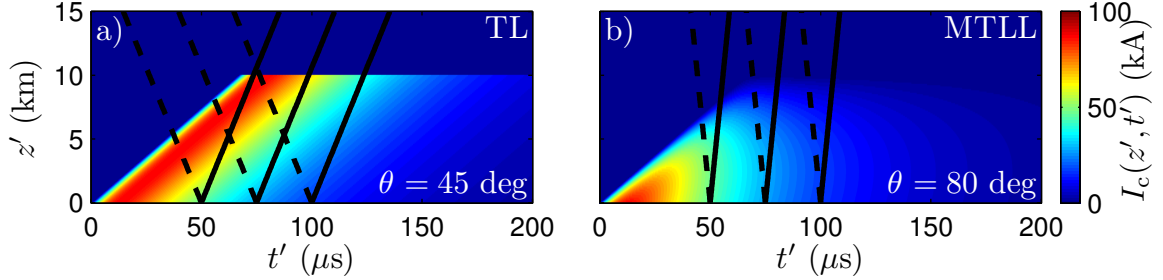


Figure 2.3: Graphical interpretation of the contour integration over $I_c(z', t')$ of (2.23). The integration contour at each instant of time traces out a V: the dashed branch is over the image channel and the solid branch is over the main channel. As time evolves, the V sweeps from left to right. For larger values of θ , the branches come closer together until they become vertical and overlapping for $\theta = 90^\circ$.

the main and image channels, respectively, and carry the θ -dependence produced by the model. The variables β and β_I represent the mismatch in v and v_f for the main and image channels, respectively. The functions \tilde{P} and \tilde{P}_I are the channel attenuation factors expressed in the time domain using the main and image current wave propagation speeds. Note that $0 \leq v_f \leq c$, $v \leq v_f$, and $0 \leq \theta \leq \pi/2$, which in turn imply that $\tilde{v} \geq \tilde{v}_I$.

We can interpret the integration over channel current of (2.23) graphically as in Figure 2.3. At each instant in time t , the integration range makes a “V” shape over $I_c(z', t')$ anchored at $t' = t - r/c$. The left branch of the V (the dashed lines in Figure 2.3) is the contribution to $A_z(r, \theta, t)$ from the return stroke channel’s image, and the right branch of the V (the solid lines in Figure 2.3) is the contribution from the return stroke channel itself. For observation points located at high elevation angles (small θ), the angle between the branches of the V is larger, and for observation points located at low elevation angles (θ near 90°), the branches of the V come together, becoming vertical and overlapping for ground-based observation ($\theta = 90^\circ$). As time evolves, the V moves over $I_c(z', t')$ from left to right and the integration over the V path sweeps out the time evolution of $A_z(r, \theta, t)$. It is the time rate of change of this quantity that forms the shape of the EMP as it passes through the observation point (r, θ) .

The form of (2.23) can be expressed more simply if we assume that $v = v_f$, as in the transmission line models. In this case, we note that $\tilde{v} \geq \tilde{v}_I \geq 0$ and $\beta = \beta_I = 0$. We

can then write (2.23) as

$$A_z(r, \theta, t) = \frac{\mu_0 \tilde{v}}{4\pi r} \left(I_0 * \tilde{P} \right) \left(t - \frac{r}{c} \right) + \frac{\mu_0 \tilde{v}_1}{4\pi r} \left(I_0 * \tilde{P}_1 \right) \left(t - \frac{r}{c} \right) \quad (2.27)$$

and

$$\frac{\partial A_z(r, \theta, t)}{\partial t} = \frac{\mu_0 \tilde{v}}{4\pi r} \left(I_0 * \frac{\partial \tilde{P}}{\partial t} \right) \left(t - \frac{r}{c} \right) + \frac{\mu_0 \tilde{v}_1}{4\pi r} \left(I_0 * \frac{\partial \tilde{P}_1}{\partial t} \right) \left(t - \frac{r}{c} \right) \quad (2.28)$$

where $*$ represents the convolution operation.

In the case that $P(z') = u(z')$ (which assumes $H = \infty$), (2.28) simplifies further. $\partial \tilde{P}(t)/\partial t$ and $\partial \tilde{P}_1(t)/\partial t$ reduce to the Dirac delta function $\delta(t)$, and (2.28) reduces to

$$\frac{\partial A_z(r, \theta, t)}{\partial t} = \frac{\mu_0}{4\pi r} (\tilde{v} + \tilde{v}_1) I_0 \left(t - \frac{r}{c} \right) \quad (2.29)$$

$$= \frac{\mu_0}{2\pi r} \frac{c^2 v_f}{c^2 - v_f^2 \cos^2 \theta} I_0 \left(t - \frac{r}{c} \right) \quad (2.30)$$

which, when substituted into (2.21), leads directly to the familiar expression for the radiated electric field from a TL model return stroke with $H = \infty$ given by [Kridner \[1992\]](#)

$$\mathbf{E}(r, \theta, t) = \frac{\mu_0}{2\pi r} \frac{v_f \sin \theta}{1 - (v_f/c)^2 \cos^2 \theta} I_0 \left(t - \frac{r}{c} \right) \hat{\theta} \quad (2.31)$$

While (2.28) is only an approximation, we can at least develop some intuition about the form of an EMP radiated by a return stroke by examining it. We see that the EMP that passes through the point (r, θ) is the superposition of two waveforms (radiated by the main and image channels, respectively), both of which are convolutions of the channel base current with “compressed” versions of the channel attenuation factor. For an infinitesimally short channel, $\tilde{P}(t) = \tilde{P}_1(t) = \delta(t)$ and the EMP waveform takes the form of $\partial I_0(t)/\partial t$. For infinitely extended channels, $\tilde{P}(t) = \tilde{P}_1(t) = u(t)$ and the EMP waveform takes the form of $I_0(t)$. For channels in

between (i.e., most realistic channels), the EMP waveform is the superposition of two waveforms shaped somewhere between $\partial I_0(t)/\partial t$ and $I_0(t)$. As most channel base currents involve very fast current rise-times (the peak value of $\partial I_0(t)/\partial t$ is high), the peak electric field radiated by shorter effective return stroke channels are typically larger than those radiated by longer effective return stroke channels.

The relative strengths of the two component waveforms are determined by \tilde{v} and \tilde{v}_I , which are in turn determined by the current wave propagation speed v and the zenith angle θ . For low current wave propagation speeds, the difference between the two waveform strengths is negligible. For large current wave propagation speeds, the waveform radiated by the main channel dominates that radiated by the image channel at small zenith angles (large elevation angles). At near vertical angles, this difference is negligible as the global $\sin \theta$ dependence means very little energy is radiated in these directions anyway. On the ground, $\tilde{v} = \tilde{v}_I$ and the two waveforms are identical. Thus, ground-based radio receivers receiving ground wave sferics see simpler waveforms than a hypothetical sky-based radio receiver receiving the same sferic. In the sky, EMPs have slightly broader peaks with reduced strength relative to those received on the ground.

Figure 2.4 illustrates many of these features by plotting the electric field radiated by both the TL and MTLE models given the same channel base current $I_0(t)$. For both models, the return stroke front speed is $v_f = c/2$. The fields are plotted at a range $r = 100$ km on the ground ($\theta = 90^\circ$) and in the sky ($\theta = 45^\circ$). For the TL model, the channel is allowed to have infinite extent ($H = \infty$) and the radiated electric field waveform is similar to the $I_0(t)$. For the MTLE model, the channel has a much more limited extent ($\lambda = 2$ km), and the radiated electric field waveform is more similar to $\partial I_0(t)/\partial t$. Note that, due to the sharp initial rise in $I_0(t)$, the fields radiated by the MTLE model (with the effectively shorter channel) have higher peak values than those radiated by the TL model (with the longer channel).

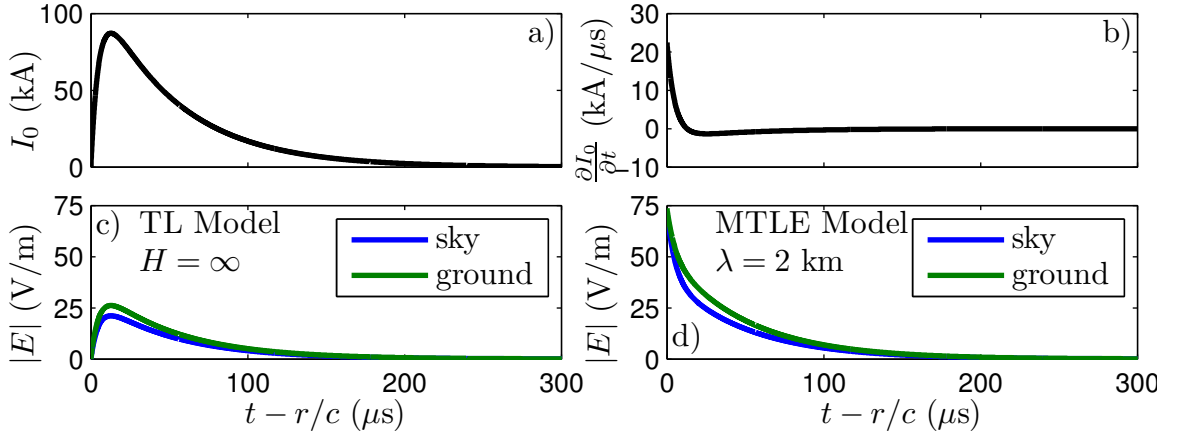


Figure 2.4: Radiated E fields at $r=100$ km on the ground ($\theta=90^\circ$) and in the sky ($\theta=45^\circ$). (a) Double exponential channel base current. (b) Time rate of change of channel base current. (c) E field waveform radiated by the TL return stroke model. (d) E field waveform radiated by the MTLE model ($\lambda=2$ km). In both models, $v_f=c/2$.

2.2 EMP Propagation in the Lower Ionosphere

In the previous section, we developed time-domain expressions for the electromagnetic fields radiated by a lightning return stroke. These fields (the EMP) propagate radially outward from the return stroke in the lower atmosphere, which is assumed to be very similar to free space. As the EMP enters the lower ionosphere, the medium through which it propagates transitions from free space into a highly collisional, magnetized plasma. Propagation in the lower ionosphere becomes significantly more complex, with wave absorption and reflection phenomena added to the propagation phenomena featured in the lower atmosphere. In this section, we describe EMP propagation in the lower ionosphere. Our main interest is to determine how the electron density profile of the lower ionosphere effects the altitude range at which the EMP wave energy is reflected and/or absorbed. Due to the complexity of this topic, we pursue a frequency-domain description of EMP propagation into the lower ionosphere and augment the discussion with examples from simulation.

The change in propagation behavior as an EMP moves into the lower ionosphere is accounted for in Maxwell's equations (2.8)–(2.11) by the transition of the free-space

permittivity ϵ_0 (a scalar) into the plasma permittivity $\bar{\epsilon}$ (a tensor). To obtain $\bar{\epsilon}$, we assume a cold, collisional, magnetized electron plasma (neglecting the effect of ions as EMP frequencies are generally too high to significantly interact with ions due to their heavy mass) and start with the force balance equation on one of its electrons:

$$m_e \frac{\partial \mathbf{v}(t)}{\partial t} = q_e \mathbf{E}(t) + q_e \mathbf{v}(t) \times [\mathbf{B}_0 + \mathbf{B}(t)] - \nu_c m_e \mathbf{v}(t) \quad (2.32)$$

where m_e and q_e are the electron mass and charge, respectively, $\mathbf{v}(t)$ is the electron's velocity, $\mathbf{E}(t)$ and $\mathbf{B}(t)$ are the externally applied electric and magnetic fields (e.g., the wave fields of an incoming EMP), \mathbf{B}_0 is the Earth's magnetic field, and ν_c is the effective rate of electron-neutral collisions. Noting that $\mathbf{B}(t) \ll \mathbf{B}_0$ even for the strongest of lightning EMPs and multiplying by $q_e N_e / m_e$, we can rewrite (2.32) as

$$\frac{\partial \mathbf{J}(t)}{\partial t} = \epsilon_0 \omega_p^2 \mathbf{E}(t) - \omega_c \mathbf{J}(t) \times \hat{\mathbf{B}}_0 - \nu_c \mathbf{J}(t) \quad (2.33)$$

where N_e is the electron number density, $\mathbf{J}(t)$ is the current density associated the the electrons' motions, ω_p is the electron plasma frequency, ω_c is the electron cyclotron frequency, $\hat{\mathbf{B}}_0$ is the unit direction vector of the Earth's magnetic field, and

$$\mathbf{J}(t) = q_e N_e \mathbf{v}(t) \quad (2.34)$$

$$\omega_p^2 = \frac{q_e^2 N_e}{m_e \epsilon_0} \quad (2.35)$$

$$\omega_c = \frac{|q_e|}{m_e} |\mathbf{B}_0| \quad (2.36)$$

Equation (2.33) relates the applied electric field $\mathbf{E}(t)$ to the induced current density $\mathbf{J}(t)$ in the plasma and can be interpreted as a form of Ohm's Law. In the remainder of this discussion, we assume time-harmonic wave propagation (all time-varying quantities have $\exp(j\omega t - j\mathbf{k}\mathbf{n} \cdot \mathbf{r})$ time- and space-dependencies) and replace time-domain quantities (e.g., $\mathbf{E}(t)$) in formulas with their complex phasors (e.g., \mathbf{E}). If we choose our coordinate system so that \mathbf{B}_0 is directed along the z-direction, (2.33) simplifies to $\mathbf{J} = \bar{\sigma} \mathbf{E}$, where $\bar{\sigma}$ is the complex plasma conductivity tensor given by

$$\bar{\sigma} = \begin{bmatrix} \frac{\epsilon_0 \omega_p^2 (j\omega + \nu_c)}{(j\omega + \nu_c)^2 + \omega_c^2} & \frac{-\epsilon_0 \omega_p^2 \omega_c}{(j\omega + \nu_c)^2 + \omega_c^2} & 0 \\ \frac{\epsilon_0 \omega_p^2 \omega_c}{(j\omega + \nu_c)^2 + \omega_c^2} & \frac{\epsilon_0 \omega_p^2 (j\omega + \nu_c)}{(j\omega + \nu_c)^2 + \omega_c^2} & 0 \\ 0 & 0 & \frac{\epsilon_0 \omega_p^2}{j\omega + \nu_c} \end{bmatrix} \quad (2.37)$$

The complex plasma permittivity tensor $\bar{\epsilon}$ can be written in terms $\bar{\sigma}$ as $\bar{\epsilon} = \epsilon_0 + \bar{\sigma}/j\omega$. Substituting the more convenient quantities \tilde{X} and \tilde{Y} , we find that $\bar{\epsilon} = \epsilon_0 \bar{\epsilon}_r$ with

$$\bar{\epsilon}_r = \begin{bmatrix} 1 + \frac{\tilde{X}}{\tilde{Y}^2 - 1} & 1 + \frac{j\tilde{X}\tilde{Y}}{\tilde{Y}^2 - 1} & 0 \\ 1 - \frac{j\tilde{X}\tilde{Y}}{\tilde{Y}^2 - 1} & 1 + \frac{\tilde{X}}{\tilde{Y}^2 - 1} & 0 \\ 0 & 0 & 1 - \tilde{X} \end{bmatrix} \quad (2.38)$$

where

$$\tilde{X} = \frac{\omega_p^2}{\omega^2} \frac{1}{1 - j\nu_c/\omega} \quad (2.39)$$

$$\tilde{Y} = \frac{\omega_c}{\omega} \frac{1}{1 - j\nu_c/\omega} \quad (2.40)$$

are the normalized plasma and cyclotron frequencies, respectively, with collision effects (the $1 - j\nu_c/\omega$ factor) included.

The relative permittivity $\bar{\epsilon}_r$ characterizes the response of the plasma to an applied electric field (in our case, the electric field of a propagating wave). To study $\bar{\epsilon}_r$, we consider time-harmonic electromagnetic waves of frequency $\omega > \omega_p$ externally incident upon a plasma with relative permittivity $\bar{\epsilon}_r$. In the event of no magnetic field ($\omega_c = 0$ and $\tilde{Y} = 0$) and no collisions ($\nu_c = 0$ and \tilde{Y} is strictly real), $\bar{\epsilon}_r$ reduces to a purely real scalar $\epsilon_r = 1 - \omega_p^2/\omega^2$. A portion of the energy in the applied time-harmonic wave electric field drives a time-harmonic conduction current in the plasma that is in phase quadrature with the field so that $\langle \mathbf{E} \cdot \mathbf{J} \rangle = 0$ (where $\langle \cdot \rangle$ represents the time-average of a quantity) and there is no Ohmic loss of wave energy (only a back-and-forth

exchange between the potential energy in the field and the kinetic energy in the current produced by field acceleration of charge carriers and re-radiation of fields by accelerated charge carriers). However, the index of refraction of the propagating wave $n = \sqrt{\epsilon_r}$ decreases, allowing for possible reflection of wave energy from the plasma if the incident wave is incident from a medium with a different permittivity (say, the neutral atmosphere or a less dense region of plasma below).

For denser collisionless plasmas (ω_p and \tilde{X} larger), the driven conduction current is larger (more electrons are available to compose the current) and the index of refraction n remains purely real but continues to decrease. If the plasma density increases large enough to make $\omega_p > \omega$, all of the incident wave energy drives the plasma conduction current, n becomes purely imaginary, and the incident wave becomes evanescent in the forward direction, resulting in total reflection of the incoming wave.

If we allow the presence of a magnetic field, we have $\omega_c > 0$ and $\tilde{Y} > 0$ and anisotropy is introduced. The permittivity $\bar{\epsilon}$ becomes a tensor but remains purely real due to lack of collisions ($\nu_c = 0$ and \tilde{X} and \tilde{Y} are purely real). The driven conduction current no longer necessarily aligns with the driving wave electric field, and the re-radiated electric field may add to the driving electric field differently than in the isotropic (no magnetic field) case. One famous result of anisotropy in a plasma is the existence of an electromagnetic wave mode that propagates through the anisotropic plasma despite the fact that its frequency is lower than the plasma frequency (the so-called “whistler” mode).

The effect of collisions ($\nu_c > 0$) is to cause \tilde{X} and \tilde{Y} to have imaginary components, which manifest themselves as an exponential decay in the propagating wave electric field amplitude. Physically, collisions interrupt the ordered motion of plasma electrons in response to a wave electric field, causing a reduction in the conduction current amplitude and an alignment of its phase with the driving electric field. The non-quadrature phase relationship between the driving field and the conduction current means $\langle \mathbf{E} \cdot \mathbf{J} \rangle \neq 0$ and the wave suffers Ohmic-type losses of energy as collisions transfer energy from the incoming wave to the ambient neutral population among which the plasma exists. The wave continues to propagate into the plasma, but with an increasingly smaller and smaller wave amplitude.

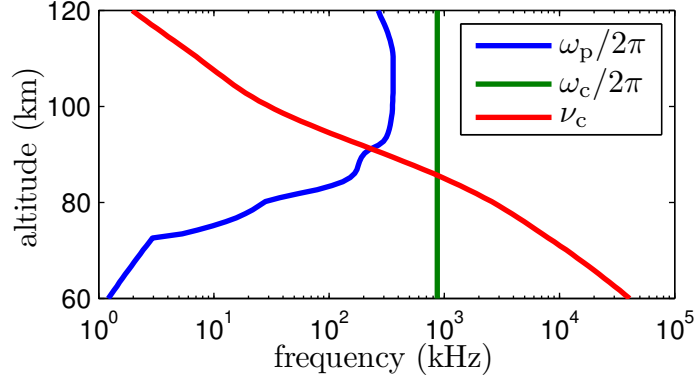


Figure 2.5: Profiles of the three characteristic frequencies over the lower nighttime ionosphere: the plasma frequency (ω_p), the cyclotron frequency (ω_c), and the electron-ion collision frequency (ν_c).

Unlike the conceptual homogenous plasmas considered in the discussion above, the lower ionosphere is an inhomogeneous plasma with a plasma frequency that increases exponentially with altitude and an electron-neutral collision frequency that decreases exponentially with altitude. Figure 2.5 shows how ω_p , ω_c , and ν_c vary throughout the lower nighttime ionosphere.

Figure 2.6 illustrates the inhomogeneity of the lower nighttime ionosphere in the ELF to LF frequency range (in which lightning strongly radiates). At each altitude and frequency, \tilde{X} and \tilde{Y} are computed and used to solve Maxwell's curl equations (specifically, $\mathbf{n} \times \mathbf{n} \times \mathbf{E} = -\tilde{\epsilon}_r \mathbf{E}$ where $\mathbf{n} = c\omega^{-1}\mathbf{k}$) for non-trivial solutions of the refractive index $n = \mu - j\chi$ under the assumption that $\mathbf{n} \parallel \hat{\mathbf{B}}_0$ (parallel propagation) and again under the assumption that $\mathbf{n} \perp \hat{\mathbf{B}}_0$ (perpendicular propagation). For propagation in each direction (or any direction), there are two solutions which characterize the propagation of different wave modes in that direction. In the case of parallel propagation at these frequencies, these solutions are the left-handed (LH) mode and the right-handed “whistler” mode. In the case of perpendicular propagation, these solutions are the ordinary (O) mode and the extraordinary (E) mode. Locations and frequencies in which χ is large represent regions of the ionosphere in which a wave mode is strongly absorbed by the plasma, and locations and frequencies in which the

refractive index $n = \mu - j\chi$ changes rapidly with altitude represent regions of potentially strong wave reflection. Clearly, the evolution of an EMP as it propagates into the lower ionosphere is strongly dependent on its component frequency content and its direction of propagation.

Figure 2.6 only describes the nature of the time-harmonic wave modes supported by the ionospheric plasma at each altitude. Numerical approaches (e.g., full-wave or finite-difference time-domain methods) are needed to understand how an EMP incident on the plasma from below is absorbed and reflected. Figure 2.7 shows results of a simulated EMP propagating into the lower ionosphere from below, produced by the finite-difference time-domain (FDTD) model used by [Marshall et al. \[2009\]](#). The Earth's magnetic field lies at a 45° angle, i.e., $\hat{\mathbf{B}}_0 = -(\hat{\mathbf{x}} + \hat{\mathbf{z}})/\sqrt{2}$. The time step size is 112 ns and the electric field magnitude is written out every 5.6 μs (which gives rise to the striations in Figures 2.7c and 2.7d). The background neutral density profile, normalized by the neutral density at the Earth's surface N_0 , is shown in Figure 2.7a. The simulation is repeated for several different electron density profiles, shown in Figure 2.7b. These profiles are taken from the IRI-2001 ionosphere model and essentially represent the range of electron densities that might be seen over the course of a summer night in the United States Great Plains.

Figures 2.7c and 2.7d show the maximum electric field magnitude and reduced electric field magnitude, respectively, seen at each point (x, z) over the duration of the simulation of profile 5. (The reduced electric field magnitude is merely the electric field magnitude normalized by the background neutral density and is a quantity that plays an important role in determining rates of various types of inelastic collisions. It is measured in units of Townsends: $1 \text{ Td} = 10^{13} \text{ V-m}^2$.) Clearly, most of the EMP energy reflects from $\sim 90 \text{ km}$ altitude, although some energy propagates on through to higher altitudes in the whistler wave mode.

Figures 2.7e and 2.7f show the maximum electric field and reduced electric field magnitudes, respectively, as would be observed at each altitude z over the duration of the simulation for each profile and illustrate the role the electron density profile plays in EMP propagation. For denser electron density profiles (e.g., profiles 1 and 2), the EMP reflects at lower altitudes; for less dense electron density profiles (e.g.,

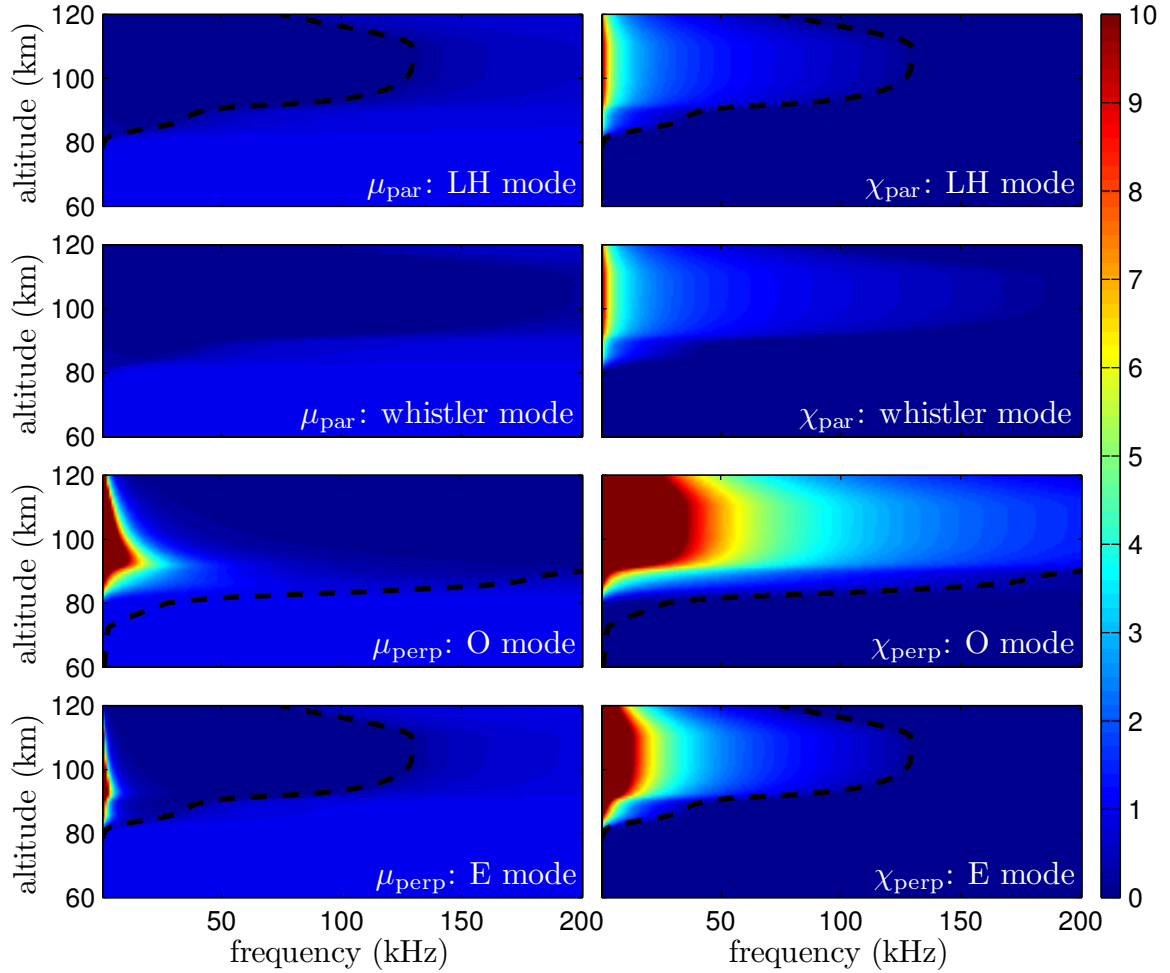


Figure 2.6: Profiles of the refraction indices over the ELF to LF frequency range in the lower nighttime ionosphere. Values of μ and χ (where $n = \mu - j\chi$) are shown for the LH and whistler modes (parallel propagation) and the O and E modes (perpendicular propagation). Additionally, various mode cutoff frequency profiles (strictly applicable only for the case of no collisions) are plotted as dashed lines.

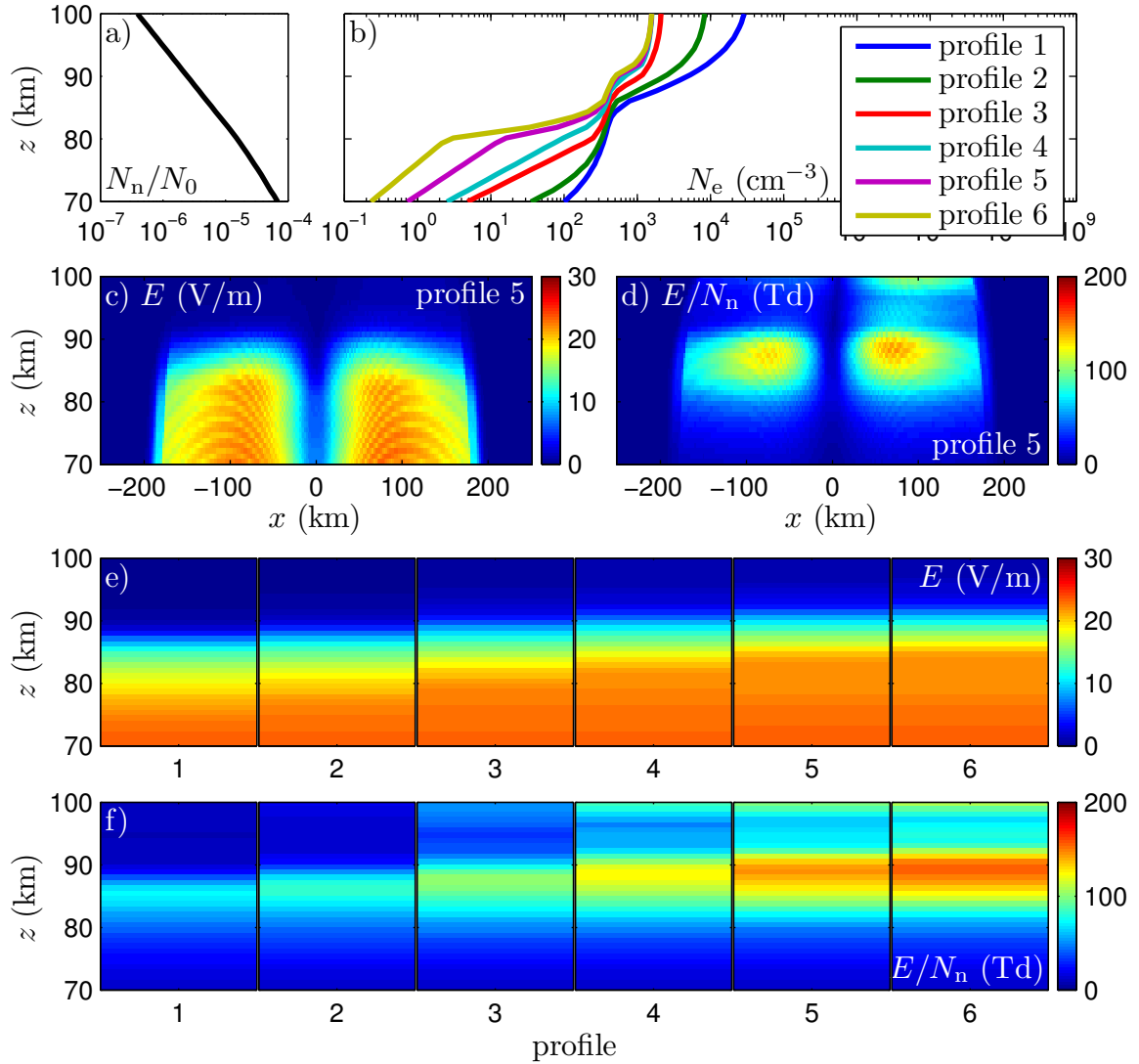


Figure 2.7: EMP propagation into the lower nighttime ionosphere. (a) Neutral density profile, normalized by the neutral density at the Earth's surface, N_0 . (b) Electron density profiles used in the simulations. (c) Peak electric field magnitude and (d) peak reduced electric field magnitude seen at each location (x, z) as a lightning EMP enters and reflects from the D-region ionosphere of profile 5. (e) Peak electric field magnitude and (f) peak reduced electric field magnitude seen at each altitude z for each ionospheric electron density profile.

profiles 5 and 6), the EMP reflects at higher altitudes. Because the reduced electric field magnitude is inversely proportional to the background neutral density (which falls exponentially with increasing altitude), less dense electron density profiles allow the EMP to attain higher values of reduced electric field magnitude before reflection. As we see in the next section, high reduced electric field magnitudes drive increased photon production and electron density modification.

Figure 2.7 also provides insight into the effect that ionospheric irregularities can have on elve production. Irregularities are changes or perturbations in ionospheric electron density that appear over limited time and spatial scales. Irregularities that are small in spatial extent relative to elve sizes have little effect on elve production. Spatially large irregularities, however, can increase or decrease the chance for elve production. Irregularities associated with a thickening of the ionospheric electron density at and below 90 km altitudes (more like profile 1 in Figure 2.7) suppress elve production as more of the upgoing EMP will reflect before reaching large reduced electric field values. Likewise, irregularities associated with a thinning of the ionospheric electron density at and below 90 km altitudes (more like profile 6) promote elve production as more of the upgoing EMP penetrates to higher altitudes where it can reach higher reduced electric field values.

2.3 Photon Production and Ionospheric Modification

The temporary presence of the EMP at ionospheric D-region altitudes leads to heating of D-region charged particles (i.e., an increase in mean charged particle kinetic energy due to EMP field-driven acceleration). As the background neutral density at D-region altitudes is still much greater than the charged particle density, the charged particle heating immediately results in an increase of the charged particle collision rate with background neutrals. Most of these collisions are of the electron-neutral variety: the smallest positive ions are over 1800 times more massive than electrons and thus the range of motion (and thus heating) of EMP-accelerated positive ions is very restricted

relative to that of EMP-accelerated electrons.

The background neutral composition at D-region altitudes is 79% molecular nitrogen (N_2) and 20% molecular oxygen (O_2), and electron-neutral collisions include both elastic and inelastic collisions with these neutral molecules. Elastic collisions do not involve changes in the energy or internal state of the electron and neutral particle involved and primarily result in returning the distribution of heated electrons to equilibrium. Inelastic collisions do involve changes in the energy and internal state of the electron and neutral particle involved and result in the transfer of energy from the heated electrons to the background neutral population.

Elves, and the associated electron density modification of which elves are an optical signature, are a result of photon production by inelastic electron-neutral collisions. Inelastic collisions can be grouped into three varieties:

1. Electron attachment to neutral molecules (namely, O_2), which decreases the overall electron density
2. Electron impact ionization of neutral molecules, which increases the overall electron density
3. Electron impact excitation of neutral molecules, including rotational, vibrational, and electronic excitation, which can lead to photon production upon relaxation

Table 2.2, compiled from Tables 1 and 2 of [Moss et al. \[2006\]](#), shows a selection of the various types of inelastic electron-neutral collisions (and their associated energy thresholds) found in the D-region ionosphere. Clearly, there are many excited energy states that neutrals can reach through electron impact excitation. Note that the actual outcome of any individual collision event is random and quantum mechanics only provides a description of the probabilities of different outcomes occurring. The energy threshold of a particular outcome is only the energy above which the probability of the outcome becomes nonzero. The actual probability of an outcome is often given as an effective cross-sectional area of the neutral involved in the collision: larger effective cross-sectional areas represent a higher probability of occurrence. While one

could compute collision cross-sections as a function of electron energy from theory, they are more often measured in laboratory settings. Several cross-sections of electron collisions with N_2 and O_2 are tabulated in Appendix 4 of [Rees \[1989\]](#).

Atmospheric neutrals excited by inelastic collisions may relax in two ways:

1. Collisional quenching, in which the acquired energy is lost during a subsequent neutral-neutral collision
2. Photon production, in which the excited neutral spontaneously emits a photon as it relaxes down to a lower energy state

Tables 2.3 and 2.4 summarize the relaxation processes of the lower ionosphere. The processes of Tables 2.3 and 2.4 are associated with the five optical transitions that are most active at elve timescales and altitudes. The radiative lifetime τ_k of a neutral in energy state k is given by $\tau_k = (A_k + \alpha_k^{N_2} N_{N_2} + \alpha_k^{O_2} N_{O_2})^{-1}$. For altitudes above 85 km, $N_{N_2} \leq 10^{14} \text{ cm}^{-3}$ and $N_{O_2} \leq 3 \times 10^{13} \text{ cm}^{-3}$ and the radiative lifetimes are thus less than 10 μs for all five optical emission bands considered in Table 2.3.

Clearly, the response of the D-region electron plasma and neutral population to a suddenly applied electric field involves many processes (heating, elastic and inelastic collisions, excitation, photon production, quenching) acting out over many timescales. Characterizing the overall response in terms of electron density modification and photon production lends itself to Monte Carlo modeling. [Glukhov and Inan \[1996\]](#) used a Monte Carlo model to show that collisions at 90 km in response to an applied electric field return the electron plasma distribution function back to isotropy in $\sim 1 \mu\text{s}$ and quasi-equilibrium in $\sim 1.5 \mu\text{s}$, durations much shorter than the duration of the applied EMP field. This fact, and the short radiative lifetimes of the primary optical emission bands at 90 km, suggest that steady-state solutions of numerical simulations of the D-region response to EMP heating are appropriate tools in studying elves. A popular numerical code used to characterize the D-region response is the ELENDIF Boltzmann code [[Morgan and Penetrante, 1990](#)], based on published collision cross-section data [e.g., [Phelps and Pitchford, 1985](#)]. Figure 2.8 shows ELENDIF results of optical excitation, ionization, and attachment rates as a function of applied electric

Table 2.2: Inelastic electron-neutral collisions in the lower ionosphere, compiled from Tables 1 and 2 of *Moss et al.* [2006].

process	reaction	threshold (eV)	comment
ionization	$e + \text{N}_2 \rightarrow 2e + \text{N}_2^+$	15.60	
	$e + \text{O}_2 \rightarrow 2e + \text{O}_2^+$	12.06	
attachment	$e + \text{O}_2 + \text{A} \rightarrow \text{O}_2^- + \text{A}$	-	3-body
	$e + \text{O}_2 \rightarrow \text{O}^- + \text{O}$	3.7	2-body
rotational	$e + \text{N}_2 \rightarrow e + \text{N}_2(\text{rot})$	0.02	
excitation	$e + \text{O}_2 \rightarrow e + \text{O}_2(\text{rot})$	0.02	
vibrational	$e + \text{N}_2 \rightarrow e + \text{N}_2(\text{vib})$	0.29–2.35	
	$e + \text{O}_2 \rightarrow e + \text{O}_2(\text{vib})$	0.19–0.38	
electronic excitation	$e + \text{N}_2 \rightarrow e + \text{N}_2(\text{A}^3\Sigma_u^+)$	6.17–7.80	
	$e + \text{N}_2 \rightarrow e + \text{N}_2(\text{B}^3\Pi_g)$	7.35	
	$e + \text{N}_2 \rightarrow e + \text{N}_2(\text{W}^3\Delta_u)$	7.36	
	$e + \text{N}_2 \rightarrow e + \text{N}_2(\text{B}'^3\Sigma_u^-)$	8.16	
	$e + \text{N}_2 \rightarrow e + \text{N}_2(\text{a}'^1\Sigma_u^-)$	8.40	
	$e + \text{N}_2 \rightarrow e + \text{N}_2(\text{a}^1\Pi_g)$	8.55	
	$e + \text{N}_2 \rightarrow e + \text{N}_2(\text{w}^1\Delta_u)$	8.89	
	$e + \text{N}_2 \rightarrow e + \text{N}_2(\text{C}^3\Pi_u)$	11.03	
	$e + \text{N}_2 \rightarrow e + \text{N}_2(\text{E}^3\Sigma_g^+)$	11.88	
	$e + \text{N}_2 \rightarrow e + \text{N}_2(\text{a}''^1\Sigma_g^+)$	12.25	
	$e + \text{O}_2 \rightarrow e + \text{O}_2(\text{a}^1\Delta_g)$	0.977	
	$e + \text{O}_2 \rightarrow e + \text{O}_2(\text{b}^1\Sigma_g^+)$	1.627	
	$e + \text{O}_2 \rightarrow e + \text{O}_2(\text{c}^1\Sigma_u^-)$	4.50	
	$e + \text{O}_2 \rightarrow e + \text{O}(^3\text{P}) + \text{O}(^3\text{P})$	6.00	
	$e + \text{O}_2 \rightarrow e + \text{O}(^3\text{P}) + \text{O}(^1\text{D})$	8.40	
	$e + \text{O}_2 \rightarrow e + \text{O}(^1\text{D}) + \text{O}(^1\text{D})$	10.00	
	$e + \text{O}_2 \rightarrow e + \text{O}(^3\text{P}) + \text{O}(^3\text{S}^0)$	14.70	

Table 2.3: Photon production processes in the lower ionosphere, with rate coefficients taken from [Vallance-Jones, 1974, p. 119].

reaction	A_k (s^{-1})	band
$N_2(B^3\Pi_g) \rightarrow N_2(A^3\Sigma_u^+) + h\nu$	1.7×10^5	N_2 1st Positive
$N_2(C^3\Pi_u) \rightarrow N_2(B^3\Pi_g) + h\nu$	2×10^7	N_2 2nd Positive
$N_2^+(A^2\Pi_u) \rightarrow N_2^+(X^2\Sigma_g^+) + h\nu$	7×10^4	N_2^+ Meinel
$N_2^+(B^2\Sigma_u^+) \rightarrow N_2^+(X^2\Sigma_g^+) + h\nu$	1.4×10^7	N_2^+ 1st Negative
$O_2^+(b^4\Sigma_g^-) \rightarrow O_2^+(a^4\Pi_u) + h\nu$	8.5×10^5	O_2^+ 1st Negative

Table 2.4: Collisional quenching processes in the lower ionosphere, with rate coefficients taken from [Vallance-Jones, 1974, p. 119].

reaction	$\alpha_k^{N_2}$ (cm^3-s^{-1})	$\alpha_k^{O_2}$ (cm^3-s^{-1})
$N_2(B^3\Pi_g) + N_2 \rightarrow 2N_2$	10^{-11}	0
$N_2(C^3\Pi_u) + O_2 \rightarrow N_2 + O_2$	0	3×10^{-10}
$N_2^+(A^2\Pi_u) + N_2 \rightarrow N_2^+ + N_2$	5×10^{-10}	0
$N_2^+(B^2\Sigma_u^+) + N_2 \rightarrow N_2^+ + N_2$	4×10^{-10}	0
$O_2^+(b^4\Sigma_g^-) + N_2 \rightarrow O_2^+ + N_2$	2×10^{-10}	0

field strength. In the steady state (and ignoring quenching and cascading, which only mildly affect photon production rates from excited neutrals at elve altitudes and timescales), the photon production rate from energy state k at a given altitude (γ_k) is simply $\gamma_k \simeq \nu_k N_e$, where ν_k is the excitation rate for state k . As reduced electric field strengths do not typically exceed 200 Td (see Figure 2.7f), the N_2 1st Positive band (N_2 1P: $B^3\Pi_g \rightarrow A^3\Sigma_u^+$) of optical emission dominates photon production in elves. As attachment and N_2 1P photon production begin for similar values of applied electric field, detection of N_2 1P photons is a good indicator of EMP-driven electron density modification (especially electron density reduction through attachment).

Figure 2.9 shows x - z slices of simulated photon production and electron density modification for two different EMPs, once again using the FDTD model of Marshall *et al.* [2009]. The left side of Figure 2.9 shows an elve produced by a weaker EMP, and the right side shows and elve produced by a stronger EMP. The top row of Figure 2.9 shows the total number of N_2 1P photons (per unit volume) emitted over the body of the elve, integrated over its lifetime, and the bottom row shows the total change in

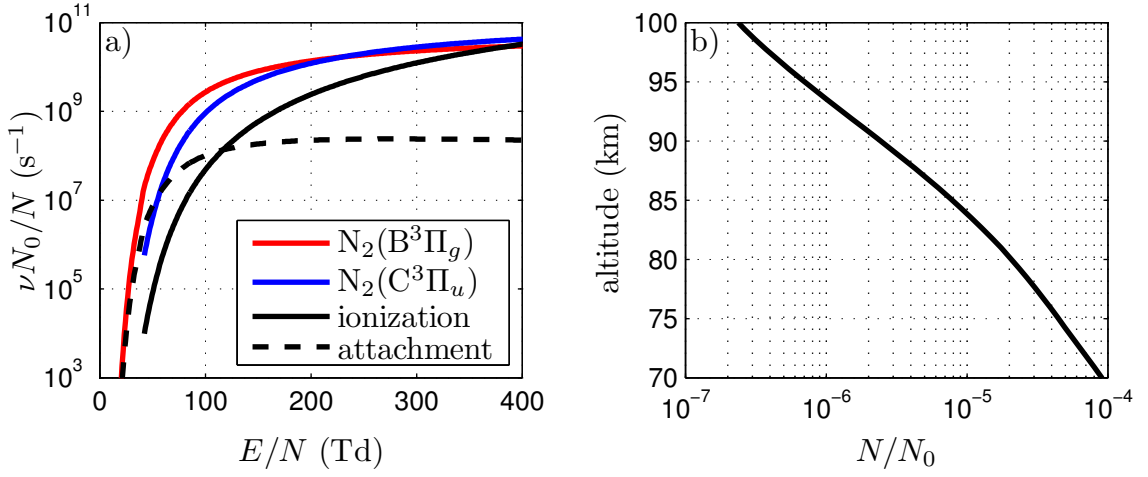


Figure 2.8: (a) Rates of EMP-driven optical excitation and electron density modification in the lower ionosphere, obtained from analytical fits to steady-state ELENDIF Boltzmann code results [Moss *et al.*, 2006]. (b) Normalized neutral density vs. altitude.

electron density over the body of the elve, integrated over its lifetime. For the weaker EMP, the total amount of photon production is smaller, and attachment dominates to decrease the electron density over the body of the elve. For the stronger EMP, the total amount of photon production increases (as expected), and ionization dominates to increase the electron density over the body of the elve. For EMPs falling between the two regimes of Figure 2.9 in terms of strength, the electron density modification can exhibit both attachment and ionization: typically, ionization dominates in the middle of the ring of the elve at lower radii while attachment dominates around the edges.

2.4 Ionospheric Relaxation Chemistry

The reactions considered in the previous section are driven by the presence of an EMP field. In addition to these reactions, there are several more background reactions that take place at all times (with or without an applied EMP field) and which constitute the background ionospheric D-region chemistry. The net effect of these background

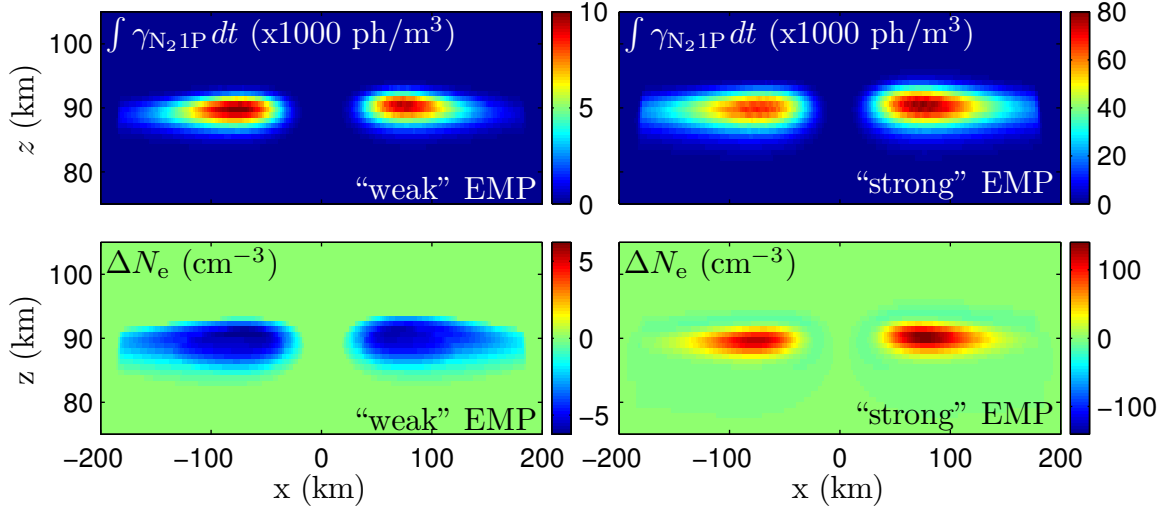


Figure 2.9: Simulated elve photon production and electron density modification. The left side shows results for a weaker EMP, and the right side shows results for a stronger EMP. The top row shows the total number of N_2 1P photons emitted over time, and the bottom row shows the total change in electron density over time. Note the change in color scale between the left and right sides.

reactions is to maintain the D-region ionosphere in a steady state and, upon some perturbing event like lightning EMP-induced heating, to return the D-region ionosphere to its background state.

D-region ionospheric chemistry is quite complex, involving large numbers of chemical species and reactions, many of whose rates are not well understood. In this section, we consider a simplified model of nighttime D-region chemistry first introduced by [Glukhov et al. \[1992\]](#) to study the D-region’s response to lightning-induced electron precipitation (see also [[Pasko and Inan, 1994](#)]). This model has also been used to study D-region heating by ground-based VLF transmitters [[Rodriguez and Inan, 1994](#)] and has recently been extended to study the upper atmospheric response to gigantic jets [[Lehtinen and Inan, 2007](#)].

The model considers five electrically charged species: electrons (whose number density is given by $N_e \text{ cm}^{-3}$), light positive ions (N_+), light negative ions (N_-), heavy positive ion clusters (N_+^c), and heavy negative ion clusters (N_-^c). The chemical processes the model considers can be divided into two categories: charge conversion

processes and charge loss processes. The charge conversion processes are:

1. dissociative electron attachment to neutrals, which essentially converts electrons into light negative ions at the rate $\beta N_e \text{ cm}^{-3}\text{-s}^{-1}$
2. electron detachment from negative ions, which converts light negative ions and heavy negative ion clusters into electrons at the rates $\gamma N_- \text{ cm}^{-3}\text{-s}^{-1}$ and $\gamma^c N_-^c \text{ cm}^{-3}\text{-s}^{-1}$, respectively
3. ion clustering, which converts light negative and positive ions into heavy negative and positive ion clusters at the rates $AN_- \text{ cm}^{-3}\text{-s}^{-1}$ and $BN_+ \text{ cm}^{-3}\text{-s}^{-1}$, respectively

Charge loss processes are:

1. recombination of electrons and positive ions, which eliminate electrons and positive ions (of both the light and heavy cluster varieties) at the rates $\alpha_d N_e N_+ \text{ cm}^{-3}\text{-s}^{-1}$ and $\alpha_d^c N_e N_+^c \text{ cm}^{-3}\text{-s}^{-1}$, respectively
2. mutual neutralization of oppositely charged ions, which eliminate oppositely charged ions (of both the light and heavy cluster varieties) at the rates $\alpha_i N_- N_+ \text{ cm}^{-3}\text{-s}^{-1}$, $\alpha_i N_- N_+^c \text{ cm}^{-3}\text{-s}^{-1}$, $\alpha_i N_-^c N_+ \text{ cm}^{-3}\text{-s}^{-1}$, and $\alpha_i N_-^c N_+^c \text{ cm}^{-3}\text{-s}^{-1}$, respectively

Figure 2.10 illustrates the species and processes considered by the model. The model solves the following system of differential equations:

$$\frac{\partial N_e}{\partial t} = Q - \beta N_e + \gamma N_- + \gamma^c N_-^c - (\alpha_d N_+ + \alpha_d^c N_+^c) N_e \quad (2.41)$$

$$\frac{\partial N_-}{\partial t} = \beta N_e - \gamma N_- - \alpha_i (N_+ + N_+^c) N_- - AN_- \quad (2.42)$$

$$\frac{\partial N_+}{\partial t} = Q - \alpha_d N_e N_+ - \alpha_i (N_- + N_-^c) N_+ - BN_+ \quad (2.43)$$

$$\frac{\partial N_-^c}{\partial t} = -\gamma^c N_-^c - \alpha_i (N_+ + N_+^c) N_-^c + AN_- \quad (2.44)$$

$$\frac{\partial N_+^c}{\partial t} = -\alpha_d^c N_e N_+^c - \alpha_i (N_- + N_-^c) N_+^c + BN_+ \quad (2.45)$$

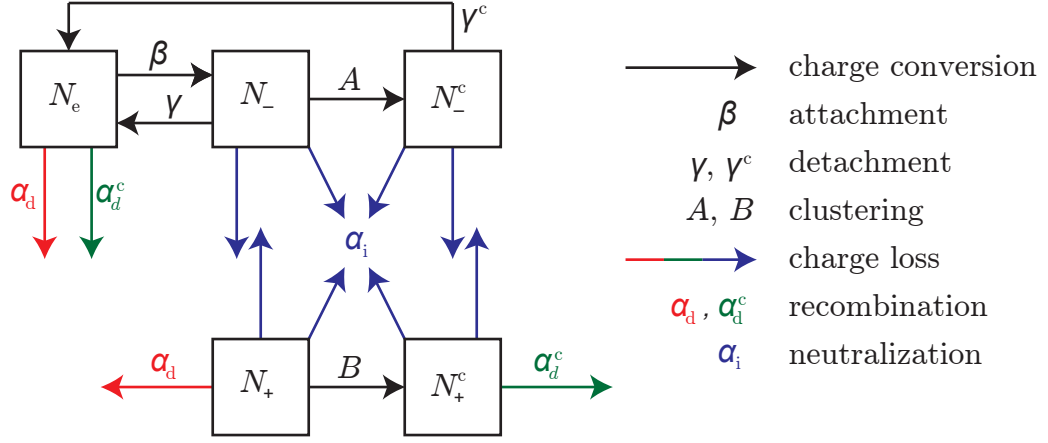


Figure 2.10: Five-species model of D-region ionospheric chemistry. Species considered are electrons (N_e), light negative and positive ions (N_- and N_+), and heavy negative and positive ion clusters (N_-^c and N_+^c). Charge conversion processes appear in black and charge loss processes appear in color. The model is developed in [Glukhov et al. \[1992\]](#) and extended in [Lehtinen and Inan \[2007\]](#).

where Q is the background ionization rate and the other variables are as defined above.

Figure 2.11 shows the altitude profiles of a few of the important rate parameters. Of particular note is the large amount by which the detachment rate γ exceeds the dissociative attachment rate β . In the steady state, the actual rates of dissociative attachment and detachment offset each other (due to the relatively large number of electrons available for dissociative attachment and the small number of negative ions available for detachment) so that there is no net change in the electron and negative ion populations. But in the event of a sudden increase in the negative ion population and an equivalent decrease in the electron population (say, due to externally-driven attachment produced by EMP heating), the large detachment rate quickly drives the two populations back to equilibrium (i.e., the newly attached electrons that drove up the negative ion population quickly detach and return to being free electrons). We discuss this effect in more detail below.

Note that over the 80–100 km altitude range of interest, $\gamma^c \simeq 0 \text{ s}^{-1}$. Additionally, $\alpha_d \simeq 6 \times 10^{-7} \text{ cm}^3\text{-s}^{-1}$, $\alpha_d^c \simeq 10^{-5} \text{ cm}^3\text{-s}^{-1}$, and $\alpha_i \simeq 10^{-7} \text{ cm}^3\text{-s}^{-1}$, meaning that

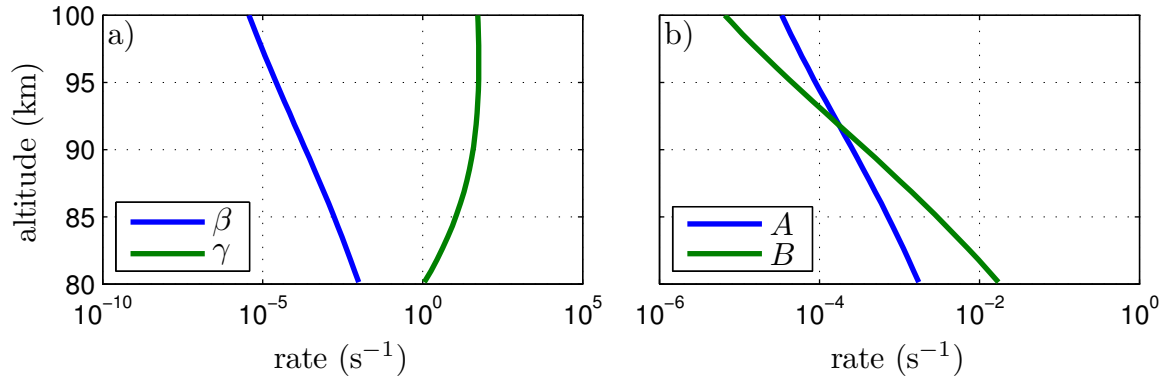


Figure 2.11: Altitude profiles of rates of ionospheric chemistry processes. (a) Rate profiles of electron attachment to neutrals (β) and electron detachment from light negative ions (γ). (b) Rate profiles of conversion of light negative ions to heavy negative ion clusters (A) and of light positive ions to heavy positive ion clusters (B).

(assuming all involved species are equally available) charge neutralization is much slower than electron recombination with positive ions (especially heavy positive ion clusters).

Figure 2.12 shows the relaxation of all five particle populations at 80–100 km altitudes in response to a sudden increase in the electron and light positive ion populations (an ionization event). Above ~ 85 km, the populations relax back to background levels primarily through recombination of electrons and light positive ions. Below ~ 85 km, the newly created light positive ions quickly convert to heavy positive ion clusters before relaxing through recombination of electrons and heavy positive ion clusters. The negative ions experience very little change during an ionization event. At all altitudes, the ionosphere chemically relaxes from ionization events on a timescale of tens of minutes.

Figure 2.13 shows the relaxation of all five particle populations at 80–100 km altitudes in response to a sudden increase in the light negative ion population and an equivalent decrease in the electron populations (an attachment event). The dominant effect at all altitudes is subsequent detachment of newly-attached electrons, quickly returning the electron and light negative ion populations back to the background levels (as described above). The relaxation timescale is less than 1 second at all

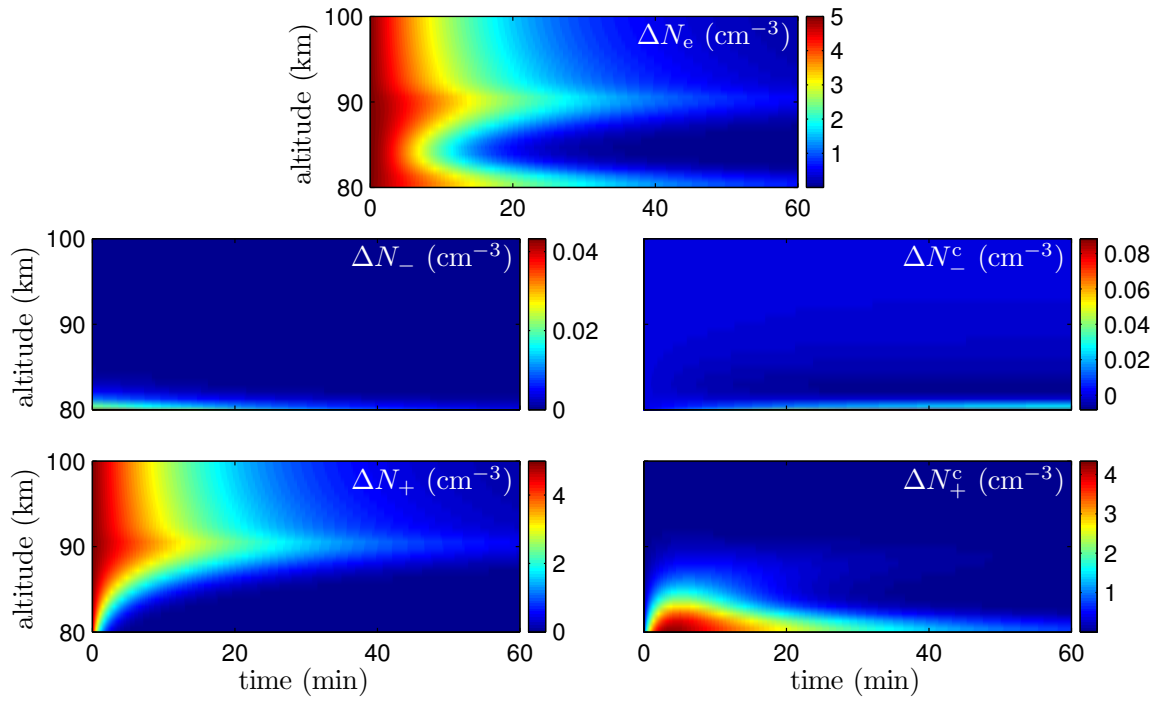


Figure 2.12: Ionospheric relaxation after an ionization event. A 5 cm⁻³ increase in the electron density (N_e) and light positive ion density (N_+) was applied suddenly at all altitudes at time $t=0$, and the difference between the species densities and their background levels is plotted over time.

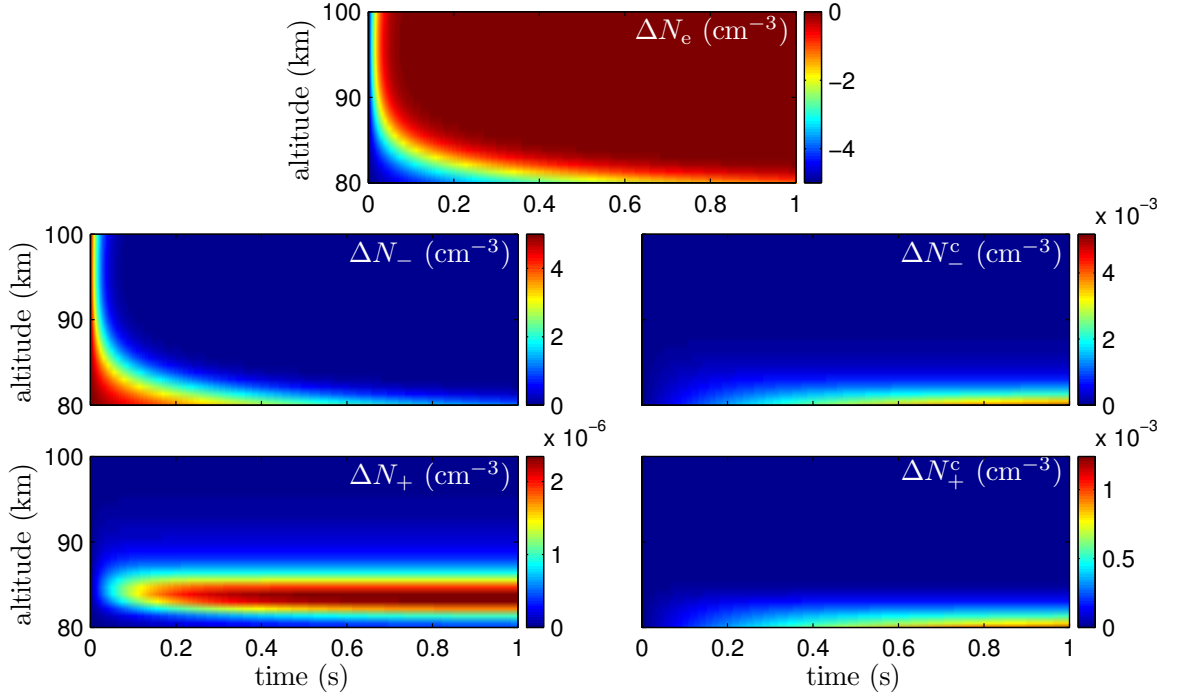


Figure 2.13: Ionospheric relaxation after an attachment event. A 5 cm^{-3} decrease in the electron density (N_e) and an accompanying 5 cm^{-3} increase in the light negative ion density (N_-) was applied suddenly at all altitudes at time $t=0$, and the difference between the species densities and their background levels is plotted over time.

altitudes in the 80–100 km range, with faster relaxation occurring at higher altitudes. Admittedly, the relaxation timescale is strongly dependent on the detachment rate profile which is not generally known with great accuracy [*Pasko and Inan, 1994*]. To the degree that the detachment rate profile can vary from that used in this section (presented in Figure 2.11), the attachment event relaxation time constant could vary as well.

Figure 2.13 suggests that attachment driven by EMP-heating is only a temporary effect, quickly cleared by ionospheric chemistry after the event. There is little opportunity for a buildup of EMP-driven attachment (without ionization) in the ionosphere due to bulk lightning activity over storm timescales. On the other hand, EMP-driven ionization can persist for tens of minutes and bulk lightning activity can readily cause buildup of ionization in the ionosphere over storm timescales.

Chapter 3

Photometric Imaging of Elves

In this chapter, we introduce in detail the PIPER photometric imager and the imaging concept on which it was designed and built. We then discuss the nature of high speed elve imaging and the difficulties involved in interpreting high speed elve data (which are common to all high-speed imaging instruments, not just PIPER). We then develop an approach for interpreting high-speed elve data as recorded by PIPER and present an analysis of the technique's performance.

3.1 The PIPER Instrument

PIPER (Photometric Imager of Precipitation of Electron Radiation, shown in Figure [3.1](#)) is a high-speed, multi-anode photometer array designed (by Robert Marshall) and built (by Robert Marshall and the author of this dissertation) at Stanford initially for the purpose of studying optical signatures of heater- and transmitter-induced radiation belt electron precipitation into the upper atmosphere (hence the name). However, it was soon realized that PIPER could double as a photometric imager for TLEs in the summer seasons, and the instrument proved exceedingly capable of recording otherwise difficult-to-capture elves in its first TLE observation campaign in the Summer of 2007.

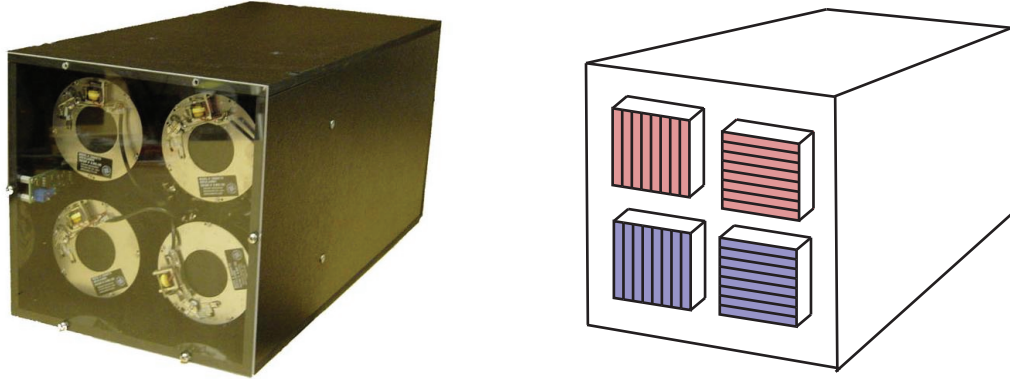


Figure 3.1: (left) The PIPER instrument, viewed from the front. (right) An outline of the PIPER instrument showing the placement of the two photometer pairs (red and blue) and the individual photometer orientations (horizontal and vertical).

3.1.1 The Photometric Imaging Concept

PIPER is composed of four 16-anode photometer arrays all aimed at the same field of view and operating in pairs. (By “16-anode photometer array” or simply “photometer”, we mean 16 photomultiplier tubes sharing the same voltage supply and housing.) For each of the four photometers, the 16 photosensitive cathodes are rectangularly shaped and arranged in a line (a hypothetical pair of 8-anode photometers are shown in Figure 3.2a). We orient one of the photometers in each pair so that its cathodes spread horizontally (the horizontal photometer, on the left in Figure 3.2a) and the other so that its cathodes spread vertically (the vertical photometer, on the right in Figure 3.2a). The cathodes of the horizontal photometer integrate the field of view vertically and together provide (at high speeds) information about how light is distributed horizontally in the field of view. Likewise, the cathodes of the vertical photometer integrate the field of view horizontally and together provide (at high speeds) information about how light is distributed vertically in the field of view.

Thus, at any instant in time, a pair of photometers divides the field of view in two ways: the horizontal photometer divides it into vertical columns while the vertical photometer divides it into horizontal rows. Referring to Figure 3.2b, if the light is distributed over the gray field of view according to the numbers (in arbitrary linear units), the horizontal photometer records the “sums of the columns” of the field of

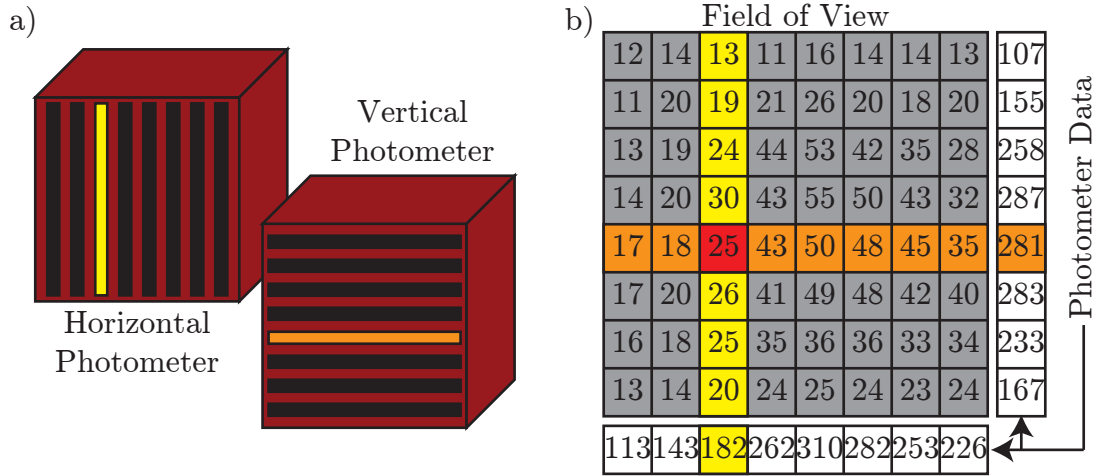


Figure 3.2: (a) A horizontal (left) and vertical (right) photometer, showing the shape and orientation of the photosensitive cathodes. (b) Illustration of the field of view division of each photometer and what each records.

view (the sums along the bottom), and the vertical photometer records the “sums of the rows” of the field of view (the sums down the right). Taken together, these two photometric measurements along single (but orthogonal) dimensions of the field of view provide information about how light was distributed in both dimensions of the field of view.

Each photometer in a pair sits behind the same optical filter as the other, and different pairs sit behind different filters. In practice, we commonly use a longpass red (i.e., passes wavelengths longer than 650 nm) optical interference filter for one pair and a wideband blue optical interference filter for the other when imaging TLEs. Thus, in total, the 64 photomultiplier tubes that comprise PIPER act as a 16-anode photometer array repeated in both the horizontal and vertical directions and repeated again at two separate wavelengths passbands.

3.1.2 Instrument Details

Figure 3.3 shows a top-down and side-on schematic view of the PIPER instrument. The front of the instrument is dominated by optics while the back of the instrument is devoted to signal conditioning.

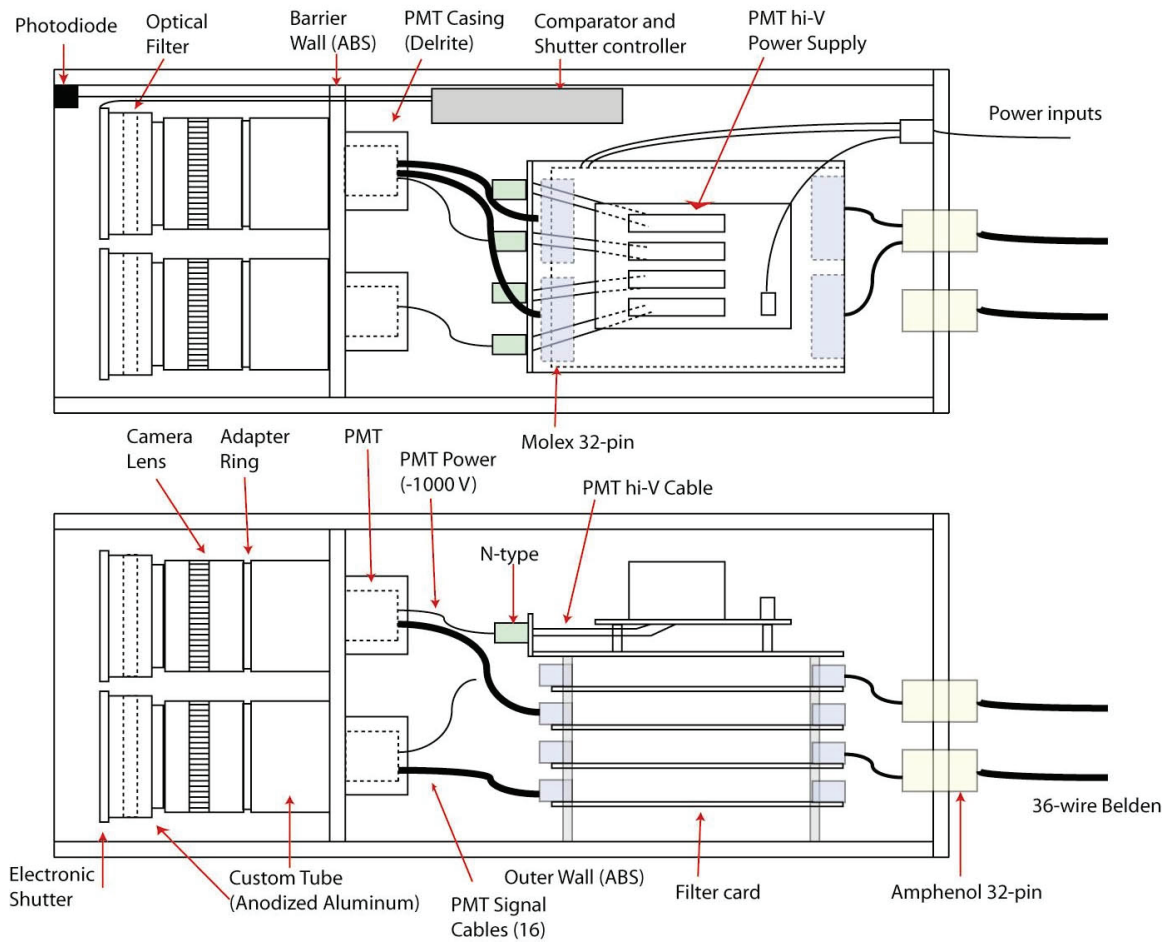


Figure 3.3: A top-down (top) and side-on (bottom) schematic view of the inside of the PIPER instrument.

Each photometer sits behind a chain of optical components. These components, in the order through which a photon passes as it enters the instrument, are:

1. An electronically-controlled shutter, opened and closed by the operator via a switch but automatically closed in case the precautionary photodiode mounted at the front of the instrument detects a sudden increase in the ambient light level (which protects the photometers against accidental damage by direct flash-light exposure, etc.).
2. An optical interference filter. For the “red” photodiodes, we use a longpass (>650 nm) filter to allow for collection of N_2 1P band photons. For the “blue” photometers, we use an 80 nm bandpass filter centered at 400 nm to allow for collection of N_2^+ 1N band photons.
3. A 50 mm f/1.4 Cannon lens, allowing for an $\sim 18^\circ$ square field of view.

The photometers themselves are Hamamatsu R5900U-20-L16 photomultiplier tube arrays, made of multialkali photocathodes behind borosilicate glass windows and sensitive over the 300–900 nm wavelength range. The cathode spectral quantum efficiency (the number of electrons yielded by the cathode per incident photon of given wavelength) peaks (0.18 electrons per photon) at a wavelength of 500 nm; its full-width half-minimum (FWHM) spans the 400–780 nm wavelength range. Each cathode covers a 0.8×16 mm effective area, and all the cathodes are arranged contiguously over the front surface of the photometer with a nominal 3% cross-talk expected between adjacent channels. Cathode-generated electrons are accelerated through -700 V along a 10-stage metal channel dynode for a nominal electron number gain of 3×10^5 . The cathode-to-anode step response rise time is nominally 0.6 ns, much faster than the μ s timescales of elve events we are interested in measuring. The dark current referred to the anode is nominally 1 fA, a negligible amount compared to the magnitude of even a dim elve signal. The R5900U-20-L16 is a close cousin of the R5900U-01-L16, used successfully on board ISUAL [[Chern et al., 2003](#)] and in winter TLE observation campaigns in Japan [[Takahashi et al., 2003](#)].

The photometer gain stages are powered by four Hamamatsu C4900 high-voltage power supplies (one for each photometer), capable of producing a -1200 V bias voltage from a 15 V input. The actual output is controlled through potentiometer settings, which are set for -700 V during TLE observation campaigns. The output current signals from each of the 64 photometer anodes are run through separate four-pole Chebyshev low-pass anti-aliasing filters (with a cutoff frequency at 12 kHz) before being carried off-instrument to be sampled.

The 64 photometer anode signals are sampled at 25 kHz sampling rates by two National Instruments PCI-6254 16-bit DAQ cards sharing the same GPS-time synchronized sample clock produced by an XL-AK GPS clock. Data acquisition software developed in-house at Stanford interfaces the DAQ cards, GPS clock, and hard drive(s) to digitize and timestamp the data and record it for permanent storage. All data is recorded (there is no triggering of data retrieval), and accumulates at a rate of ~ 11 GB-hr $^{-1}$. Given typical storm lifetimes and numbers of days between big storms, a 1 TB hard drive can store several weeks of PIPER TLE campaign data. The data is mined afterward and events of interest (elves, halos, sprites, etc.) are located and tagged for easy reference. All campaign data is archived for future analysis.

More details about the PIPER instrument can be found in [Marshall et al. \[2008\]](#).

3.1.3 Field of View

The PIPER instrument has an 18° field of view. As elves occur at around $h=90$ km altitude, an elve can be observed at most at a ground range r of

$$r = R_E \cos^{-1} \left(\frac{R_E}{R_E + h} \right) = 1065 \text{ km} \quad (3.1)$$

(where $R_E = 6378$ km is the Earth radius) before the center of the event dips below the horizon. For this reason, we define the direct field of view of PIPER as a wedge of 18° extending out to ~ 1000 km ground range.

However, elves have significant radial extent (typically ~ 150 km) meaning that elves just outside the direct field of view can still leak into the direct field of view of PIPER and be detected. To compensate for this feature, we add a 150 km border to

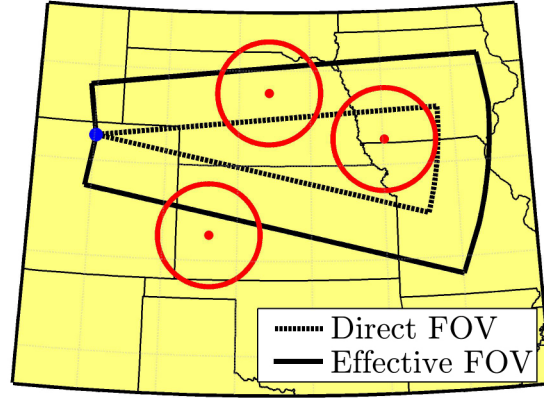


Figure 3.4: PIPER field of view definitions. The direct field of view is the region directly visible by the PIPER photometer anodes. The effective field of view is that region in which an originating elve should produce a PIPER detection (either directly, or due to the edge of the elve leaking into the direct field of view).

the direct field of view and declare this area as the effective field of view of PIPER: in other words, any elve centered in this region should be detectable. Admittedly, dim elves just on the inside edge of this region may not actually leak into the direct field of view while especially bright elves occurring just outside this region may actually leak into the direct field of view. We take the 150 km value for the border thickness as a compromise between these cases. Figure 3.4 illustrates the direct and effective field of view definitions.

The surface area of the Earth contained in the effective field of view of PIPER is roughly 2.4×10^6 km².

3.1.4 Example Data

At any instant in time, a pair of PIPER photometers records the horizontal and vertical integration of light in its 2D field of view; these recordings accumulate over time to form the PIPER data product. Figure 3.5 presents a TLE occurring on July 10, 2007 from the Yucca Ridge Field Site near Ft. Collins, CO and recorded by PIPER's pair of red-wavelength photometers and illustrates how PIPER data is

presented throughout this work. (Six 17 ms fields of intensified video-rate camera data from the same event are shown in Figure 3.6.) Figure 3.5a shows a 50 ms segment of PIPER data taken from the red vertical photometer (including a zoom-in on a particular 2 ms interval within this segment). Likewise, Figure 3.5b shows the same 50 ms segment of PIPER data taken from the red horizontal photometer (including a zoom-in on a particular 2 ms interval within this segment). Note the choice in axes. For vertical photometer data (which records the vertical distribution of light in the field of view), time proceeds from left to right so that the vertical distribution of light appears vertically-oriented in the figure. For horizontal photometer data (which records the horizontal distribution of light in the field of view), time proceeds from top to bottom so that the horizontal distribution of light appears horizontally-oriented in the figure. The color scale is in arbitrary linear units and is proportional to the flux of photons incident upon a given photometer cathode at a given instant in time.

Figure 3.5 also illustrates a number of the high-speed events PIPER is capable of resolving. The TLE shown in Figure 3.5 includes an elve (identifiable by its characteristic downward arc in vertical data and flattened arc in horizontal data), a sprite halo, and sprite tendrils. PIPER shows a few-ms gap between the end of the halo and the beginning of the sprite, and can also resolve the 120 Hz flicker of a fluorescent light on the horizon that showed up along the bottom of the field of view. In conventional video-rate camera data, high-speed features like the elve and halo, the gap between the halo and sprite, and the flicker of the horizon light cannot be resolved (Figure 3.6). These features are difficult to resolve even in high-speed cameras if slow-response intensifiers are used (note the effect of the intensifier response in Figure 3.6 in causing the sprite brightness to persist several more fields after PIPER shows the event to be over).

Figure 3.7 shows more examples of TLEs as recorded from Langmuir Laboratory on various days in July 2008 by PIPER’s pair of red-wavelength photometers. The top two panels show the vertical and horizontal photometer data for a single elve, the middle two panels show the vertical and horizontal photometer data for an elve followed by a halo, and the bottom two panels show the vertical and horizontal photometer data for a so-called “elve doublet” (see Chapter 5).

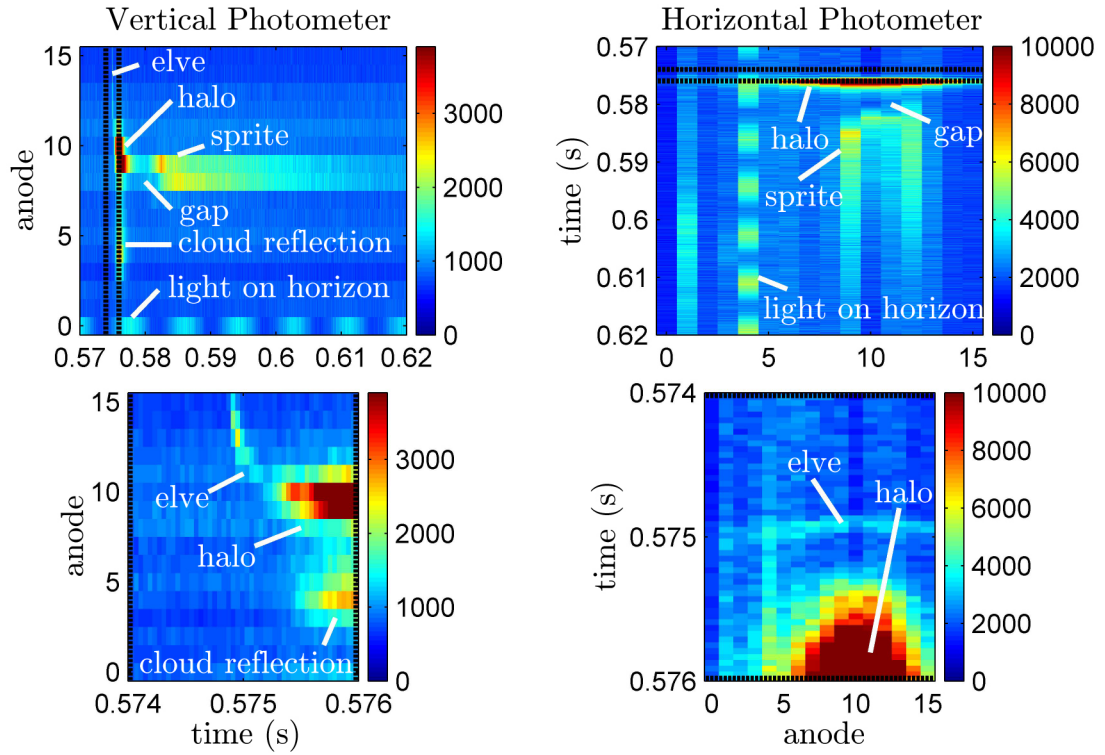


Figure 3.5: An example TLE as recorded in PIPER's pair of red-wavelength photometers: (a) 50 ms of vertical photometer data and a 2 ms zoom-in of the data, and (b) 50 ms of horizontal photometer data and a 2 ms zoom-in of the data.

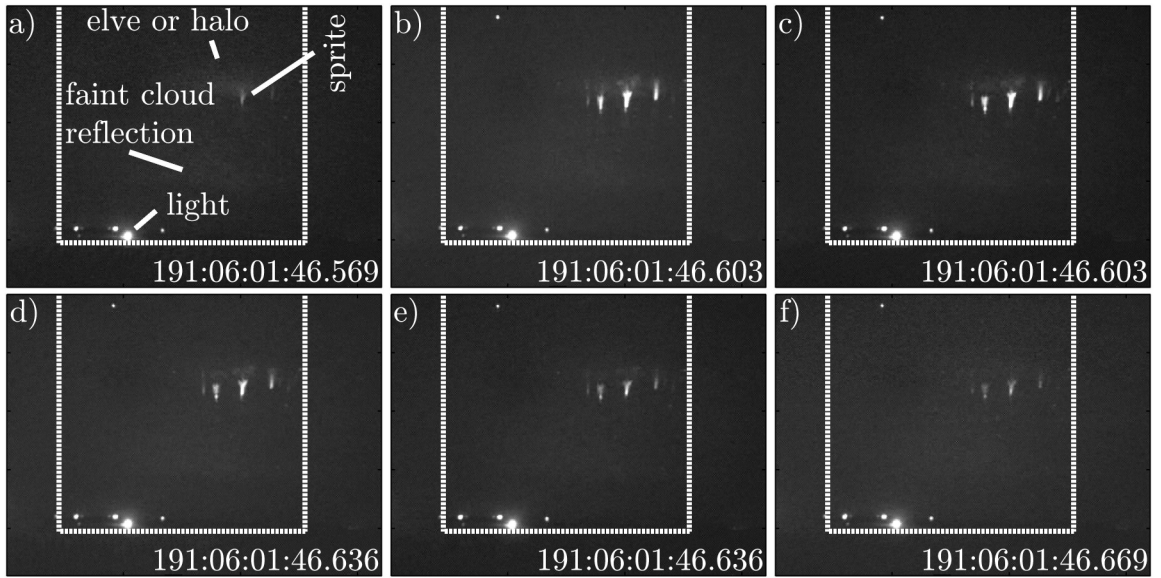


Figure 3.6: Six 17 ms fields of the same TLE as in Figure 3.5 with the PIPER field of view outline shown. The GPS frame timestamps are shown, updated every other field. The PIPER data of Figure 3.5 corresponds roughly to the fields in the top row. Note that the intensifier causes the sprite luminosity to persist for several fields after the event.

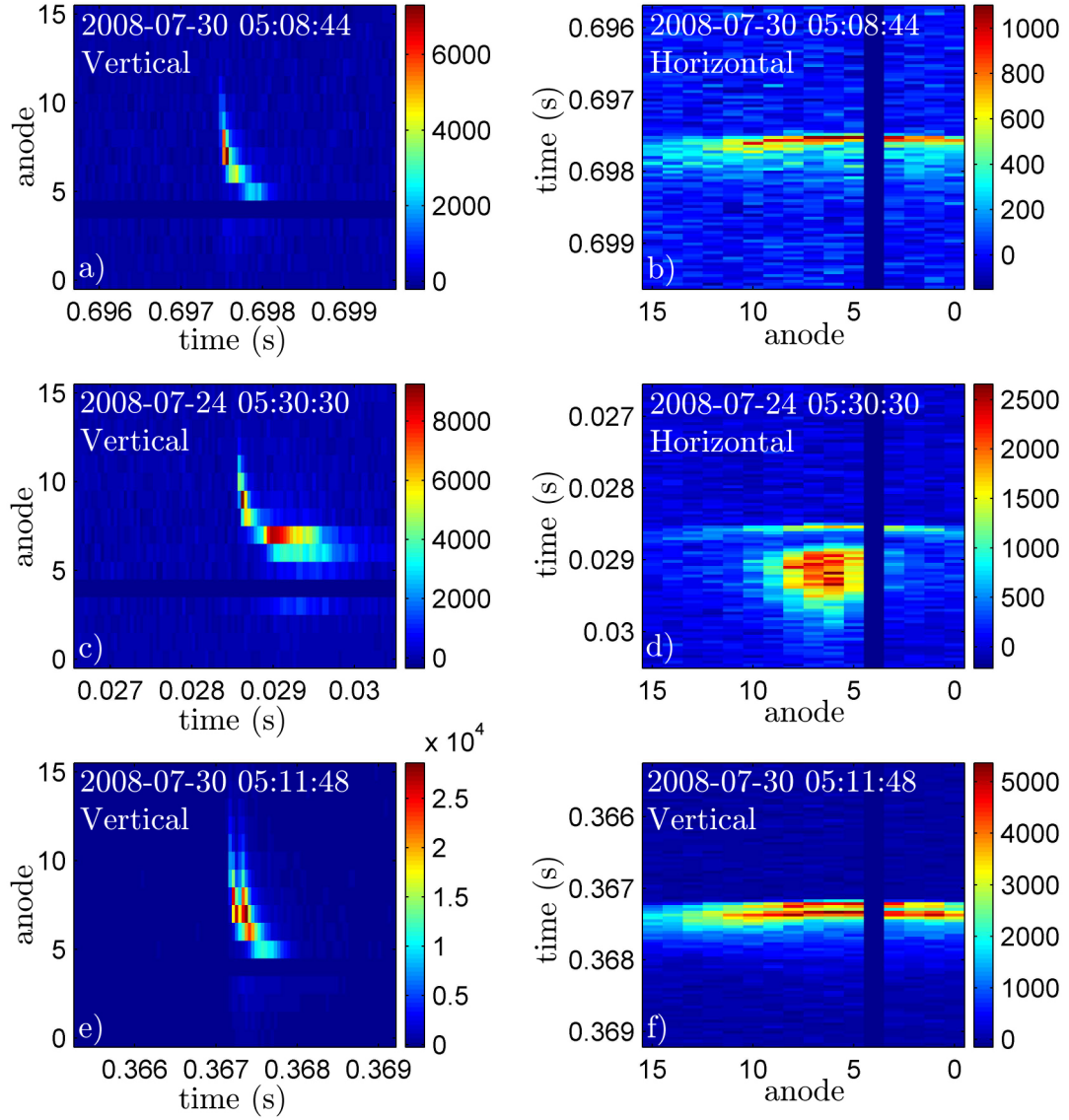


Figure 3.7: (a,b) Vertical and horizontal photometer data for a single elve. (c,d) Vertical and horizontal photometer data for an elve followed by a halo. (e,f) Vertical and horizontal photometer data for an elve doublet.

Without considering the fact that Figure 3.7a and 3.7b are the signatures of an elve, one might interpret them as follows: light first appears at the top center of the field of view and splits into two sources that drift to the right and left while rapidly moving downward in the field of view. This interpretation is very similar to the initial interpretation of the first elve observations of *Fukunishi et al.* [1996] (which were two-photometer versions of Figure 3.7a). There is not much evidence in Figures 3.7a and 3.7b to suggest the expanding luminous ring of an elve. The temporal sharpening and smearing of the received light intensity makes this effect not observable without prior (or theoretical) knowledge of the underlying production mechanism of the photon emission. We discuss this effect in more detail in the next section.

3.2 High-Speed Imaging of Elves

Elves are most commonly observed with photometers, photometer arrays, and cameras. For single-anode photometers (which have very high temporal resolution but no real spatial resolution), an elve is merely a brief pulse in the photomultiplier tube anode current, and interpretation of the dynamics of the geometry of the observed elve is not usually possible. For low-speed (e.g., 60 field-s⁻¹ video-rate) cameras (which have very high spatial resolution but relatively low temporal resolution), the entirety of the elve appears within the integration time of a single video frame, and interpretation of the temporal dynamics of the geometry of the observed elve is not usually possible.

High-speed cameras (capable of observing several frames within the 1–2 ms elve lifetime) and multi-anode photometer arrays present the opportunity for observing elve geometry as it unfolds over the event lifetime. For this reason, both high-speed cameras and, especially, photometer arrays have become increasingly popular tools in the study of elves. Care must be taken, however, in interpreting data from these instruments.

As mentioned in previous chapters, the horizontal (or lateral) expansion rate of the luminous circle that makes up an elve exceeds the speed of light (and also the emitted photon propagation velocities). Consider Figure 3.8. As a photon is emitted

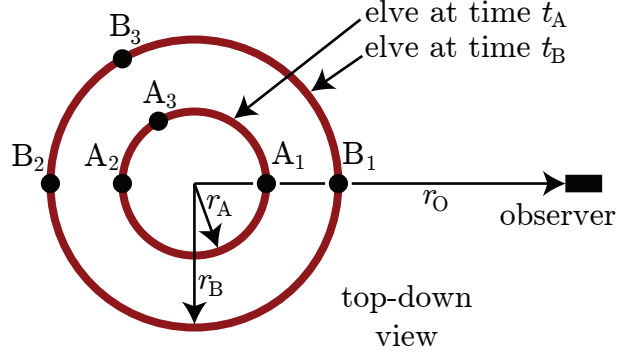


Figure 3.8: Schematic illustration of the photon delay effect.

from point A_1 at time t_A of the evolution of an elve, it starts to propagate toward the remote observer at the speed of light while the elve (i.e., the source region of the photons) moves on ahead of it. A photon emitted later from point B_1 at time $t_B > t_A$ actually arrives at the observer before the photon emitted from point A_1 because the faster-than-light expansion of the elve in the direction of the observer gives it a head start. In this case, photons emitted in the time order t_A, t_B arrive at the observer in reverse order.

Alternatively, considering photons emitted from points A_2 and B_2 , the faster-than-light lateral expansion of the elve results in photons that were emitted with initial time separation $\Delta t_{BA} = t_B - t_A$ arriving at the observer in the same order but with an increased time separation. In the general case (say, points A_3 and B_3), the time separation of the two photons at the observer is a non-trivial function of the time separation of two photon emission times, the elve geometry, and the viewing geometry. This effect, which is a direct consequence of the fact that the elve expansion rate is a non-negligible fraction of the photon propagation velocity (the speed of light), leads to temporal sharpening or piling up (focusing) and smearing (defocusing) of intensity in observational data, depending upon which portion of the elve is viewed. We refer to this effect as the “photon delay” effect as one can account for it by properly accounting for the delay in a photon’s arrival time relative to its emission time. The photon delay effect is not a problem particular to a specific instrument, but rather manifests itself in any imaging instrument with enough temporal resolution to observe

the elve multiple times over its lifetime.

Figure 3.9 shows a sequence of frames from a fictional high-speed camera observing a simulated elve from the ground at a 500 km distance. The left column of Figure 3.9 shows the view one might first expect if not considering the photon delay effect. The circular expansion of the elve over time is immediately apparent, and the dynamics of the elve geometry (its radius over time, total duration, etc.) is readily observed. The middle column of Figure 3.9 shows the actual view of the same elve, including the photon delay effect. Instead of an expanding ring, the photon delay effect causes the elve to appear as a downward descending arc, and also explains the particular appearance of an elve signature in PIPER data (also shown in Figure 3.9) appears the way it does.

3.3 Elve Photon Emission Profiles

In light of the photon delay effect, it is difficult to discern the dynamics of the geometry of an elve from its signature in PIPER data (e.g., Figures 3.7a and 3.7b). In Figure 3.10, we present a more natural view of an elve (cf. [Inan *et al.*, 1996, Figure 2d]). We assume that an elve is an azimuthally symmetric expanding luminous ring roughly confined to a single altitude. We consider only the luminosity in a single direction and plot the photon volume emission rate (indicated by color) along the radius in that direction (the vertical axis of Figure 3.10) as time progresses (from left to right on the horizontal axis of Figure 3.10). For the rest of this work, we refer to this type of view of an elve as its photon emission profile, and in the following sections we describe how to recover an approximation of an elve photon emission profile from its photometer array observation.

The photon emission profile of Figure 3.10 provides for much easier extraction of important geometric parameters of the elve. The elve duration, total elve radius, and hole radius (all denoted on Figure 3.10) can be trivially read from the photon emission profile. The same is true for the volume emission rate over time. The elve expansion rate at a given time instant is simply the slope of the curve of the emission profile at that instant. None of these parameters (with the possible exception of the total

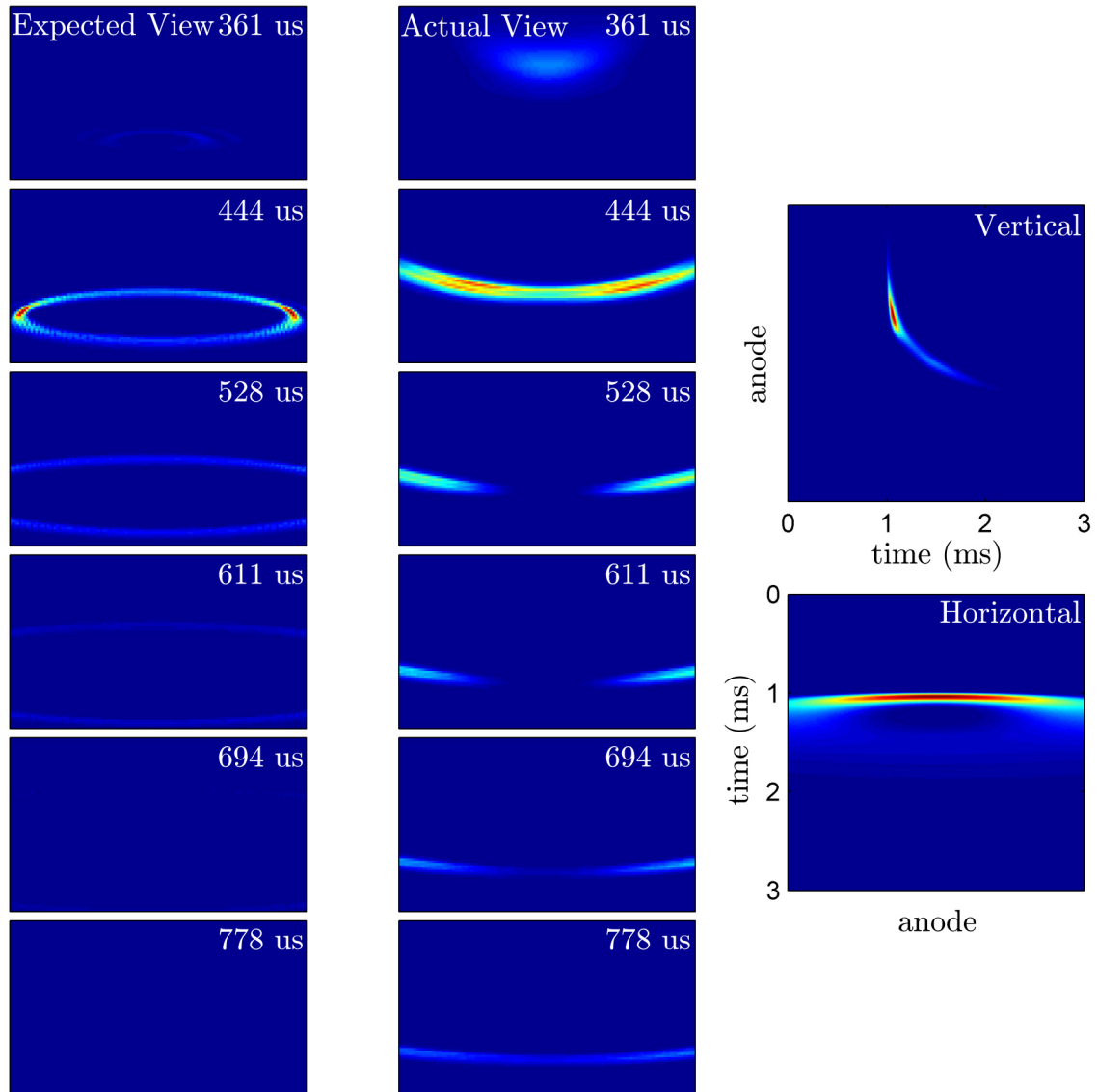


Figure 3.9: (left column) Series of simulated high-speed camera frames of a developing elve, without including the photon delay effect. (middle column) Same as the left column, but including the photon delay effect. (right column) Simulated photometer array data for the same developing elve, including the photon delay effect.

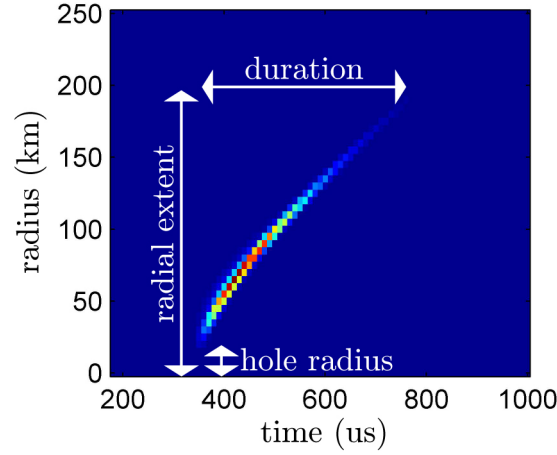


Figure 3.10: The photon emission profile of an elve.

elve radius if the elve completely fits in the instrument field of view, which is usually not the case in PIPER data) can be easily extracted from the raw photometric array data of Figures 3.7a and 3.7b. Thus, obtaining the photon emission profile of an elve is an important step in quantifying the particular geometric features of the elve.

3.4 Recovering Photon Emission Profiles

In this section, we describe an algebraic reconstruction technique for recovering an estimate of the photon emission profile of an elve from its photometric array observation data. We consider our photometric array data to be a known vector y and our desired emission profile to be an unknown vector x . Assuming we know our viewing geometry exactly, we can construct a matrix A that describes the mapping of any emission profile to photometric array data as $y = Ax + \epsilon$ (where ϵ is a measurement noise vector whose elements are assumed to be small in magnitude). We recover x by solving a regularized optimization problem (a standard technique; see, e.g., [Karl \[2000\]](#)) that includes a data fidelity objective, a quadratic smoothness regularization term, and the constraint that x be element-wise nonnegative.

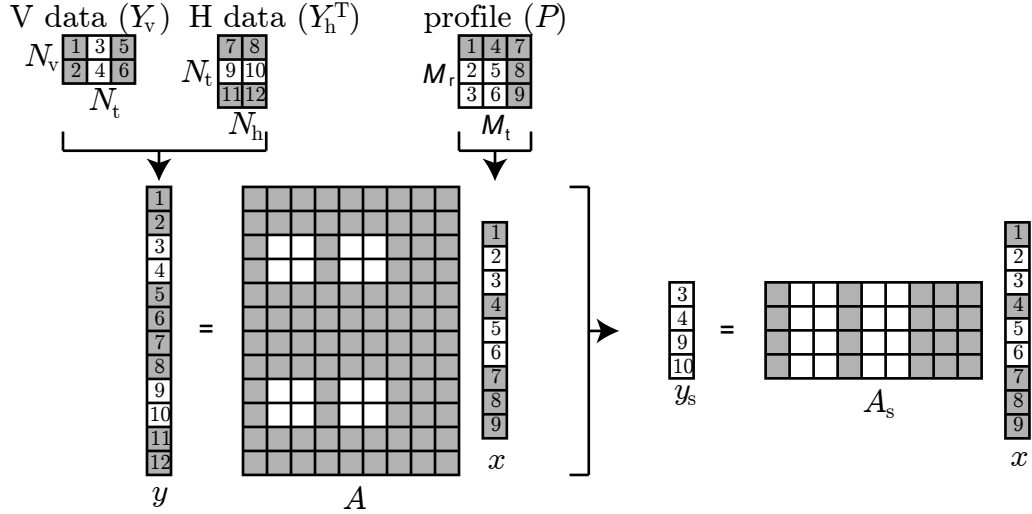


Figure 3.11: Formation of x , y , and A for the case of $N_t = 3$, $N_h = N_v = 2$, and $M_r = M_t = 3$. The thresholding process was applied to y and $I = \{3, 4, 9, 10\}$ was the set of y element locations containing the elve signal; y_s and A_s were then constructed from only these elements/rows.

3.4.1 Approach

Consider N_t samples of an observed elve taken from a photometric array containing N_h horizontally-oriented anodes and N_v vertically-oriented anodes. If we were to display such data as in Figure 3.7a and 3.7b, the vertical data would be a $N_v \times N_t$ image and the horizontal data would be a $N_t \times N_h$ image. If we denote the vertical observation data image as $Y_v \in \mathbb{R}^{N_v \times N_t}$ and the horizontal observation data image as $Y_h \in \mathbb{R}^{N_h \times N_t}$ (notice we usually display the transpose of Y_h when viewing the data as an image), we can consolidate our entire observation into a single vector $y \in \mathbb{R}^{N_t(N_v + N_h)}$ using the matrix $\text{vec}()$ operator as $y = \text{vec}([Y_v, Y_h])$. Likewise, consider a photon emission profile defined on a support containing M_r radial points and M_t time points. If we were to display such a profile as in Figure 3.10, the profile would be a $M_r \times M_t$ image. If we denote the profile image as $P \in \mathbb{R}^{M_r \times M_t}$, we can consolidate our profile into a single vector $x \in \mathbb{R}^{M_r M_t}$ as $x = \text{vec}(P)$. Figure 3.11 illustrates this formulation for the case of $N_t = 3$, $N_h = N_v = 2$, and $M_r = M_t = 3$.

Because the elements of y (each individual photometric array observation) are

a linear function of the elements of x (each one of which can be interpreted as a luminous ring of a given radius appearing suddenly at a given time), there is a matrix $A \in \mathbb{R}^{N_t(N_v+N_h) \times M_r M_t}$ that defines the contribution that each element of x makes in y . (A description of how to construct A can be found in the Appendix.) Thus, we have a linear observation equation $y = Ax + \epsilon$, where y is known, A is known exactly if the viewing geometry is known exactly, x is unknown, and $\epsilon \in \mathbb{R}^{N_t(N_v+N_h)}$ is a measurement error vector whose elements are assumed to be small relative to the elements of Ax .

Our approach is to find a vector x that is consistent with our observation vector y and is consistent with any *a priori* characteristics a photon emission profile should have. As a first pass, this task can be accomplished by solving the convex optimization problem

$$\begin{aligned} & \text{minimize} && ||y - Ax||_2 + \lambda ||D_u x||_2 \\ & \text{subject to} && x \succeq 0 \end{aligned} \tag{3.2}$$

Here, the objective to be minimized has two terms. The first term is a data fidelity term that penalizes (becomes large) vectors x that are less consistent with the observation y . The second term is a regularization term that penalizes non-smooth emission profiles. We know that any physical photon emission profile should be smoothly varying as the expansion of the luminous ring of the elve in the atmosphere is continuous (i.e., it cannot have a radius of 35 km at one instant and then have a radius of 16 km at the next, but rather should have a continuously increasing radius at time progresses). Because the elve expands at a velocity similar (to within an order of magnitude) to the speed of light, we expect our smoothness assumption to especially hold true in the u direction (at an angle to both the t and r axes), where $u = 0.3 \text{ km-}\mu\text{s}^{-1}$. (Recall that directions on an emission profile can be interpreted as velocities, with nearly vertical directions corresponding to high velocities and nearly horizontal directions corresponding to low velocities.) The matrix D_u estimates at each point of the emission profile a weighted sum of the directional derivative along the u direction and perpendicular to the u direction (with the former weighted more significantly than the latter). The $||D_u x||_2$ term, then, is a measure of how smoothly

the emission profile x varies along the u direction and penalizes emission profiles that do not exhibit continuous expansion at speeds similar to the speed u . (More detail on how to construct D_u can be found in the Appendix.)

The scalar $\lambda \in \mathbb{R}$ can be interpreted as defining the “exchange rate” between units of the second objective term and units of the first objective term. That is, multiplying the second term by λ converts the measure of the smoothness objective into the units that the data fidelity objective term is measured in. Increasing the value of λ increases the relative importance of smoothness in the u direction compared to data fidelity; decreasing λ increases the relative importance of data fidelity compared to smoothness in the u direction.

The $x \succeq 0$ constraint restricts the search for emission profiles to only those profiles x that are element-wise nonnegative. Physically, the elements of x are volume photon emission rates which cannot be negative, and any x including a negative element can be immediately rejected as nonphysical.

The optimization problem (3.2) is a convex optimization problem (the objective function’s domain and epigraph are convex sets and the constraint defines a convex set), meaning that there are efficient numerical techniques for solving it [Boyd and Vandenberghe, 2004]. To solve (3.2) (or its related problem mentioned later), we use CVX, a package for specifying and solving convex programs [Grant and Boyd, 2010, 2008].

3.4.2 Noise Rejection

There is a concern with the above formulation. We can see from Figures 3.7a and 3.7b that many (probably most) of the elements of our observation vector y are likely to be pure noise (i.e., do not contain any elve signal). Most of these elements are present in the data only because of the vagaries of how we chose the start and stop time of the slice of photometric data containing our elve observation. For that reason, these elements are really irrelevant in regard to finding an ideal emission profile x , and we need not consider them.

To address this concern, we identify all the elements of y that are pure noise and

remove them from y to form y_s (where the “s” subscript stands for “signal”). Likewise, we remove the corresponding rows from A to form A_s . We can accomplish this noise removal by choosing scalar threshold values q_v and q_h for the vertical and horizontal photometric array data images Y_v and Y_h , respectively. Using these threshold values, we can define the binary image $Y_{v,\text{bin}}$ as

$$Y_{v,\text{bin}}^i = \begin{cases} 1 & \text{if } Y_v^i \geq q_v \\ 0 & \text{otherwise} \end{cases} \quad (3.3)$$

where the superscript i refers to the i th element. The binary image $Y_{h,\text{bin}}$ can be defined similarly. We form the vector $y_{\text{bin}} \in \{0, 1\}^{N_t(N_v+N_h)}$ from $Y_{v,\text{bin}}$ and $Y_{h,\text{bin}}$ in exactly the same way that we formed y from Y_v and Y_h . The binary vector y_{bin} defines which elements of our observation contain the elve signal (elements equal to 1) and which elements are pure noise (elements equal to 0). Temporarily letting I denote the set of element indexes of y_{bin} which are nonzero and letting the superscript i refer to the i th element of I , we can define our signal observation vector $y_s \in \mathbb{R}^{|I|}$ as $y_s^i = y^{I^i}$ and we can define the signal matrix $A_s \in \mathbb{R}^{|I| \times M_r M_t}$ similarly as the rows of A corresponding to nonzero entries in y_{bin} . Figure 3.11 illustrates the formation of x_s , y_s , and A_s . Furthermore, noting that y_s and A_s are composed of elements and rows (respectively) associated with either the vertical or horizontal photometer array observation, we can refer to these components by partitioning y_s and A_s as

$$y_s = \begin{bmatrix} y_{sv} \\ y_{sh} \end{bmatrix} \quad (3.4)$$

and

$$A_s = \begin{bmatrix} A_{sv} \\ A_{sh} \end{bmatrix} \quad (3.5)$$

where the “v” and “h” subscripts refer the the components associated with the vertical and horizontal photometer array observations, respectively.

Because we know which elements contain signal and which are pure noise after

looking at our observation data, we can identify elements of x that make no contribution to the signal elements of y and fix their values to zero ahead of time. We form such “region of interest” maps as

$$\begin{aligned} x_{v,ROI} &= A_{sv,bin}^T \mathbf{1} \\ x_{h,ROI} &= A_{sh,bin}^T \mathbf{1} \end{aligned} \quad (3.6)$$

where $A_{s,bin} \in \{0, 1\}^{|I| \times M_r M_t}$ is a binary version of A_s with the i th element of $A_{s,bin}$ defined as

$$A_{s,bin}^i = \begin{cases} 1 & \text{if } A_s^i > 0 \\ 0 & \text{otherwise} \end{cases} \quad (3.7)$$

and where $\mathbf{1}$ is the all-ones vector. Just as for y_s and A_s , $A_{sv,bin}$ and $A_{sh,bin}$ form a partition of $A_{s,bin}$. Each element of $x_{v,ROI}$ and $x_{h,ROI}$ is a nonnegative integer equal to the number of elements of y_{sv} or y_{sh} that that profile element makes a contribution to under the action of A_{sv} or A_{sh} . If any element of x is zero in both $x_{v,ROI}$ and $x_{h,ROI}$, then that element makes no contribution to the observed elve. We can thus define an overall binary “region of interest” map $x_{ROI,bin}$ as

$$x_{ROI,bin} = x_{v,ROI,bin} \wedge x_{h,ROI,bin} \quad (3.8)$$

where \wedge is the element-wise logical AND operator and $x_{v,ROI,bin}$ is the binary version of $x_{v,ROI}$, the i th element of which is formed predictably as

$$x_{v,ROI,bin}^i = \begin{cases} 1 & \text{if } x_{v,ROI}^i > 0 \\ 0 & \text{otherwise} \end{cases} \quad (3.9)$$

$x_{h,ROI,bin}$ is formed in the same manner.

In practice, we restrict our search of candidate photon emission profiles x to only those with zeros in the same positions as the zeros in $x_{ROI,bin}$ (or perhaps $x_{v,ROI,bin}$ if we ignore the often-noisier horizontal array data in forming the region of interest). An

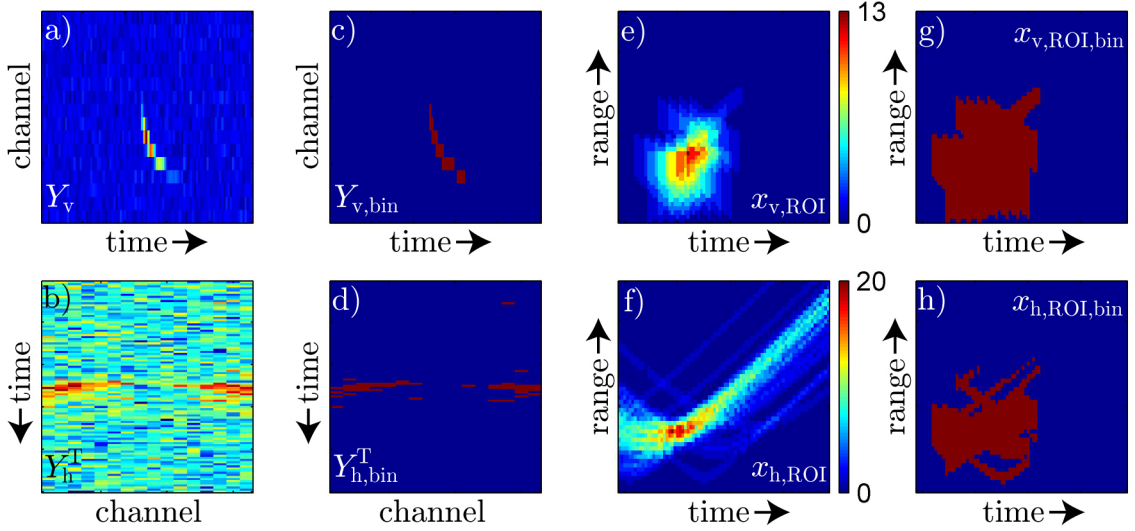


Figure 3.12: (a,b) The vertical and horizontal photometric array observation of an elve. (c,d) Thresholded versions of (a,b) which show which elements of the observation actually contain the elve signal. (e,f) The profile regions of interest, plotted in 2D. (g,h) The masks that $x_{v,ROI}$ and x_{ROI} suggest for the recovered photon emission profile.

example of the formation of the region of interest maps and the masks they suggest for the recovered photon emission profile is shown in Figure 3.12. For now, we only use $x_{ROI,bin}$ to find locations of x that can be fixed to zero before solving the optimization problem. We see in the next section that $x_{v,ROI}$ is also useful in selecting the correct matrix A (or A_s) to use for a given photometric array observation of an elve.

A side benefit of modifying the problem to reject noise as described above is that this modification makes the optimization problem considerably smaller. Typical values of N_t , N_h , N_v , M_r , and M_t result in a matrix A that is rather large: in Figure 3.12, we have $N_t = 100$, $N_h = N_v = 16$, $M_r = 50$, and $M_t = 80$ which results in a matrix A that is 3200×4000 . Because we normally have $|I| \ll N_t (N_h + N_v)$, working with y_s and A_s instead of y and A reduces the problem size significantly: in Figure 3.12, $|I| = 61$ and we have a matrix A_s that is 61×4000 . If I is determined before A is constructed, there is no need to actually construct a full matrix A and the much smaller and more useful A_s can be constructed directly, saving computation time. Furthermore, using the region of interest map to fix certain values of x to zero ahead of time is equivalent

to removing columns from A_s . In Figure 3.12, $x_{\text{ROI},\text{bin}}$ suggests that there are only 650 elements of interest in x , so the size of the optimization problem (measured by the size of A) drops from 3200×4000 to 61×650 .

3.4.3 Summary

In summary, given photometric array data of an elve in the form of two images Y_v and Y_h , one can recover an estimate of the photon emission profile of the elve as follows:

1. Choose scalar thresholds q_v and q_h and use them with Y_v and Y_h to form y_s and A_s , which represent the signal portion of the elve observation.
2. Use A_s to form $x_{\text{ROI},\text{bin}}$ (or $x_{v,\text{ROI},\text{bin}}$), which defines which elements in the emission profile make contributions to the signal portion of the elve observation.
3. Let I be the list of element positions in $x_{\text{ROI},\text{bin}}$ that have a value of zero, and solve the following convex optimization problem:

$$\begin{aligned}
 & \text{minimize} && ||y_s - A_s x||_2 + \lambda ||D_u x||_2 \\
 & \text{subject to} && x \succeq 0 \\
 & && x^i = 0, i \in I
 \end{aligned} \tag{3.10}$$

3.5 Practical Considerations in Profile Recovery

The matrix A (and A_s as well) is a function of the elve viewing geometry, and the viewing geometry must be known exactly in order to construct A without error. The dependence of A on the viewing geometry is discussed in detail in the Appendix. Here, we note that three major geometric parameters play important roles (see Figure 3.13):

- r , the range (along the ground) from the observer to the ground-location of the causative lightning return stroke
- θ , the elevation angle at which the imaging instrument is pointed

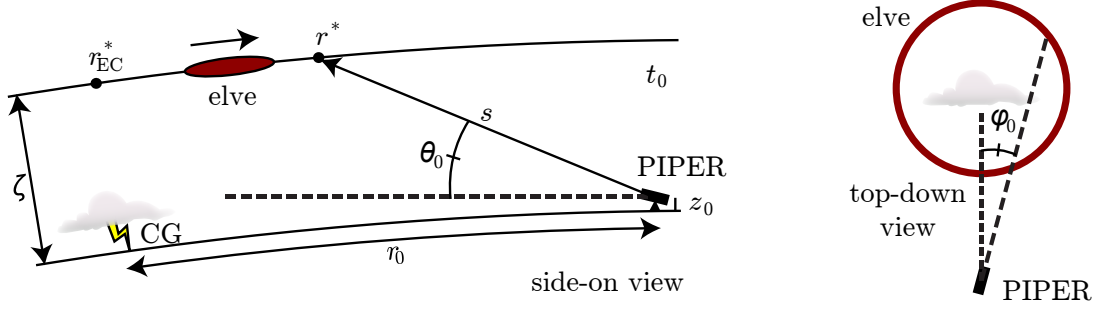


Figure 3.13: Definition of viewing geometry parameters r , θ , ϕ , and others.

- ϕ , the azimuth angle (relative to the center of the elve) at which the imaging instrument is pointed

We refer to the true values of r , θ , and ϕ for the elve under examination by 0 subscripts (r_0 , θ_0 , ϕ_0) and acknowledge that these values may not be known exactly in practice. Because the matrix A upon which our emission profile reconstruction is founded is a function of these imperfectly known parameters, it is important to study the effect that errors in the viewing geometry parameter estimates have on the quality of our resulting emission profiles and to investigate approaches for refining our estimates and reducing this error.

3.5.1 Inaccurately Known Viewing Geometry

We consider errors in the estimates of r , θ , and ϕ individually. Figure 3.14 shows the root mean square error between the reconstructed photon emission profile and the true profile for an artificially constructed elve observation (with known viewing geometry) reconstructed with an imperfectly constructed matrix A . In each case, we construct the imperfect A matrices by fixing two of the viewing geometry parameters to their correct values and varying the third to investigate its effect. For the top three traces in Figure 3.14, we used an artificial elve observation with $(r_0, \theta_0, \phi_0) = (500 \text{ km}, 11^\circ, 0^\circ)$. For the fourth trace, we used $(r_0, \theta_0, \phi_0) = (500 \text{ km}, 11^\circ, 4^\circ)$ to consider the case of an off-center viewing of an elve.

Considering the full-width half-minimum (FWHM) of each trace in Figure 3.14, we see that ϕ is the most forgiving of the three viewing geometry parameters (in both the

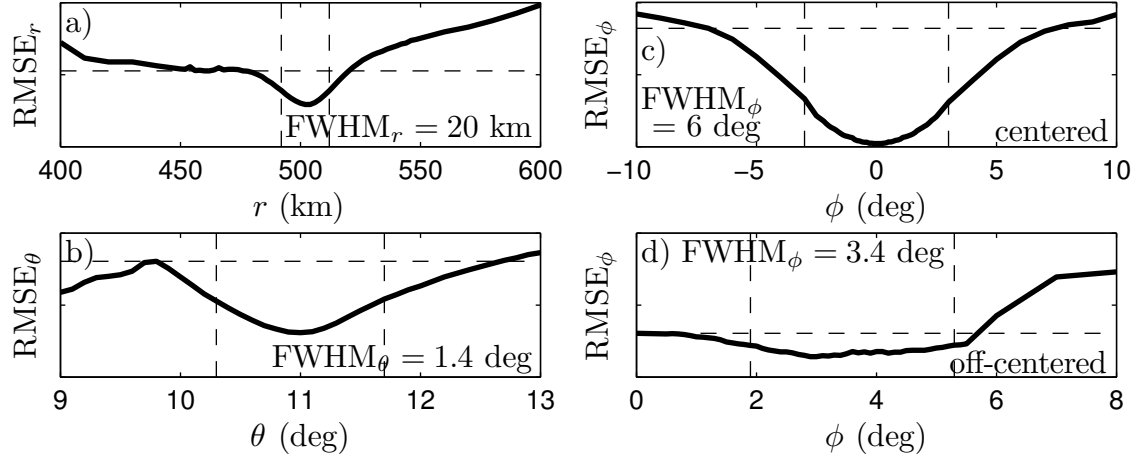


Figure 3.14: Root mean square error between the reconstructed photon emission profile and the true emission profile for imperfectly known (a) r , (b) θ , (c) ϕ in the case of centered viewing ($\phi_0 = 0^\circ$), and (d) ϕ in the case of off-centered viewing (the true $\phi_0 = 4^\circ$).

centered and off-centered cases): one needs to know ϕ to within only $FWHM_\phi/2 = 3^\circ$ of the true value ϕ_0 in the centered viewing case (and to within 1.7° in the off-centered viewing case). In horizontal PIPER photometric array data, the value of ϕ_0 can be estimated to within 1.1° as ϕ_0 denotes the location of horizontal symmetry in the data and each anode is only 1.1° wide.

For r , we have $FWHM_r = 20$ km and thus need to know the value of r_0 to within 10 km. Most lightning location networks (e.g., NLDN in the United States) can provide ground ranges to within 1 km and similar accuracy can be obtained from simultaneous VLF recordings in the absence of lightning location networks by comparing the optical and sferic arrival times [Barrington-Leigh, 2000]. Thus, while the reconstruction approach is sensitive to errors in the knowledge of r_0 , there exist several means by which r_0 may be estimated with more-than-necessary accuracy.

The imaging instrument elevation angle θ requires the most careful estimation. We see from Figure 3.14 that $FWHM_\theta = 1.4^\circ$ meaning that θ_0 must be known to within about 0.7° . Typical pan/tilt units can provide pointing elevation angle information only to within about 1° and even the most accurate units are not helpful if the elevation angle of the surface on which they are mounted is not precisely known. In

the next section, we discuss an approach for “tuning” the estimate of θ_0 from the data to improve the resulting emission profile.

3.5.2 Elevation Angle Estimation

From the discussion above, we see that θ must be chosen very carefully as differences between θ and the true value θ_0 can quickly reduce the quality of the resulting photon emission profile. In this section, we discuss the use of the elve observation data itself in choosing θ .

Earlier, we described the calculation of the emission profile “region of interest” $x_{v,ROI}$ for the purpose of finding the emission profile elements that do not contribute to the signal-carrying portions of our observation and fixing their values to zero. Each element of $x_{v,ROI}$ is a nonnegative integer equal to the number of elements in y_{sv} (the portion of the vertical photometer array observation containing the elve signal) that that profile position makes a contribution to. One can visualize $x_{v,ROI}$ and y_{sv} as in Figure 3.15: elements of y_{sv} in the elve observation (highlighted in red and outlined in white in Figure 3.15a) correspond to overlapping regions in the photon emission profile (the white outlines in Figures 3.15c and 3.15d), and $x_{v,ROI}$ is simply a count of the number of regions covering each point of the profile. As one varies the value of θ (and r and ϕ as well), these regions grow and shrink and drift in various directions and $x_{v,ROI}$ changes accordingly. If we consider only variations in θ , the regions tend to move in independent directions as θ changes, and they reach a maximum amount of overlap when $\theta = \theta_0$.

We can use $\|x_{v,ROI}\|_2$ as a measure of the amount of overlap of the signal-contributing regions in the emission profile and vary θ until $\|x_{v,ROI}\|_2$ reaches a maximum (Figure 3.15b). In Figure 3.15e, we show the results of an investigation of this approach. We construct an artificial elve observation with $\theta_0 = 11^\circ$ and attempt to determine θ_0 using the above method with candidate θ values ranging from 10° to 12° in steps of 0.05° . We repeat the test 1000 times and compile the results in a histogram. We see that all the θ_0 estimate errors are less than 0.2° , suggesting that this approach finds θ_0 to within the needed 0.7° accuracy to be useful.

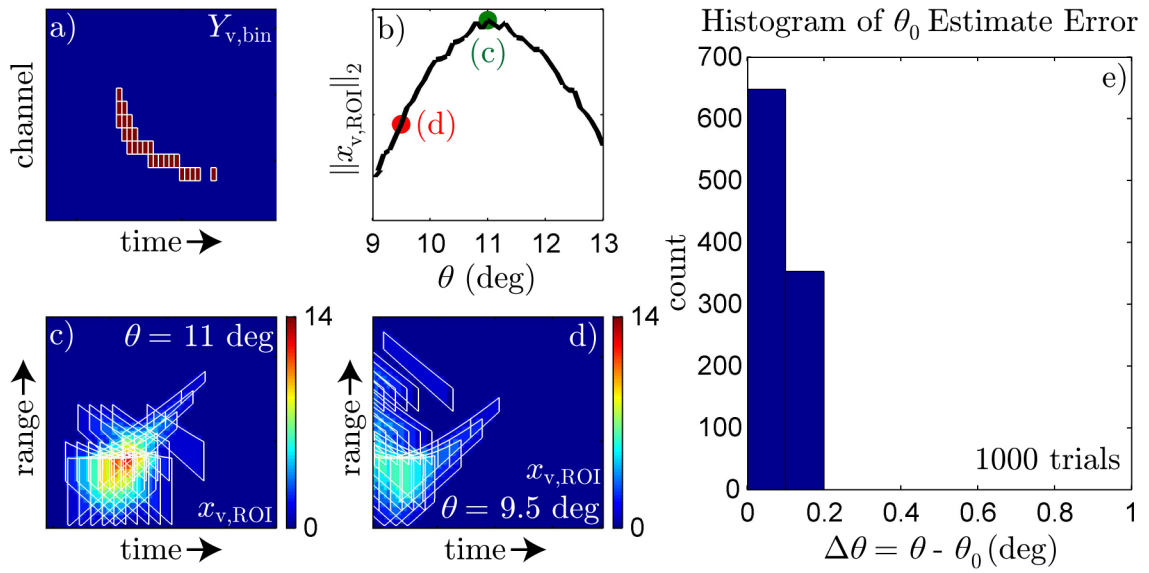


Figure 3.15: (a) $Y_{v,bin}$, the vertical portion of an example thresholded elve observation, with those elements containing the elve signal highlighted in red and outlined in white. (b) Plot of $\|x_{v,ROI}\|_2$ vs. θ for this example. (c) $x_{v,ROI}$ (plotted in 2D) for the correct viewing geometry ($\theta = \theta_0 = 11^\circ$), with the regions associated with the signal-component elements of the observation outlined. (d) Same as (c), but with $\theta = 9.5^\circ$. (e) Histogram of θ_0 estimate errors over 1000 tests (the true value of θ_0 was 11°).

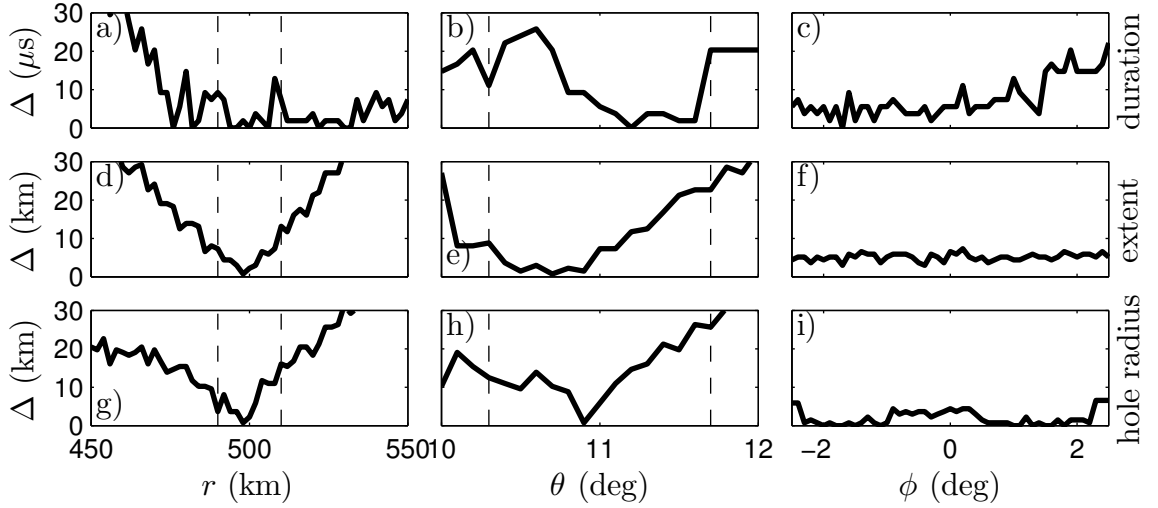


Figure 3.16: The top row (a–c) plots the error $\Delta = |\text{measured duration} - \text{actual duration}|$ as r , θ , and ϕ are varied. The middle row (d–f) and bottom row (g–i) plot the same for the radial extent and hole radius. In each plot, $\Delta = 0$ corresponds to perfect measurement of the observable under inspection, and larger Δ s correspond to larger measurement error. Vertical dotted lines denote the FWHM boundaries obtained in Figure 3.14. In all cases, the actual duration was 200 μs , the actual radial extent was 125 km, and the actual hole radius was 35 km.

3.5.3 Observable Sensitivity Analysis

In practice, the reconstructed photon emission profiles are used to measure values of elve geometry observables. The observables include, for instance, the total duration (time from start to finish), the total radial extent, and the hole radius (see Figure 3.10). We investigate the sensitivity of these three observables to imperfectly known viewing geometry in Figure 3.16. For each plot, we vary one of the three viewing geometry parameters (r , θ , or ϕ) and plot the corresponding absolute value of the error in the measured value of the observable.

We see that the error in the measured duration never exceeds 30 μs (relative to the actual duration of the example elve of 200 μs) as long as r , θ , and ϕ are known to within the FWHM intervals of Figure 3.14. The error in the measured radial extent never exceeds 25 km and is often less than 10 km (relative to the actual radial extent of 125 km). The error in the measured hole radius never exceeds 25 km and

Table 3.1: Example elve observations and their associated photon emission profiles.

event	r_0	θ_0	ϕ_0	duration	extent	hole
July 24 3:29:11	584 km	5.3°	−5°	310 μ s	160 km	20 km
July 29 6:27:30	570 km	11.0°	−4°	340 μ s	165 km	45 km
July 29 6:57:30	563 km	11.0°	−1°	320 μ s	145 km	10 km
July 29 7:27:02	445 km	11.0°	8°	480 μ s	200 km	15 km
August 2 5:45:58	657 km	4.3°	4°	280 μ s	160 km	35 km
August 2 6:04:21	678 km	4.0°	4°	380 μ s	170 km	35 km

is often less than 15 km (relative to the actual hole radius of 35 km). Clearly, the duration and extent can be measured reliably to within a few tens of μ s and tens of km, respectively. Measurement of the hole radius is more sensitive to imperfections in the assumed viewing geometry (especially in regard to the elevation angle).

3.6 Examples of Reconstructed Emission Profiles

Several PIPER elve observations and their associated reconstructed photon emission profiles are shown in Figure 3.17. All the elves were observed from Langmuir Laboratory near Socorro, New Mexico during the summer of 2008. Each row of Figure 3.17 is a separate elve observation: the left and middle columns show the vertical and horizontal PIPER observations and the right column shows the reconstructed photon emission profile. Note that the fifth vertical and horizontal photometer anodes were not functioning correctly during these nights of observation and were removed from the observation data. Table 3.1 provides associated information about the observations and profiles in Figure 3.17.

For all the elves, the range r_0 used to create the photon emission profile was obtained from NLDN. The viewing azimuth was estimated from the horizontal PIPER data, and the viewing elevation was obtained by considering $\|x_{v,ROI}\|_2$ for θ values ranging over a 2σ interval from the nominal pointing elevation recorded in the field. The measured parameters of the elve geometry obtained from the emission profile (i.e., the duration, radial extent, and initial hole radius) were obtained by considering regions of the reconstructed photon emission profile that exceed half the peak value

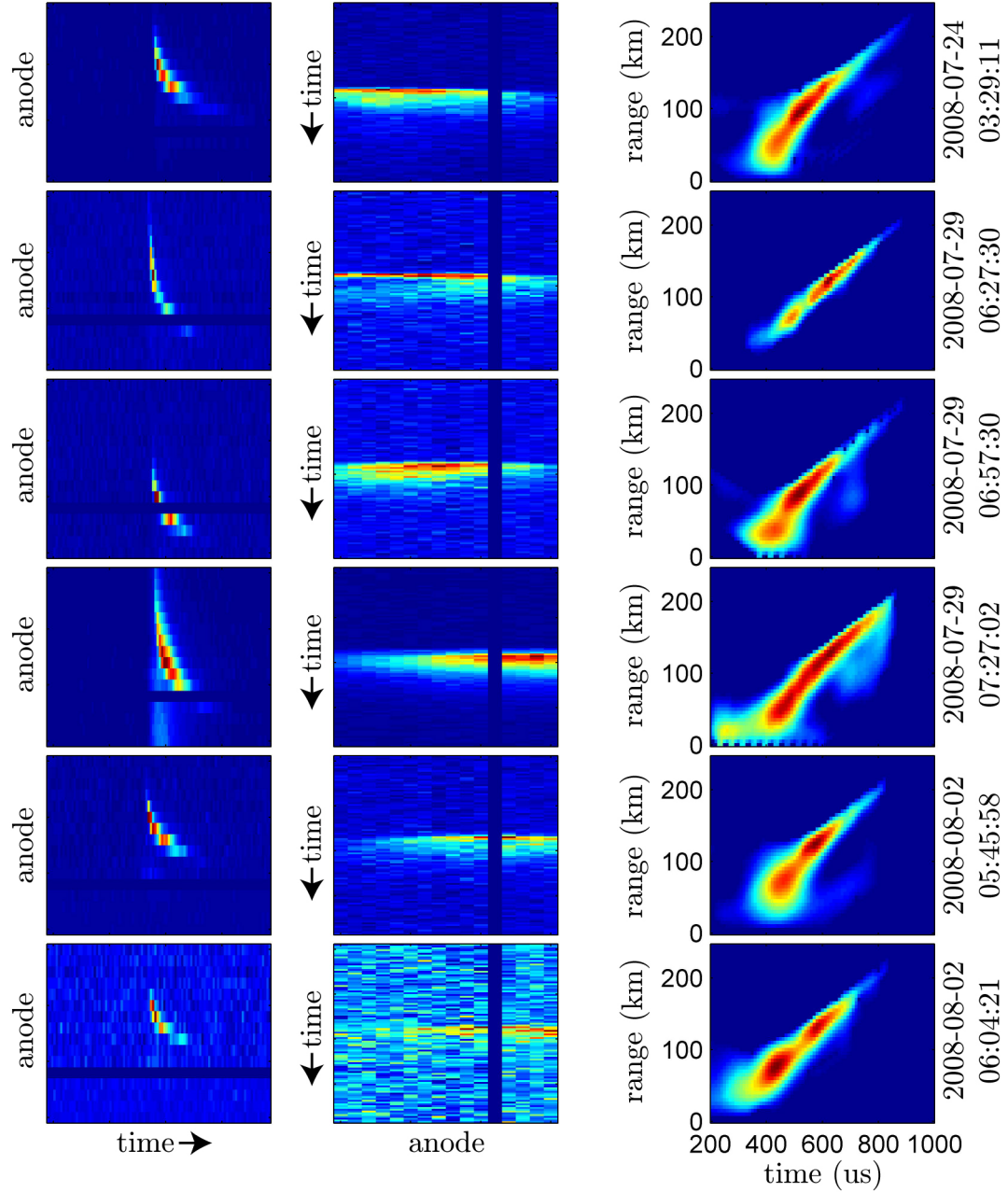


Figure 3.17: Several examples of PIPER elfe observations and their associated reconstructed photon emission profiles. Each row is a separate elfe event. (left) Vertical PIPER data. (middle) Horizontal PIPER data. (right) Reconstructed photon emission profile.

of the profile.

It is comforting to see that the θ_0 estimation approach independently converges upon the same value of θ_0 for all three elves from July 29, 2008. On that night, the PIPER instrument was repointed at 06:25 UTC and then again at 07:32 UTC and thus the value of θ_0 should not have changed during the period between repointings. PIPER was not repointed between the two events on August 2, and we see that the θ_0 estimation procedure converged to within 0.3° of the same value for both events.

In this chapter, we have introduced the PIPER photometric imaging instrument and its use in imaging elves. We have also discussed how to interpret PIPER data, introducing the concept of the photon emission profile of an elve and developing a method for recovering its estimate from PIPER data. In the next chapter, we present aggregate elve observations from three years' worth of PIPER TLE observation campaigns.

Chapter 4

Aggregate Elve Observations

In this chapter we examine three years of PIPER elve observations associated with thunderstorms in the United States Great Plains and Northern Mexico. This data set is unique among elve observation data sets because of the combination of three features of the PIPER instrument.

First, PIPER is an array of sensitive, high-speed photomultiplier tubes (as opposed to a CCD camera or a single-anode photometer). Photomultiplier tubes are considerably more sensitive than most CCD cameras and respond to light input on sub-nanosecond timescales. Very few events are missed for being too dim, and the high time resolution and arrayed nature of the PIPER instrument allow for unambiguous discrimination between elves and other TLEs (particularly elves and halos, which are easily confused in video data [*Barrington-Leigh et al.*, 2001]).

Second, PIPER is free-running (i.e., non-triggered). Because PIPER elve detection does not rely on any manual or automatic triggering mechanism, trigger bias is minimized. This feature allows PIPER to attain a more complete view of aggregate elve activity compared to related instruments that rely on triggering (e.g., the Fly’s Eye [*Inan et al.*, 1997], and other previous photometric array instruments).

Third, PIPER is ground-based, allowing it to observe storms within a 1000 km radius over their entire duration. This feature contrasts with space-based instruments (e.g., ISUAL’s Array Photometer [*Chern et al.*, 2003]), which are confined to orbital trajectories and can only sample the elve activity of a storm in the ~ 10 minute window

in which they pass over it. Space-based instruments in sun-synchronous orbits are also confined to observing storm activity at a constant local time (e.g., ISUAL only observes TLEs occurring just before local midnight due to its orbit). PIPER is free to track the same storm over several-hour periods at any time after sundown.

Throughout this chapter, we keep in mind that elve activity is the direct result of a strong lightning-induced EMP interacting with the lower ionosphere. For this reason, observed elve activity acts as a proxy measure of both strong lightning activity within storms and lightning-driven ionospheric electron density modification. In examining the elve observations of this chapter, we pursue the following two themes: (a) the statistical connection between elves and their causative lightning return strokes, and (b) the aggregate effect elves have on the lower ionosphere over time.

4.1 Observation Campaigns

The elve observations of this chapter come from four summer TLE observation campaigns. In this section, we review the equipment and data analysis techniques common to all campaigns and highlight details about each campaign individually.

4.1.1 Equipment and Techniques

The primary instrument featured in all the elve observation campaigns is the PIPER instrument. PIPER offers unambiguous detection of elves from the ground over a radius of up to ~ 1000 km.

In addition to PIPER data, we have high-resolution lightning return stroke data from the National Lightning Detection Network (NLDN) [Cummins *et al.*, 1998]. NLDN provides the latitude and longitude locations of lightning return strokes as well as calibrated estimates of their peak currents (including polarity). For regions included in our observation campaigns, the NLDN return stroke detection efficiencies are typically $\sim 90\%$ with return stroke locations accurate to within 500 m [Biagi *et al.*, 2007]. NLDN data is useful for studying the connection between observed elves and their parent CGs. For the elves observed in Northern Mexico well south of the United

States border, NLDN data is less useful as the return stroke detection efficiency falls off quickly with distance from the border.

For each campaign, we set up an AWESOME ELF/VLF receiver [[Cohen et al., 2010](#)] to record incoming VLF sferics launched by the same CGs that produce the elves. The receiver setup consists of two orthogonal air-core loop antennas to measure both horizontal components of the local wave magnetic field. The receiver is sensitive from ~ 800 Hz to 47 kHz and exhibits a linear phase response over this range of frequencies. Due to efficient sferic propagation in the Earth-ionosphere waveguide, the receiver is easily sensitive enough to detect incoming sferics originating from locations well beyond PIPER's ~ 1000 km range. The received magnetic field waveforms are digitized (with a sampling rate of 100 kHz) and recorded locally with GPS-synchronized time stamping. A more expanded discussion of the technical details of the AWESOME ELF/VLF receiver is given in [Cohen et al. \[2010\]](#).

During each campaign, we also set up a Watec WAT-902H3 Ultimate video-rate camera for live monitoring of PIPER's field of view. The camera is mounted on top of PIPER so that PIPER's field of view is contained inside the camera's $32^\circ \times 22^\circ$ field of view. Only a small number of < 2 ms events (elves and halos) recorded by PIPER simultaneously show up in the camera due to the camera's 17 ms field integration and lack of sensitivity, and the camera is primarily used to find TLEs (especially sprites) in real-time to assist in correctly centering PIPER's field of view on storms.

The PIPER instrument is mounted on a Quickset International (now Moog Quickset) QPT-90 pan/tilt unit capable of steering to any azimuthal direction and $\pm 40^\circ$ elevation angle to within 0.25° accuracy. We use real-time NLDN CG location data and live meteorological data from the National Center of Atmospheric Research (NCAR) to determine storm locations and set PIPER's pointing direction, and we use the live video feed from the Watec camera to adjust the pointing as cloud flashes and sprites are observed.

After each campaign, the recorded PIPER data is processed by automatically finding all the times in which the field of view brightens suddenly. This search is accomplished by averaging all the anodes of the vertical photometer together to create one $25000 \text{ sample-s}^{-1}$ time series and then breaking the time series into 1 ms segments.

For each 1 ms segment, the segment’s sample mean and sample standard deviation are computed. The first 10 segments of a data record are labeled “typical” and each subsequent segment is compared to the last 10 typical segments. If the segment’s sample mean is more than one standard deviation greater than the average segment-mean of the last 10 typical segments, the segment is labeled “interesting”; otherwise, it is labeled “typical”. After all the interesting segments are automatically identified, the full PIPER data corresponding to each interesting segment is examined by hand to determine if the segment contains a TLE (and what kind) or not. While the automatic labeling of interesting segments is, in some sense, a kind of trigger, the triggering threshold is low and the number of false positives is very large (10–100 times larger than the number of detected elves) and we are confident that there are no missed elve detections due to elve segments failing to be labeled interesting. Moreover, the full data set is always retained, and the labeling scheme can always be modified and the data reprocessed if there is a legitimate concern about missed events.

For elve observations that are significantly bright relative to the background, we further process them to obtain their photon emission profiles as described in Chapter 3. These profiles provide information about geometric properties of the elves that cannot be directly inferred from raw PIPER observations.

4.1.2 Yucca Ridge, 2007

The 2007 Yucca Ridge TLE observation campaign was the inaugural campaign for the PIPER instrument and lasted from June 26, 2007 to August 3, 2007. The Yucca Ridge Field Site, operated by FMA Research, Inc., has been a favorite location for TLE observation throughout the history of the field [e.g., [Lyons, 1994, 1996](#); [Fukunishi et al., 1996](#); [Inan et al., 1997](#)]. Yucca Ridge is located at an altitude of $\sim 5,700$ ft along the top of a ridge about 20 miles east of the Colorado Rocky Mountain Front Range and offers an excellent vantage point for viewing storms in the United States Great Plains to the east. Scanning across the horizon at night, the mountains block much of the view to the west and the lights of the cities of Fort Collins, Denver, and Windsor

discourage viewing to the south (although in practice we still point in those directions when needed). The rest of the horizon is reasonably dark with only occasional horizon lights sprinkled here and there. Thus, the preferred viewing directions from Yucca Ridge range from due north eastward to the south-southeast, with southerly viewing more difficult due to light pollution and westward viewing difficult because of the mountains (and, in the earlier evening hours, leftover scattered light from the setting sun).

We set up the PIPER instrument on the roof of the Yucca Ridge Field Site and an AWESOME VLF receiver in a field 1000 ft away from the site. NLDN coverage for all locations viewable from Yucca Ridge is excellent.

The campaign lasted for 39 nights although many of those nights featured cloud cover that precluded optical observation. There were 6 nights (and over 13 hours) of active storm observations in ideal sky conditions (i.e., no cloud obstruction).

4.1.3 Langmuir Lab, 2008

The 2008 Langmuir Lab TLE observation campaign lasted 30 nights from July 4, 2008 to August 3, 2008 and was conducted from Langmuir Laboratory. Langmuir Laboratory is situated atop South Baldy Peak of the Magdalena Mountains about 17 miles west of Socorro, New Mexico and is located at an elevation of $\sim 10,800$ ft (significantly higher than Yucca Ridge). Due to the high altitude, observations from Langmuir Lab are less affected by atmospheric extinction issues, making faint and more distant elves more easily detectable.

The PIPER instrument was set up along a wraparound deck/walkway on the south east side of the building just below the roof. Thus, the building itself blocked the view to the west and northwest (regions that are mostly desert and devoid of thunderstorms). Light pollution from Albuquerque to the north-northeast was a minor problem, but the rest of the horizon was very dark (very few horizon lights) and ideal for nighttime optical observation. From Langmuir Lab, one can look east and northeast into the United States Great Plains region or southwest into Northern Mexico, both of which are regions famous for their summer thunderstorm activity.

An AWESOME VLF receiver was set up in the woods 1000 ft east of the laboratory. NLDN coverage of all United States regions viewable from Langmuir is excellent. However, to the distant south and southwest (i.e., Mexico), the NLDN detection efficiency falls off dramatically due to lack of coverage beyond United States borders.

Cloud cover was again a problem during this campaign, and there were only six nights (but almost 20 hours) of ideal viewing conditions. Two of those nights (July 24, 2008 and August 2, 2008) included observations of huge elve-producing storms in Mexico outside NLDN’s primary region of coverage.

4.1.4 Yucca Ridge, 2009

In 2009 we returned to Yucca Ridge for a two-part TLE observation campaign. The first part was a manned campaign (where we were physically present to evaluate sky conditions and operate the instruments) that ran for 33 nights from June 2, 2009 to July 5, 2009. The second part was a remote campaign (where we operated the instruments remotely from Stanford and assessed sky conditions and best pointing directions from live meteorological data) that ran somewhat intermittently for 62 nights from July 8, 2009 to September 7, 2009. The manned portion of the campaign saw 13 nights (over 33 hours) of ideal storm observation while the remote portion of the campaign saw 11 nights (over 38 hours) of ideal storm observation.

For both portions of the 2009 campaign, PIPER was installed on the roof of the Yucca Ridge Field Site as in 2007. An AWESOME VLF receiver installed near Las Vegas, New Mexico (500 km south of Yucca Ridge) provided VLF sferic observations.

4.1.5 Summary

Table 4.1 summarizes the three years of TLE observation campaigns considered in this study. We observed 1644 elves over the course of the 2007, 2008, and 2009 TLE observation campaigns. About 83% of these observations come just from the 2008 Langmuir Lab campaign and the manned portion of the 2009 Yucca Ridge campaign, and 12% of these observations come from the remote campaign at Yucca Ridge in

2009. Of the 36 nights of successful elve observation (out of 164 nights total), two nights involved storms in Northern Mexico (denoted by “M” subscripts in Table 4.1). These two nights yielded 458 elves (28% of the total elve observations). NLDN coverage for elve observations made on these two nights is considerably less complete than for elve observations made from storms in the United States.

As described above, the PIPER elve observations are accompanied by other auxiliary measurements as well. We are able to associate a subset of the PIPER elve observations with NLDN stroke reports and a separate subset with unclipped VLF sferics. A third subset of the events are bright enough to allow for recovery of elve photon emission profiles. The Venn diagram of Figure 4.1 illustrates the relationship of these subsets (with area in the diagram accurately reflecting the elve count). Each additional measurement technique (NLDN, VLF sferics, and photon emission profiles) provide additional information about the elve and/or its causative CG. NLDN stroke reports provide the location of the causative CG return stroke and its peak current. A VLF sferic, if the range to the causative CG is known, provides a second measure of the return stroke peak current as the range-normalized VLF sferic magnetic field peak and return stroke peak current are well-correlated. In the absence of range information, a VLF sferic at least provides the polarity of the causative CG. If the elve is sufficiently bright relative to the background, recovery of the photon emission profile of the elve gives information about its geometry, including the radial extent, duration, and hole radius.

In the rest of this chapter, we examine the data set described in Table 4.1 in detail. In particular, we examine the distribution of elve locations, the rates of elve occurrence during storm-time scenarios, trends in elve activity over different times of the night, elve production probability dependence on CG return stroke peak current, and distributions of observed elve geometry.

4.2 Occurrence Maps

Figure 4.2 shows elve locations (inferred from the NLDN-reported locations of parent CGs) for selected nights of each of the four TLE observation campaigns. Due to

Table 4.1: Summary of three years of elve observation campaigns.

Yucca Ridge 2007: Manned 6/26/2007 to 8/3/2007 (39 nights)			Langmuir Lab 2008: Manned 7/4/2008 to 8/3/2008 (30 nights)			
Night	Elves	Duration	Night	Elves	Duration	
7/10/2007	42	1 hr, 5 min	7/24/2008 ^M	158	4 hr, 24 min	
7/16/2007	11	2 hr, 20 min	7/28/2008	2	1 hr, 6 min	
7/20/2007	-	2 hr, 12 min	7/29/2008	285	4 hr, 23 min	
7/22/2007	1	3 hr, 14 min	7/30/2008	67	2 hr, 23 min	
7/29/2007	24	2 hr, 37 min	8/1/2008	6	1 hr, 32 min	
8/2/2007	9	1 hr, 51 min	8/2/2008 ^M	300	6 hr, 7 min	
6 nights	87	13 hr, 19 min	6 nights	818	19 hr, 55 min	
Yucca Ridge 2009: Manned 6/26/2007 to 7/5/2009 (33 nights)			Yucca Ridge 2009: Remote 7/8/2009 to 9/7/2009 (62 nights)			
Night	Elves	Duration	Night	Elves	Duration	
6/6/2009	4	35 min	7/12/2009	9	2 hr, 25 min	
6/8/2009	24	2 hr, 5 min	7/14/2009	37	4 hr, 28 min	
6/14/2009	52	4 hr, 14 min	7/17/2009	-	3 hr, 53 min	
6/15/2009	12	2 hr, 5 min	7/19/2009	15	3 hr, 16 min	
6/16/2009	100	5 hr, 43 min	7/24/2009	12	2 hr, 39 min	
6/18/2009	195	3 hr, 48 min	7/26/2009	-	1 hr, 10 min	
6/22/2009	-	49 min	7/27/2009	35	5 hr, 34 min	
6/24/2009	49	3 hr, 8 min	8/1/2009	9	4 hr, 25 min	
6/25/2009	8	3 hr, 22 min	8/3/2009	32	5 hr, 20 min	
6/27/2009	88	3 hr, 27 min	8/11/2009	-	22 min	
6/30/2009	4	1 hr, 44 min	8/27/2009	47	5 hr, 5 min	
7/1/2009	7	1 hr, 49 min				
7/4/2009	-	21 min				
13 nights	543	33 hr, 10 min	11 nights	196	38 hr, 37 min	
		Manned	Remote	US	^M Mexico	Total
Nights		25	11	34	2	36
Elves		1448	196	1186	458	1644
Durations		66 hr, 24 min	38 hr, 37 min	94 hr, 30 min	10 hr, 31 min	105 hr, 1 min

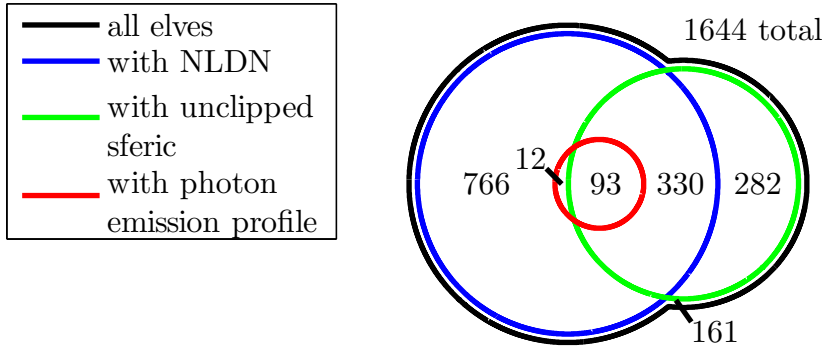


Figure 4.1: The breakdown of PIPER elve observations by which auxiliary measurements were additionally made for each event. The areas of each section are proportional to the numbers they represent.

the Rocky Mountains to the west of the Yucca Ridge site, observations are confined mainly to the United States Great Plains region (north, east, and south of Yucca Ridge). Due to field-of-view obstruction by the lab building itself, observations from Langmuir Lab are confined mainly to the southern United States Great Plains and Northern Mexico regions.

We note that the coverage area involved in ground-based observation of elves is very large. Considering just Yucca Ridge campaigns, elves are observed as close as 148 km and as far as 1008 km over 12 different states. In terms of continuous observation of night-time elve activity as a proxy measure of ionospheric D-region perturbation, it would not take many ground-based PIPER sites to provide complete coverage of the entire continental United States (or a land area of similar size). Individually, each site would be susceptible to outages due to local cloud cover (of the 102 nights of manned observation in this data set, only 25 nights saw clear skies). Collectively, outages could be reduced by overlapping neighboring ground-based PIPER site coverage areas and taking advantage of the fact that cloud coverage in one area often accompanies clear skies in other areas.

The elve locations shown in Figure 4.2 do not include events for which there is no NLDN data. Thus, elve observations from Northern Mexico are particularly underrepresented in the maps as NLDN detection efficiency falls off precipitously

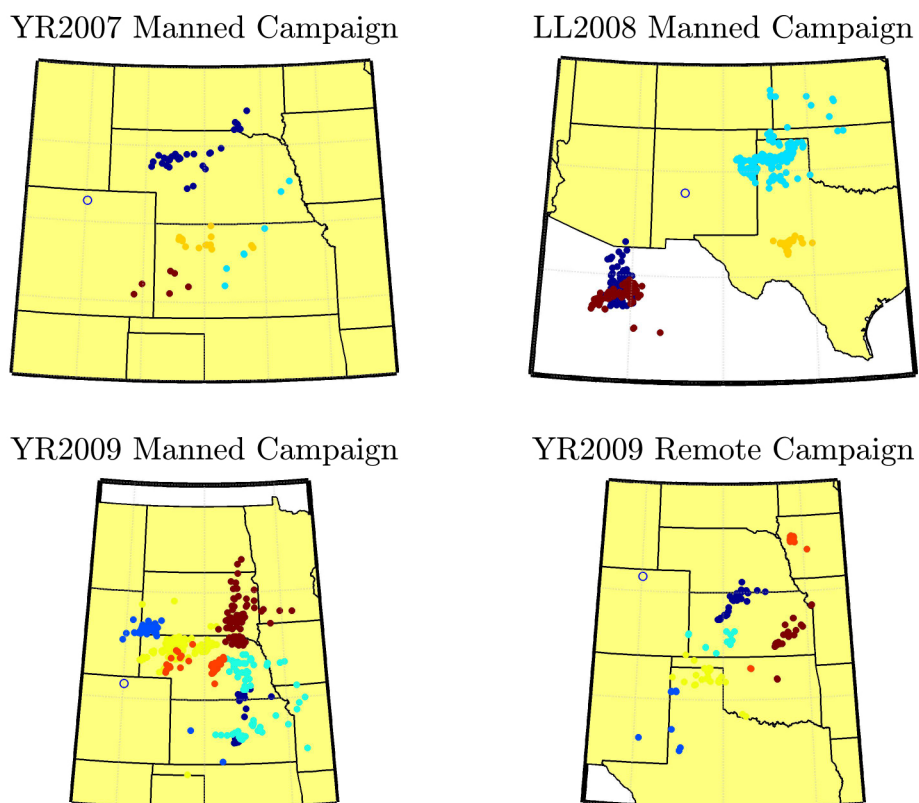


Figure 4.2: Maps of elve locations from selected nights (one color per night) of each of the four observation campaigns: the Yucca Ridge 2007 campaign, the Langmuir Lab 2008 campaign, the manned component of the Yucca Ridge 2009 campaign, and the remote component of the Yucca Ridge 2009 campaign.

more than a few hundred kilometers from the United States border. The Northern Mexico elve observations with accompanying NLDN data (plotted in the maps) are biased towards larger events closer to the United States border (so as to be detectable by NLDN) and are not as representative of the underlying lightning activity as are elve observations from the United States Great Plains. For this reason, in the following sections, if considering only the set of elve observations with accompanying NLDN reports, we normally exclude observations from the two nights of Northern Mexico viewing unless otherwise explicitly stated so as not to allow the selection bias on these nights to perturb our results.

4.3 Occurrence Rates

The maps of Figure 4.2 show that elves occur in close proximity to one another relative to the large region over which they individually affect the ionosphere. In this section, we investigate the variability in elve occurrence rates and see that elves also occur closely spaced in time (relative to the ~ 100 s or longer ionospheric relaxation time).

To date, *Chen et al.* [2008] offer the only published estimate of elve occurrence rates. Based on three years of ISUAL satellite-based TLE observations covering 81% of the Earth's surface, they estimate a globally-averaged elve occurrence rate of 3.23 elve-min⁻¹ (or 0.02 elve-min⁻¹, when normalized to the size of the effective field of view of PIPER). Due to the sun-synchronous orbit of ISUAL, this occurrence rate only considers elves occurring around local midnight. Moreover, because ISUAL cannot pause over an active storm to measure the storm-time elve occurrence rate, the reported rate must be considered a background occurrence rate to which actual storm-time occurrence rates must be compared.

To investigate the storm-time elve occurrence rates, we adopt the following notation. Consider M storms, with the i th storm involving N_i elve observations. Let $t_{i,j}$ denote the occurrence time of the j th elve in the i th storm relative to the start time of observation for the i th storm, with $1 \leq i \leq M$ and $1 \leq j \leq N_i$. Let $\Delta t_{ij} = t_{i,j+1} - t_{i,j}$ denote the wait time between elves j and $j+1$ of storm i , again with $1 \leq i \leq M$ but now with $1 \leq j \leq N_i - 1$.

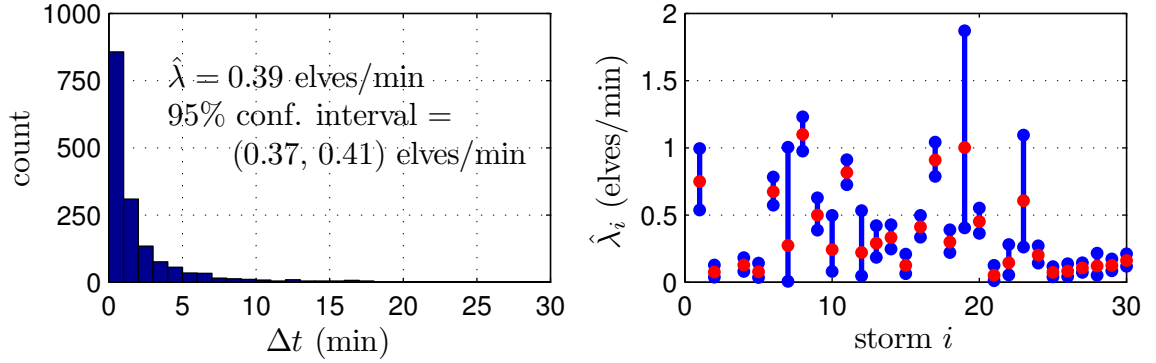


Figure 4.3: (a) Histogram of elve interarrival times over the entire three-year data set. The distribution is nearly exponential, and the maximum-likelihood estimate of its rate parameter λ is shown. (b) Rate parameter estimates and their 95% confidence intervals for elve interarrival times for each individual storm in the three-year data set.

Figure 4.3a shows a histogram of elve interarrival times Δt_{ij} accumulated over all the storms observed in this data set. Assuming the distribution of Δt is exponential (as it appears in Figure 4.3a and as is expected for any Poisson process), the maximum likelihood estimate of the distribution's rate parameter λ is $\hat{\lambda} = 0.39$ elve-min⁻¹ (about one elve every 2.5 min), with a 95% confidence interval ranging from 0.37 elve-min⁻¹ to 0.41 elve-min⁻¹. We take this value (~ 0.4 elve-min⁻¹) to be the average storm-time elve occurrence rate, and note that it is 20 times the globally-averaged background rate as reported based on ISUAL data [Chen *et al.*, 2008].

Figure 4.3b describes the storm-to-storm variability in the elve occurrence rate by plotting the maximum likelihood estimate of the rate parameter $\hat{\lambda}_i$ for each storm, along with its 95% confidence interval. We see in Figure 4.3b that there is great variability in the per-storm elve occurrence rate. Storm 21 exhibited a rate of 0.05 elve-min⁻¹ (around one elve every 19 min) averaged over a 1 hr 44 min period, while storm 8 exhibited a rate of 1.1 elve-min⁻¹ (around one elve every 55 sec) averaged over a 4 hr 23 min period. This latter rate is 55 times the globally-averaged background rate. We can conclude that storm-time elve occurrence rates are typically 20 times the globally-averaged background rate, reaching at least as high as 55 times the background rate in some storms.

As expected, the storm-time elve occurrence rate can vary considerably over the course of a storm. To consider the intra-storm variability in the elve occurrence rate, we define storm i 's elve occurrence function, $s_i(t)$, as

$$s_i(t) = \sum_j \delta(t - t_{i,j}) \quad (4.1)$$

and a window of length W , $w_W(t)$, as

$$w_W(t) = \begin{cases} \frac{1}{W} & \text{if } |t| \leq \frac{W}{2} \\ 0 & \text{otherwise} \end{cases} \quad (4.2)$$

The elve occurrence rate function of storm i at the W timescale, $r_i^W(t)$, is simply the convolution of storm i 's elve occurrence function and the window:

$$r_i^W(t) = (s_i * w_W)(t) \quad (4.3)$$

We interpret $r_i^W(t)$ as the elve occurrence rate of storm i at time t at the W timescale, and plotting $r_i^W(t)$ over time provides a view of the variability in storm i 's elve occurrence rate over its lifetime. As an example of the within-storm variability in elve rate, we plot the elve occurrence rate function at the 1-, 5-, 15-, and 60-minute timescales for the storm of August 2, 2008 in Figure 4.4. The variability is quite high. At the 5-min timescale, the rate changes from 0.4 elve-min⁻¹ (the average storm-time elve occurrence rate) to 3.8 elve-min⁻¹ (9.5 times the average storm-time rate) in a 22 min interval (from minute 176 to minute 198).

Table 4.2 shows the peak recorded storm-time elve occurrence rates at several timescales, W . For example, considering all $W=60$ min time periods, there is one 60 min time period in which 118 elves were recorded. The resulting elve occurrence rate for that period, then, is ~ 2 elve-min⁻¹, 5 times the typical storm-time rate and 100 times the globally-averaged background rate. Considering shorter time periods, the peak observed rates are even higher (the remaining rows of Table 4.2). We conclude that, considering time periods of 60 min or less, peak storm-time elve occurrence rates can be over 100 times greater than the globally-averaged background rate.

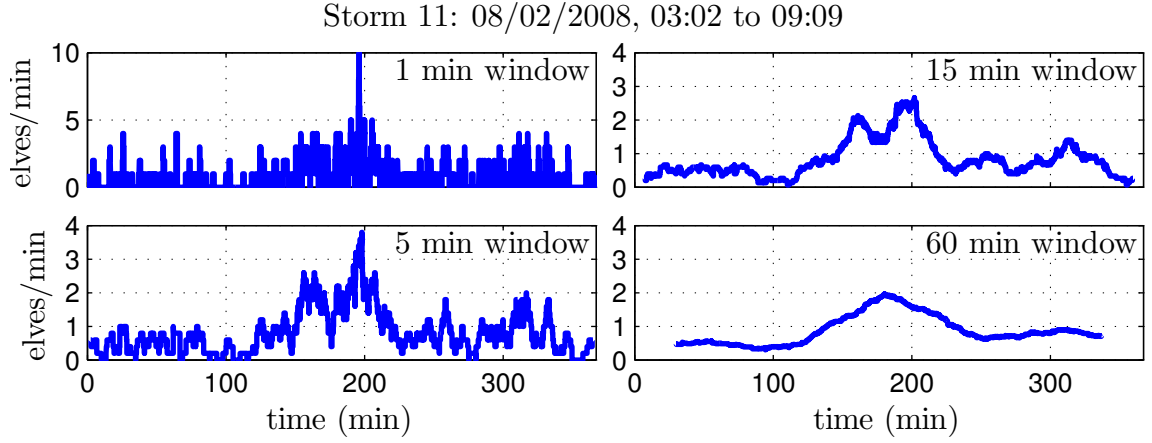


Figure 4.4: Within-storm variability in the elve occurrence rate for the storm on August 2, 2008 at the 1-, 5-, 15-, and 60-min timescales.

Table 4.2: Peak elve occurrence rates at different time scales.

W	rate	elve count	time	increase over mean	
				storm-time	global
60 min	2.0 elve-min ⁻¹	118 elves	8/2/08, 5:32–6:32	5x	100x
30 min	2.2 elve-min ⁻¹	67 elves	8/2/08, 6:00–6:30	6x	110x
15 min	2.7 elve-min ⁻¹	41 elves	6/18/09, 5:14–5:29	7x	140x
10 min	3.3 elve-min ⁻¹	33 elves	6/18/09, 5:19–5:29	8x	170x
5 min	4 elve-min ⁻¹	20 elves	6/18/09, 5:20–5:25	10x	200x
2 min	6 elve-min ⁻¹	12 elves	8/2/08, 6:16–6:18	15x	300x
1 min	10 elve-min ⁻¹	10 elves	8/2/08, 6:18–6:19	25x	500x

4.4 Elve Activity vs. Local Time of Night

The globally-averaged elve occurrence rate of $3.23 \text{ elve-min}^{-1}$ reported by [Chen et al. \[2008\]](#) and referred to in the previous section is derived from ISUAL observations. Due to its sun-synchronous polar orbit, ISUAL surveillance is confined to observation of storms along longitude lines near local midnight [[Chern et al., 2003](#)]. Ground-based observation of elves affords the opportunity to observe elve activity at non-midnight times, but most ground-based TLE observation campaigns have not been able to observe enough elves to gain a clear picture of how elve activity evolves through the night.

In this section, we examine elve occurrence as a function of the local time of night. In Figure 4.5, we present histograms of the numbers of storm observation minutes, strong CGs, and elves observed during Yucca Ridge TLE campaigns, binned by local time. At Yucca Ridge during the summer months, civil twilight (defined as times when the center of the sun is less than 6° below the horizon, providing enough light not to need artificial lighting for normal outdoor activities) ends just after 9:00 PM and begins again around 5:00 AM. In Figure 4.5a, we see that storm observation always started after 9:00 PM, peaked around 11:00 PM, and tapered off toward 4:00 AM. The strong ($|I_p| \geq 40 \text{ kA}$) CG activity within PIPER’s effective field of view (Figure 4.5b) follows the same trend. Figure 4.5c shows the number of strong CGs occurring within PIPER’s effective field of view, normalized by the number of minutes of PIPER observation. That the distribution of Figure 4.5c is rather flat suggests that PIPER, while recording at any time of night, was looking into a field of view with roughly the same rate of strong CG production at all times. (That is, PIPER was not commonly left on during “dead” times with little lightning activity.)

Figure 4.5d shows the number of elves observed at each time of night, and Figure 4.5e shows the number of elves normalized by the number of strong CGs in the field of view at each time of night. We see in Figure 4.5d that the number of elves (normalized by strong CG activity) grows through the night from 9:00 PM to 2:00 AM before falling off sharply around 3:00 AM. We also note that there seems to be a sharp increase in elve activity between 11:00 PM and 11:30 PM. While this increase may be

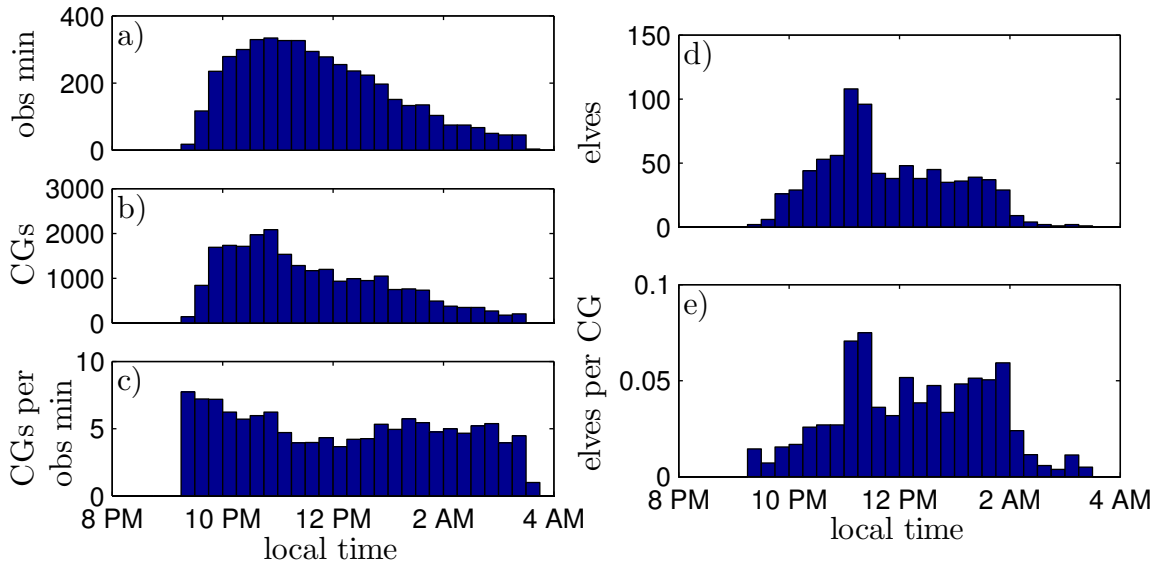


Figure 4.5: Elve activity vs. local time of night. (a) The total number of minutes of PIPER observation. (b) The number of strong ($|I_p| \geq 40$ kA) CGs within PIPER's effective field of view. (c) The number of strong CGs at each time of night, normalized by the total number of observation minutes recorded at that time of night. (d) The number of elves. (e) The number of elves observed at each time of night, normalized by the number of strong CGs at that time of night.

simply random in nature, we note that six of the 24 storms considered (6/16/2009, 6/18/2009, 6/24/2009, 7/12/2009, 7/14/2009, and 7/19/2009) all exhibited marked increases in elve activity roughly between 11:00 PM and 11:30 PM.

There are two competing effects that lead to increased or decreased elve production as the night evolves. First, the rate of strong elve-producing CGs decreases as the night wears on. Generation of strong thunderstorms is often driven by solar heating of the Earth's surface during the day and more thunderstorms develop in the middle of the day than in the middle of the night. Most nighttime thunderstorm activity is continued from thunderstorm activity in the late afternoon and early evening (as evidenced by the trend in storm-time observation minutes of Figure 4.5a). Thus, we expect the number of elves to decrease as the night progresses.

On the other hand, the ambient D-region electron density decreases as the evening progresses. Decreased D-region electron density raises the effective reflection height of the ionosphere, allowing the EMP electric field to penetrate to higher altitudes where the background neutral densities are lower and optical excitation rates per unit field are higher. Figure 2.7f illustrates this effect. An EMP propagating into each of six different nighttime ionospheric density profiles is simulated. The profiles represent progressively more attenuated ionospheres, typical of later and later times of the night. The profile of the peak reduced electric field for each profile which is representative of the N_2 1P photon production rates (see Figure 2.8) is shown. Clearly, during times in which the ionosphere is most depleted, EMP reduced electric fields achieve their highest values (through propagating up to higher altitudes with lower background neutral density) and therefore more readily produce N_2 1P photons (i.e., elves).

The net result of these two competing effects is that total elve production (averaged over many nights) rises in the early part of the night when the collapsing ionosphere effect dominates (i.e., there are still storms around to launch EMPs into the weakening ionosphere), but then falls in the latter part of the night when the effect of fewer available CGs dominates. Ignoring the aforementioned anomalous effects around 11:00 PM, Figure 4.5d illustrates this rising and then falling trend. The peak

period for total elve production appears to be just before midnight (which is coincidentally the local time sector observed by the satellite-borne ISUAL instruments). The physical reason for this anomalous peak is not clear.

The effect of the collapsing ionospheric electron density is apparent in Figure 4.5e, with elve production (on a per CG basis) 2.5 times as strong near 2:00 AM than near 9:00 PM. The implication of Figures 4.5d and 4.5e is that, in the absence of any particular observations of storms, the variance in D-region electron densities is largest earlier in the night. In the event of an observed storm at a given time, however, the variance in the D-region electron density should increase toward the end of the night.

4.5 Elve Production Probability vs. Peak Current

As seen in previous sections, storms are commonly capable of producing significant lightning EMP interaction with the lower ionosphere within small spatial regions (relative to the 100s of kilometer wide regions of each EMP's influence) and short timescales (relative to the 100s of seconds it takes for the EMP-perturbed ionosphere to relax). The bulk effect of subsequent and overlapping EMPs is significant perturbation of the lower ionosphere above a storm. The ability to monitor lightning activity within a storm over time and subsequently nowcast the state (i.e., estimate the present state) of the perturbed lower ionosphere above the storm is of particular interest.

We seek to establish an empirical relationship between some causative lightning parameter (which should be relatively easy to measure) and its perturbation effect in the lower ionosphere (which may be difficult or costly to measure). Once the relationship is established, subsequent observations of the lightning parameter and knowledge of the cause-effect relationship can be used to estimate the ionospheric perturbation effect (without having to actually measure it) for the purpose of nowcasting. Ideally, the causative lightning parameters we would like to measure are the strength and duration of the lightning's resulting EMP electric field at D-region altitudes, and the ionospheric perturbation effect we would like to record is the associated change in D-region electron density. However, both of these quantities are prohibitively difficult

to measure directly.

In practice, a number of easy-to-measure lightning parameters can be used as a proxy measure of the strength and duration of the EMP electric field at D-region altitudes. These include return stroke peak currents reported by lightning detection networks, sferic waveforms recorded on the ground, and even the brightness of a lightning return stroke. Moreover, as elves are typically the optical signature of the EMP-modification of D-region electron density, we can use elve occurrence (as detected by PIPER) as a proxy measure of EMP interaction with the lower ionosphere. In this section, we fit free-running PIPER elve observations and NLDN-reported CG peak currents to a logistic regression model of elve production probability dependence on CG peak current. Empirical development of the connection between CG peak current and elve production has not been previously possible due to the low elve detection efficiencies of previous instruments.

Consider N CGs occurring within the field of view of PIPER during its operation, and let $I_{p,i}$ denote the peak current (as reported by NLDN) of the i th CG. Let the peak current observation $X_i = f(I_{p,i})$ denote some function f of the peak current of the i th CG, and let Y_i denote whether or not the i th CG produced an elve ($Y_i = 1$ if an elve was produced and $Y_i = 0$ otherwise). We assume Y_i is a Bernoulli random variable with probability p dependent upon X_i (i.e., $Y_i \sim \text{Bern}(p(X_i))$) through the logistic model

$$p(X_i) = \frac{\exp(\beta_0 + \beta_1 X_i)}{1 + \exp(\beta_0 + \beta_1 X_i)} \quad (4.4)$$

Equation (4.4), plotted in Figure 4.6, is known as the logistic regression function and maps the input parameter space (the entire real line) to the interval $[0, 1]$. This mapping is appropriate for modeling probabilities, which cannot take values outside the interval $[0, 1]$, and motivates the use of logistic regression over more familiar types of regression (e.g., linear regression) [Chatterjee and Hadi, 2006].

Given $X = (X_1, \dots, X_N)$ and $Y = (Y_1, \dots, Y_N)$, we can calculate $f_{Y|X}$, the conditional probability density of elve occurrences Y given the peak current observations X by ordering the data such that the first q elements of Y are 1 and the remainder

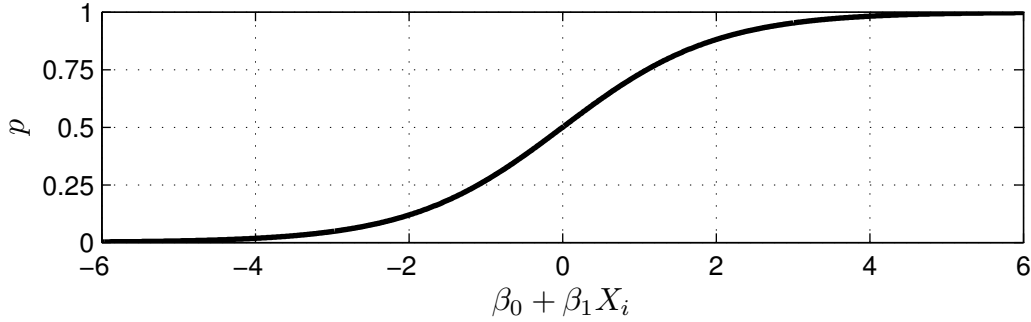


Figure 4.6: The logistic regression function

are 0:

$$f_{Y|X} = \prod_{i=1}^q p(X_i) \prod_{i=q+1}^N [1 - p(X_i)] \quad (4.5)$$

$$= \prod_{i=1}^q \frac{\exp(\beta_0 + \beta_1 X_i)}{1 + \exp(\beta_0 + \beta_1 X_i)} \prod_{i=q+1}^N \frac{1}{1 + \exp(\beta_0 + \beta_1 X_i)} \quad (4.6)$$

Defining the log-likelihood of our observations as $L = \log f_{Y|X}$ and noting it is a function of the model parameters β_0 and β_1 , we can fit the logistic model to our data by choosing model parameters that maximize L . Once we have chosen a suitable function f and its associated model parameters, we have a model for the dependence of elve production probability on causative return stroke peak current. We repeat this process twice: once for the population of +CGs and once for the population of -CGs.

We try several different functions f and evaluate the resulting model for each one using log-likelihood, retaining the choice of f for which the log-likelihood L is maximized. Table 4.3 summarizes this investigation. We see that $f(I_p) = \log|I_p|$ maximizes L in both the +CG and -CG cases and thus does the best job of describing the relationship between I_p and the probability of elve production.

Choosing $f(I_p) = \log|I_p|$, we obtain the optimal (in the maximum likelihood sense) model parameters for both CG populations (see Table 4.4). Because we have chosen

Table 4.3: Selection of the form of the peak current dependence.

$f(I_p)$	L for +CGs	L for -CGs
I_p^2	-2162	-2020
I_p	-1761	-1762
$\sqrt{ I_p }$	-1623	-1673
$\log I_p $	-1550	-1621

$X_i = \log|I_{p,i}|$, we can rewrite the model probability directly in terms of I_p as

$$p(I_p) = \frac{C|I_p|^{\beta_1}}{1 + C|I_p|^{\beta_1}} \quad (4.7)$$

where $C = \exp(\beta_0)$. We plot the dependence of the modeled probability on peak current in Figure 4.7 (the blue line) along with the empirically-observed probabilities (the black dots). The empirically-observed probabilities are tabulated by grouping all CGs into 10 kA bins and computing the ratio of the number of CGs associated with elves to the total number of CGs for each bin. For smaller peak currents, each dot represents more data points (more events fall within each 10 kA bin), while for larger peak currents, each dot represents fewer data points (only a few events fall within each 10 kA bin). Because we consider all events separately in fitting the model to our data, we expect the blue line to fit to the black dots of Figure 4.7 more tightly at smaller peak current values and less tightly at larger peak current values. Other reasons for disparity between the modeled and empirical probabilities include the fact that peak current magnitude is not the only parameter at play in elve production. Future studies of elve production probability should include other lightning parameters like received sferic strength and ionospheric parameters such as the state of the ionospheric density profile (including the presence and extent of any irregularities).

The CG data examined in Figure 4.7 includes 18 times as many -CGs as +CGs. However, only 0.08% of -CGs produce elves while 2.2% of +CGs produce elves, resulting in 61% of all elves in association with +CGs. The primary reason for the polarity asymmetry in elve production is the well-known polarity asymmetry in peak current: -CGs involve smaller peak currents (and thus typically weaker

Table 4.4: Elve production probability model parameters using $f(I_p) = \log |I_p|$.

	+CGs	−CGs
β_0	−21.2	−25.2
β_1	4.2	5.1
C	6.2×10^{-10}	1.1×10^{-11}

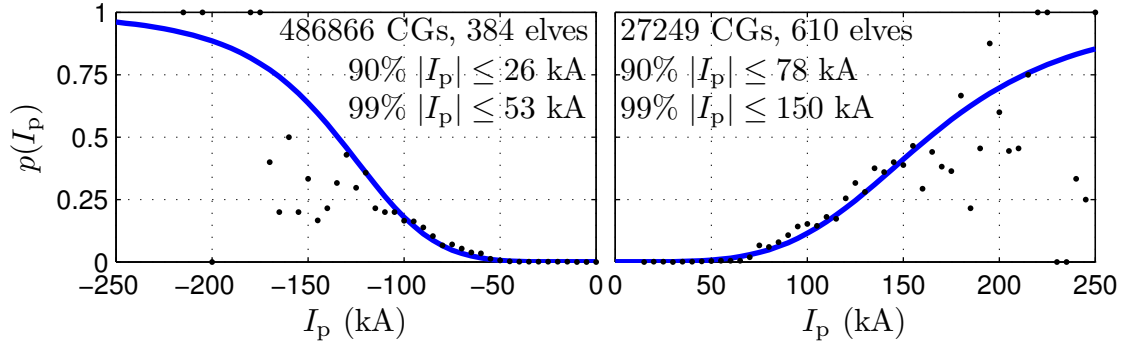


Figure 4.7: Empirically-observed elve production probabilities (dots, computed as the ratio of the count of all elve-associated CGs to the count of all CGs with peak currents within 5 km of a given value of I_p) and the modeled probability fit to the data by logistic regression (line).

radiated EMPs) than +CGs [Williams *et al.*, 2007]. Of the CGs considered, the 90th percentile −CG peak current magnitude is only 26 kA while the 90th percentile +CG peak current magnitude is 78 kA.

The polarity asymmetry runs deeper than simple differences in peak current, as evidenced by Figure 4.8 which reproduces both curves of Figure 4.7 on the same axis for direct comparison. Clearly, large peak current magnitude −CGs (albeit fewer in number) more readily produce elves than +CGs of similar peak current magnitudes, suggesting that −CG-radiated EMPs are typically stronger than +CG-radiated EMPs when CG peak current magnitude is held fixed. This result can be explained in terms of the shorter channel lengths and more impulsive channel currents of −CG return strokes. The median value of peak channel current rates of change is $12 \text{ kA-}\mu\text{s}^{-1}$ for −CGs and only $2.4 \text{ kA-}\mu\text{s}^{-1}$ for +CGs [Rakov and Uman, 2003, pp. 146, 215]. Additionally, the main negative charge layer (usually tapped by −CGs) in typical thunderclouds is several kilometers below the main positive charge layer (usually

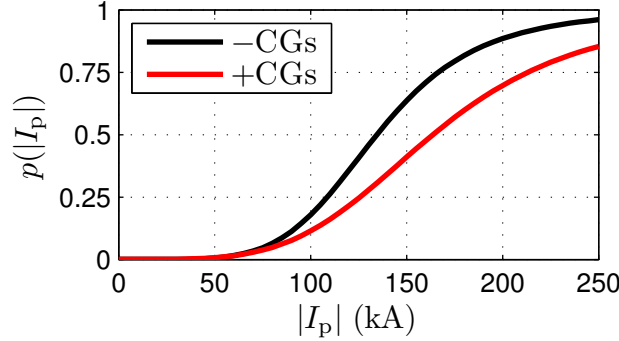


Figure 4.8: Modeled elve production probability dependence on CG peak current magnitude.

tapped by +CGs), meaning $-$ CG channel lengths are shorter than +CG channel lengths. Because shorter return stroke channels radiate fields more similar to the time rate of change of channel base current than to the channel base current itself (see Section 2.1), we expect larger $-$ CGs to radiate stronger EMPs (and more easily produce elves) than similarly-sized +CGs.

The model probabilities of Figure 4.8 represent an update and improvement to the estimated elve occurrence probabilities first presented by *Barrington-Leigh and Inan* [1999] using the Fly’s Eye instrument. The elve observation data set of *Barrington-Leigh and Inan* [1999] consisted of 73 manually-triggered 2-second observations of atmospheric “flashes” coinciding with NLDN return stroke reports. Of these 73 events, 52% were elves. Of the 34 events associated with NLDN return stroke peak current magnitudes exceeding 56 kA, all were elves. Despite the fact that the authors point out that these numbers are affected by manual instrument triggering, other researches (e.g., *Chen et al.* [2008]) have used the rule of thumb that all CGs with peak current magnitudes greater than 60 kA produce elves. Figure 4.8 provides a more realistic picture of elve production. Clearly, there are many large peak current magnitude CGs that do not produce elves (and would have necessarily been missed in the manually-triggered observations of *Barrington-Leigh and Inan* [1999]): only about 10% of 60 kA peak current magnitude CGs produce elves in our data.

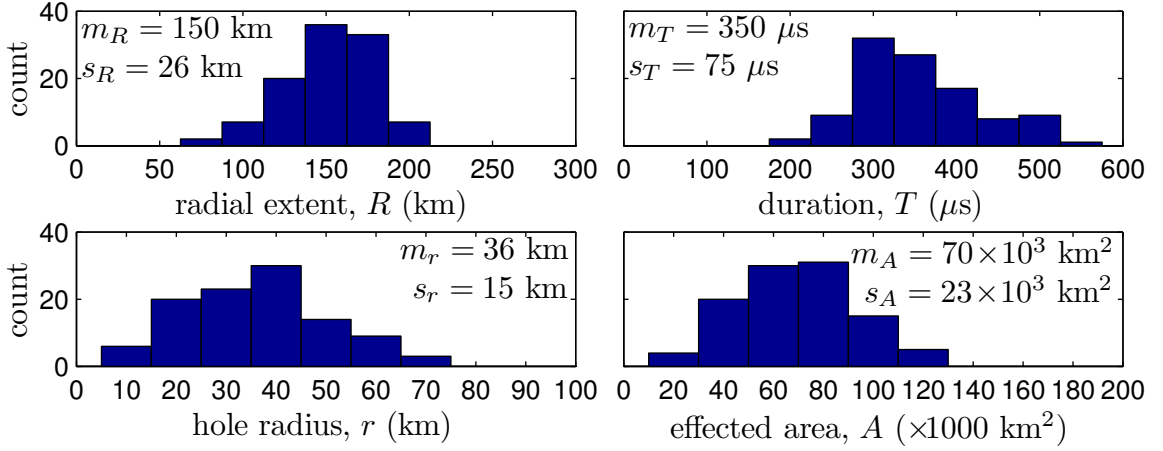


Figure 4.9: Histograms of the four geometric quantities (radial extent R , initial hole radius r , and duration T) derived from the photon emission profile estimates of 105 elves.

4.6 Geometric Parameter Distributions

We now restrict our attention to that subset of our observations for which we were able to produce an estimate of the photon emission profile. From the photon emission profile of an elve, we can directly estimate its radial extent R , initial hole radius r , and total duration T . Additionally, we can estimate the total affected area A as $A = \pi R^2 - \pi r^2$. Figure 4.9 shows histograms for these four parameters taken from a population of 105 elves for which we were able to obtain photon emission profile estimates. The sample means, m , and sample standard deviations, s , for each parameter are shown.

The 105 elves considered here span diameters ranging from 150 km to 400 km, and the mean affected area of 70×10^3 km² is larger than the State of West Virginia. As elves are typically optical signatures of EMP modification of electron density in the lower ionosphere, it is clear that a single lightning-radiated EMP can have a near-instantaneous effect on a very large region of the ionosphere.

We should stress that the geometric parameter statistics of Figure 4.9 represent only that particular subset of our elve observations for which the elve signal was very strong relative to the background noise. Practically speaking, only those events which

tend to be brighter than most or at close range are included. Less bright elves, for which photon emission profile estimation is less accurate, will no doubt include more events with smaller radial extents, shorter total durations, and smaller effected areas.

4.7 Conclusions

In this chapter, we have examined three years of bulk elve observations made by the free-running, ground-based PIPER instrument over four different elve observation campaigns. A number of features emerge:

1. Elves can be efficiently observed using ground-based photometric array instruments at up to 1000 km distances.
2. Average storm-time elve occurrence rates are ~ 20 times the globally-averaged background rate and can peak as high as several hundred times the globally-averaged background rate over few-minute periods.
3. Averaged over many nights, elve activity tends to increase toward midnight due to the post-dusk collapse of the lower ionospheric electron density and then decrease after midnight due to the decreasing amount of lightning activity available to produce elves.
4. Normalized by the level of lightning activity, the amount of elve activity tends to rise through the night, meaning a storm at 2:00 AM can produce elves (and ionospheric density perturbations) 2.5 time more readily than a similar storm at 9:00 PM.
5. A number of nights exhibit an as-yet unexplained increase in elve activity near 11:00 PM local time.
6. About 61% of elves are associated with +CGs due to the relative abundance of large +CGs (compared to -CGs).

7. Holding peak current magnitude fixed, however, $-CG$ s more readily generate elves than $+CG$ s, likely due to their more impulsive channel current waveforms and shorter channel lengths.
8. Among brighter events, average elves have radii of 150 km and affect 70×10^3 km² areas of the lower ionosphere over sub-ms timescales.

Chapter 5

Elve Doublets

5.1 Introduction

Of the 1644 elves analyzed in Chapter 4, a small subset appear to be pairs of elves occurring at the same location in rapid ($<200\ \mu\text{s}$) succession. While rare, these events were recorded in all observation campaigns and were particularly frequent during the 2008 Langmuir Laboratory campaign. In particular, for one small storm in West Texas on July 30, 2008, these events comprised over 20% of the elve observations from that storm. We refer to these events as “elve doublets” and investigate them and their potential causes in detail in this chapter.

5.2 Observations

In this section, we review the observations of elve doublets made by PIPER as well as potential observations of elve doublets made by other instruments. Additionally, we review satellite radio observations of similar (and likely related) phenomena, known as trans-ionospheric pulse pairs (TIPPs).

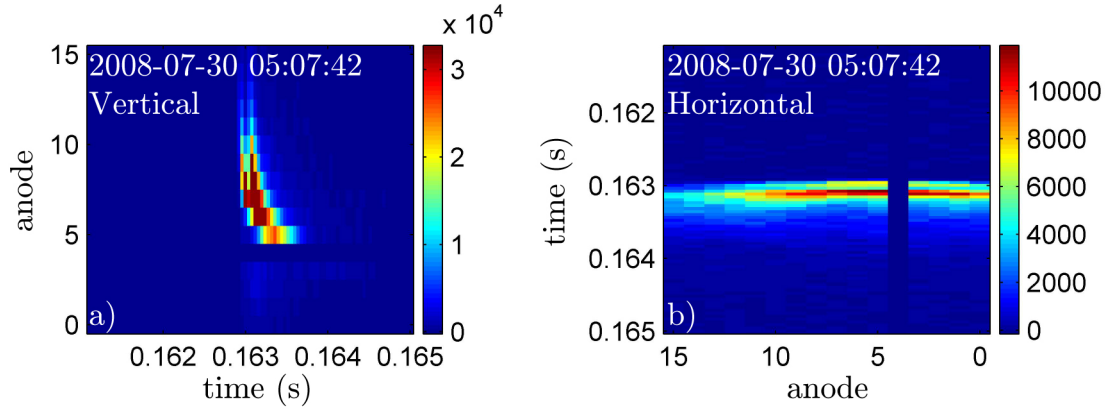


Figure 5.1: Another example of an elve doublet as observed by PIPER. (a) Vertical photometer data. (b) Horizontal photometer data. As in Figure 3.7, anode 4 of each photometer is a bad anode due to a wiring fault and can be ignored.

5.2.1 Doublets in PIPER Data

An example of an elve doublet in PIPER data is shown in Figure 3.7e,f. Another example is shown in Figure 5.1. In both cases, the vertical photometer features two elve-like down-and-to-the-right curves while the horizontal photometer features two elve-like horizontal arcs. If both curves in each photometer of each example are interpreted as the photometric signatures of outwardly expanding luminous rings, then one could interpret both examples as a pair of elves occurring less than $200 \mu\text{s}$ apart.

While doublets were observed in all campaigns, they were observed particularly frequently during the 2008 Langmuir Laboratory observation campaign. During that campaign, six storms were observed between July 24 and August 2. In terms of elve production, three of these storms (July 24, July 29, and August 2) were large storms that produced large numbers of elves, one of these storms (July 30) was a medium-sized storm, and the remaining two storms were very small. (The terms “large”, “medium”, and “small” here are used quite loosely: suffice it to say that all the “large” storms averaged more than 30 elve-hr^{-1} for at least 4 hours or more after sundown, all the “small” storms averaged less than 5 elve-hr^{-1} and lasted no longer than 2 hours after sundown, and the one “medium” storm was somewhere in

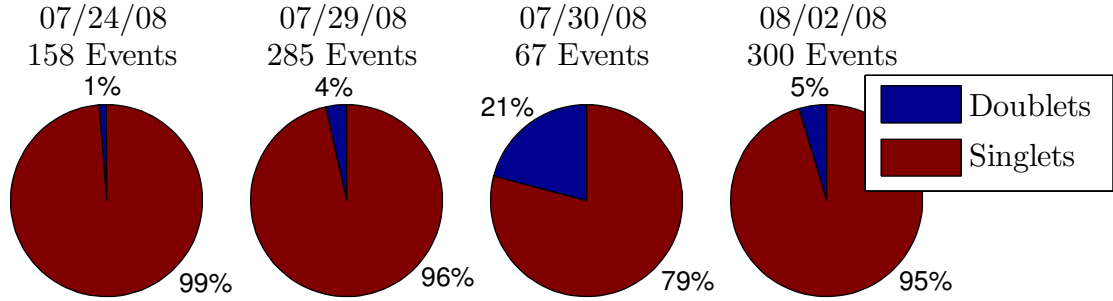


Figure 5.2: Distributions of elve singlet and elve doublet counts for four different storms during the 2008 Langmuir Laboratory elve observation campaign.

between.)

Figure 5.2 shows the distribution of elve counts for each of these storms (excluding the two small ones). In Figure 5.2 and in the rest of this chapter, we refer to traditional, lone elves as “singlets” to distinguish them from doublets. For the three largest storms of 2008 (July 24, July 29, and August 2), the singlets and doublets occur in roughly the same proportions, with elve doublets making up no more than 5% of the total elve count. In the one medium-sized storm (July 30), however, elve doublets made up 21% of all elve observations. This storm produced few sprites (only 5, compared to $\sim 30+$ for the other large storms), was considerably smaller than the other large storms in terms of physical area, and was likely not the same meteorological class of storm as the larger storms. (In other campaigns, doublets more commonly made up around 1% of the total elve observations.)

Table 5.1 further summarizes the elve observations of 2008 on a per-storm basis. In addition to the number of each category of elve observed, Table 5.1 shows the breakdown by causative CG/IC polarity (determined from received VLF sferics) and the number of events with associated NLDN reports. (Note that causative polarities for 1 singlet on July 24 and 14 singlets on August 2 could not unambiguously be determined from their sferics and are not included in the causative polarity percentage breakdowns.) The four panels of Figure 4.2 shows the geographic distribution of the elve observations for the four largest storms of the 2008 Langmuir Laboratory campaign. The blue dots correspond to the July 24 storm (in Mexico), the cyan dots

Table 5.1: Elve singlet and doublet observations by storm during the 2008 Langmuir Lab observation campaign. Count totals, breakdown by causative polarity, and counts of associated NLDN reports are reported.

Date	Elve Singlets		Elve Doublets	
	Counts (+/−)	w/NLDN	Counts (+/−)	w/NLDN
7/24/2008 ^M	156 (34%/66%)	101 (65%)	2 (0%/100%)	0 (0%)
7/28/2008	2 (50%/50%)	2 (100%)	0 (-/-)	-
7/29/2008	275 (20%/80%)	224 (82%)	10 (0%/100%)	5 (50%)
7/30/2008	53 (13%/87%)	35 (66%)	14 (0%/100%)	6 (43%)
8/1/2008	6 (17%/83%)	4 (67%)	0 (-/-)	-
8/2/2008 ^M	286 (22%/78%)	96 (34%)	14 (0%/100%)	1 (7%)

^MStorms in Mexico

correspond to the July 29 storm, the yellow dots correspond to the July 30 storm, and the blue dots correspond to the August 2 storm (in Mexico). The two elves of the July 28 storm occurred along the New Mexico-Colorado border, and the six elves of the August 1 storm occurred near the convergence of New Mexico, Arizona, and Mexico.

The causative CG/IC polarities for the elve singlets of Table 5.1 show the elve activity being dominated by negative (likely −CG) events, with positive events making up 15–30% of the total elve activity. Elve doublet events are exclusively associated with negative polarity causative discharges. Storms occurring in Mexico (July 24 and August 2) or near the Mexican border (August 1) involve lower NLDN detection rates due to lack of coverage by NLDN outside United States border. Storms well within the United States border involve high (>80%) NLDN detection rates with the notable exception of the July 30 storm that produced the unusually large percentage of elve doublets. In all cases, NLDN detection rates of discharges causing elve doublets is always considerably lower than NLDN detection rates of discharges causing normal elves. NLDN reports all 12 discharges causing elve doublets as being CGs (as opposed to ICs), and the reported peak current magnitudes are all typical of other elve-causing CGs (with the exception of one anomalously large 418.9 kA event with an unusually high χ^2 value and a polarity that did not agree with that of the VLF sferic, which we

Table 5.2: Nominal elve separations in time for elve doublet events.

Separation (μs)	Count
<60	0
60–100	6
100–140	24
140–180	10
>180	0

interpret as a misreport). NLDN never reports multiple return strokes that could be associated with a single elve doublet observation.

A total of 40 elve doublets were observed over 4 storms in 2008. From direct photometric data, the mean nominal separation in time between the elves over these 40 events is 124 μs , although PIPER’s 40 μs time resolution makes precise measurement of this value difficult. Table 5.2 summarizes the breakdown in elve separation times for elve doublet events. There are no events separated by more than 180 μs .

Figure 5.3a shows normalized VLF sferics recorded for elve events, including elve doublet events, from the July 29 storm all plotted on a single axis. The green traces are sferics associated with elve singlets, while the blue traces are sferics associated with elve doublets. Figures 5.3b–e are histograms of the peak normalized VLF values for the first four sferic peaks: the first positive peak (b), the first negative peak (c), the second positive peak (d), and the second negative peak (e). The green regions of (b–e) represent counts of non-doublet-associated sferics, while the blue regions represent counts of doublet-associated sferics.

It is clear from Figure 5.3 that sferics associated with elve doublet events are intense (in magnitude) and exhibit multiple strong initial peaks. While there are also a few examples of non-doublet sferics that are intense with multiple strong initial peaks, most are less intense in magnitude and have at most one strong initial peak. Consider the peak sferic value histograms of (b–e). For the first positive peak (b), all peak sferic values tend to be large regardless of whether they are associated with elve doublets or not. For the first negative peak (c), more non-doublet-associated sferics have lower peak values while all the doublet-associated sferic peak values remain large.

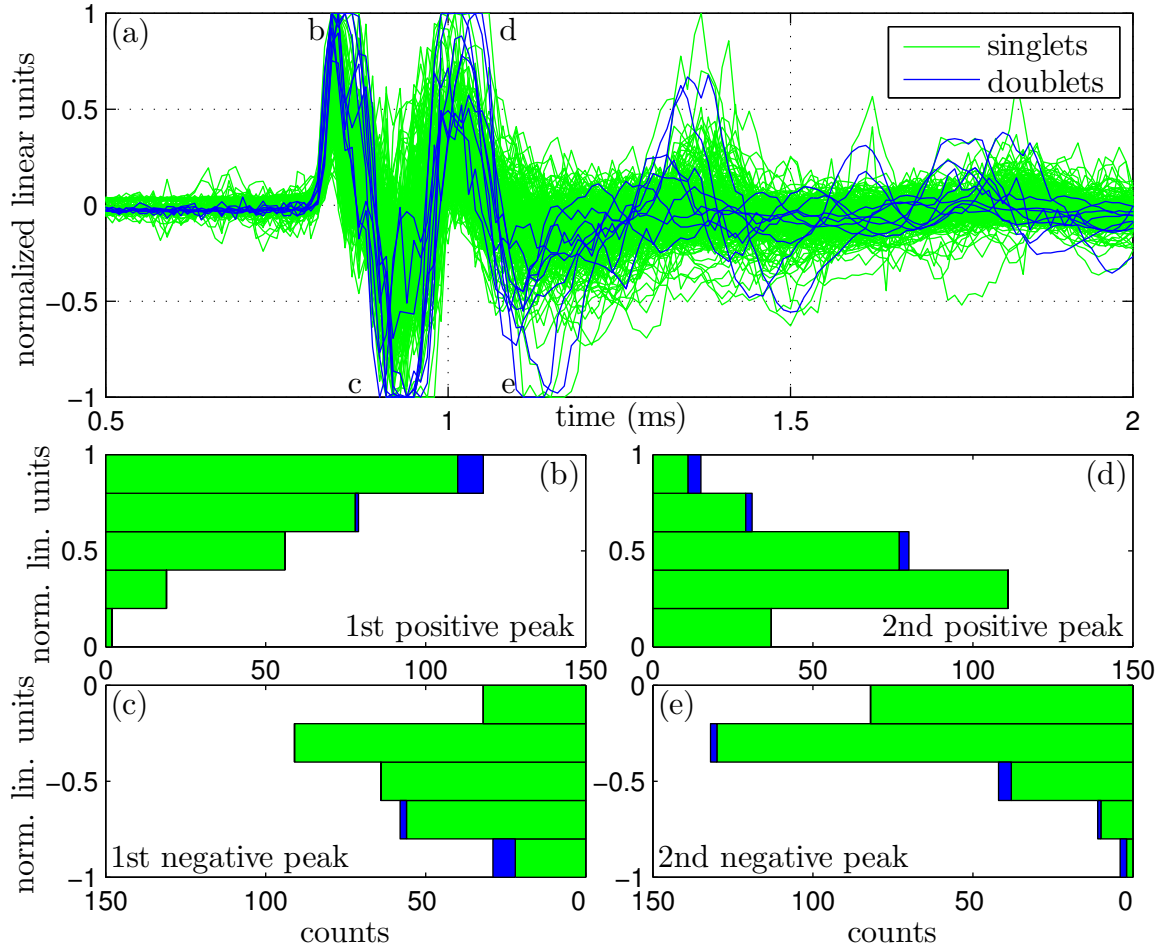


Figure 5.3: (a) Normalized VLF sferics from the July 29 storm. The green traces are sferics associated with elve singlets, and the blue traces are sferics associated with elve doublets. The amplitude axis is in normalized linear units, where -1 and $+1$ represent the maximum measurable magnetic field of the AWESOME VLF receiver. (b–e) Histograms of the peak VLF values for the first four sferic peaks: the first positive peak (b), the first negative peak (c), the second positive peak (d), and the second negative peak (e). The green regions of the histograms represent counts of non-doublet-associated sferics, while the blue regions represent counts of doublet-associated sferics. Note that the count axes on histograms (c) and (e) are reversed for effect: the zero-count locations of the four histograms occur right-to-left in the order in which the peaks occur in the sferic (first positive, first negative, second positive, and then second negative).

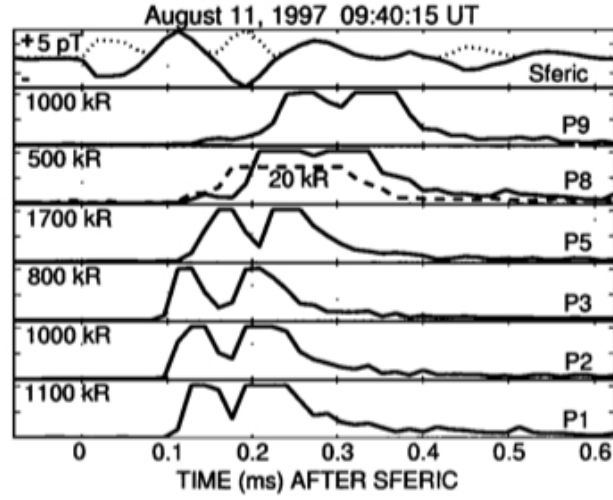


Figure 5.4: Possible observation of an elve doublet by the Fly’s Eye instrument, reproduced from Figure 2 of *Barrington-Leigh and Inan* [1999]. Time-series photometric data for red photometers P1–P3, P5, and P8–P9 (solid lines), blue photometer P12 (dashed line), and the recorded VLF sferic (top trace, solid line) and its magnitude (top trace, dotted line) are shown. Reported Rayleigh values assume all photons are either red (700 nm) or blue (400 nm).

This trend continues for the second positive peak (d) and, to a more limited degree, even for the second negative peak (e). It should be noted that the AWESOME VLF receiver used to record the sferics of Figure 5.3 does not record frequency content above 50 kHz, and future use of a VLF/LF receiver (capable of recording frequency content beyond 50 kHz) could provide more information about the lightning return strokes involved in these events.

5.2.2 The Fly’s Eye

Observations of elve doublets likely pre-date the observations we made with the PIPER instrument in 2007–2009. An “unusually bright event...showing variations in optical output...” observed by the Fly’s Eye photometer instrument was reported by *Barrington-Leigh and Inan* [1999] (and is reproduced in Figure 5.4). They suggest the event shows that “temporal fine-structure in the causative very low frequency EMP can manifest itself in the photometric record of elves.”

The event, observed from Langmuir Lab in 1997, was associated with an NLDN-reported -155 kA CG in the Texas panhandle (only 350 km north of the location of the July 30, 2008 storm observed by PIPER). The Fly’s Eye instrument consists of nine horizontally-arrayed single-anode photometers (P1–P9) behind red wavelength optical filters and three additional single-anode photometers (P10–P12) behind blue wavelength optical filters with larger fields of view overlapping the first nine photometers. The event was centered near the center of P3’s field of view. Figure 5.4 shows the time-series photometric data for the red photometers P1–P3, P5, and P8–P9 (solid lines), the blue photometer P12 (dashed line), and the recorded VLF sferic (top trace, solid) and its magnitude (top trace, dotted). The peaks of the apparent elve doublet are separated by about $80\text{ }\mu\text{s}$ (similar to PIPER elve doublet observations). The event also produced a notable amount of blue light, which was not commonly observed in elves by the Fly’s Eye instrument due to the severe atmospheric extinction blue light suffers in the lower atmosphere due to absorption and Rayleigh scattering.

5.2.3 Trans-Ionospheric Pulse Pairs

The photometric elve doublet observations described above are not the only example of observations of short-lived impulsive signals originating from thunderstorms and occurring in pairs. Since the early 1990s, satellites have frequently observed pairs of VHF radio pulses originating from thunderstorms known as trans-ionospheric pulse pairs (TIPPs). The individual pulses that make up a TIPP event are typically $10\text{ }\mu\text{s}$ long with dispersion characteristics that suggest an origin near the surface of the Earth, and the pair of pulses in a TIPP event are typically separated by $\sim 50\text{ }\mu\text{s}$ [Holden *et al.*, 1995]. Subsequent ground-based HF radio observations of sub-ionospheric pulse pairs (SIPPs) showed similar pulse widths as TIPPs, but without the dispersion and with pulse separations varying from $5\text{ }\mu\text{s}$ to $160\text{ }\mu\text{s}$, further suggesting sub-ionospheric origins [Smith and Holden, 1996]. Comparison with NLDN data showed that TIPP events frequently occur within 10 ms of NLDN reports of IC discharges [Zuelsdorf *et al.*, 1998], and detailed examination of one event showed

that the pulse separation time agreed well with the hypothesis that a single discharge event at cloud altitudes was producing the first pulse directly and the second pulse through a ground reflection [Russell *et al.*, 1998]. Subsequent detailed study of ground-based radio observations of narrow bipolar pulses (referred to as CIDs in this work) conclusively identified CIDs as the causative source mechanism for TIPP and SIPP observations [Smith *et al.*, 1999].

5.3 Investigation

In this section, we consider potential elve doublet source mechanisms. We first examine the effect of current source orientation on the photometric signature of its resulting elve. We then review two classes of source mechanisms: multiple-source mechanisms, where separate current sources account for each flash in a doublet, and ground reflection mechanisms, where a single current source and its reflection from the ground account for the two flashes in a doublet. We find that the most promising causative mechanism is a vertically-oriented discharge at cloud altitudes and its ground reflection, and we examine compact intracloud discharges (CIDs) as a likely cause.

5.3.1 Source Orientation

According to our results in Section 2.1, the radiation pattern for a vertically-oriented return stroke features a $\sin \theta$ dependence on polar angle θ , meaning that most of the radiated power is radiated outward rather than upward. For non-vertical current sources (common in IC lightning discharges), the radiation pattern is simply rotated along with the discharge’s current moment, and the radiated power is radiated both outward (in an azimuthally-dependent manner) as well as upward.

If a horizontally-oriented discharge produces an elve, the azimuth dependence of its radiation pattern causes its photometric signature in PIPER to vary with viewing position. An elve produced by a horizontal IC and viewed along the current axis of the IC would have wide horizontal extent in the horizontal photometer of PIPER.

but narrow vertical extent in its vertical photometer. Likewise, an elve produced by a horizontal IC and viewed perpendicular to the current axis of the IC would have narrow horizontal extent in PIPER's horizontal photometer and wide vertical extent in its vertical photometer. Elves produced by horizontal ICs and viewed from other directions will feature varying amounts of horizontal and vertical extent in PIPER's photometers, depending on the viewing direction.

That elve doublet observations do not exhibit much variation in the horizontal and vertical extent of their component elves suggest that their component elves are produced from vertically-oriented current sources rather than horizontally-oriented current sources. In the rest of this chapter, we consider potential causative mechanisms that feature only vertically-oriented current sources.

5.3.2 Multiple-Source Causative Mechanisms

The multiple-source class of causative mechanisms (as opposed to the reflection class of causative mechanisms) includes groups of distinct current sources which individually radiate EMPs that separately account for the elve that compose an elve doublet. Table 5.3 reviews a number of pairs of vertically-oriented current sources that may occur in a lightning discharge. Each row of Table 5.3 represents a different pair of sources. For instance, the second row considers the case of a dart leader followed by a subsequent return stroke, while the third row considers the case of a pair of subsequent return strokes. For each source, the typical duration and current involved in the source is presented, and for each pair of sources (each row of Table 5.3), the typical gap interval between the two sources in the pair is presented.

Of the pairs of sources in Table 5.3, most are immediately disqualified as a causative mechanism for elve doublets for one of a variety of reasons. First, there is no reason for the gap interval between the sources to consistently be 50–150 μs (e.g., subsequent return strokes followed by an M-components), while the gap between elves in a doublet event is consistently in the 50–150 μs range. Secondly, many of the pairs of sources include the possibility of a string of more than just two events (e.g., subsequent return strokes), but elve doublet events never include more than two elves.

Table 5.3: Potential multiple-source causative mechanisms for elve doublets.

source	duration	current	gap interval
stepped leaders return stroke	10s of ms $\sim 75 \mu\text{s}$	50-1000 A $\sim 30 \text{ kA}$	10s of μs
dart leader subsequent return stroke	1-2 ms $\sim 30 \mu\text{s}$	10-6000 A $\sim 10 \text{ kA}$	10s of μs
subsequent return strokes	$\sim 30 \mu\text{s}$	$\sim 10 \text{ kA}$	1-150 ms
subsequent return stroke M-component	$\sim 30 \mu\text{s}$ $\sim 2 \text{ ms}$	$\sim 10 \text{ kA}$ 100-200 A	up to 4 ms
K processes	$\sim 700 \mu\text{s}$	varies	$\sim 10 \text{ ms}$

Thirdly, several of the sources (e.g., K processes) are likely not strong nor impulsive enough to radiate an EMP capable of driving EMP-heating of the lower ionosphere and producing elves.

The only pair of sources in Table 5.3 that can even be considered as an elve doublet source mechanism is the dart leader-subsequent return stroke pair. However, it is not likely that dart leaders would readily generate elves, and VLF sferic recordings of elve doublet events do not suggest the involvement of leader processes. (Referring to Figure 5.3, VLF recordings of elve doublet sferics include large-amplitude peaks that are few in number—suggestive of return strokes—rather than a long series of small-amplitude short-duration peaks representative of leader steps.) Due to lack of suitable candidates, we can rule out the multiple source class of causative mechanisms for elve doublets.

5.3.3 Reflection Causative Mechanisms

The reflection class of causative mechanisms involves single current sources radiating EMPs that produce a first elve directly and a second elve through reflection from a conducting surface. This class of causative mechanism is appealing because it generally involves production of only two elves, consistent with doublet observations

which never exhibit more than two elves.

An example of a reflection source mechanism is a CG return stroke producing a direct elve in the normal way and a second elve after the initial EMP reflects from the conducting ionosphere and then again from the conducting ground. This mechanism, however, is not likely the cause of elve doublets. The reflected EMP would arrive back at the lower ionosphere a minimum of 600 μs after its initial arrival and would be severely attenuated after the first ionospheric reflection, likely unable to drive significant electron heating a second time.

A more likely reflection-type causative mechanism is a vertically-oriented, in-cloud discharge (e.g., a CID), illustrated in Figure 5.5a. A discharge at altitude z produces an EMP, the top half of which propagates directly to the lower ionosphere while the bottom half propagates to the lower ionosphere only after reflecting from the ground. The difference in arrival times Δt depends on the radial distance r of the ionospheric point considered, and Figure 5.5b illustrates the range of time separations relevant for typical cloud source altitudes and elve radii. For cloud sources between 10 km and 15 km, the expected time separations are $\sim 100 \mu\text{s}$ which is similar to those separations reported for elve doublet observations in Table 5.2. It should be noted that the VLF sferics of Figure 5.3 are not immediately consistent with this hypothesis, as one would expect only one sferic peak (made up of contributions from both the CID channel and its image) to arrive at a receiver on the ground. It is possible, then, that this hypothesis is wrong. It is also possible, however, that the sferics of Figure 5.3 are inaccurate representations of the actual sferics arriving at the receiver due to the AWESOME VLF receiver's limited ($< 50 \text{ kHz}$) frequency response. If the actual input to the VLF receiver is a sferic containing $> 50 \text{ kHz}$ frequency components (i.e., from a CID source), the presence of the receiver's low-pass filter can add a ringing effect (that is, additional peaks) to the recorded sferic output (e.g., consider a delta function input into an ideal low-pass filter, producing a sinc function). Measured sferics from an actual VLF/LF receiver are required to properly reject this hypothesis.

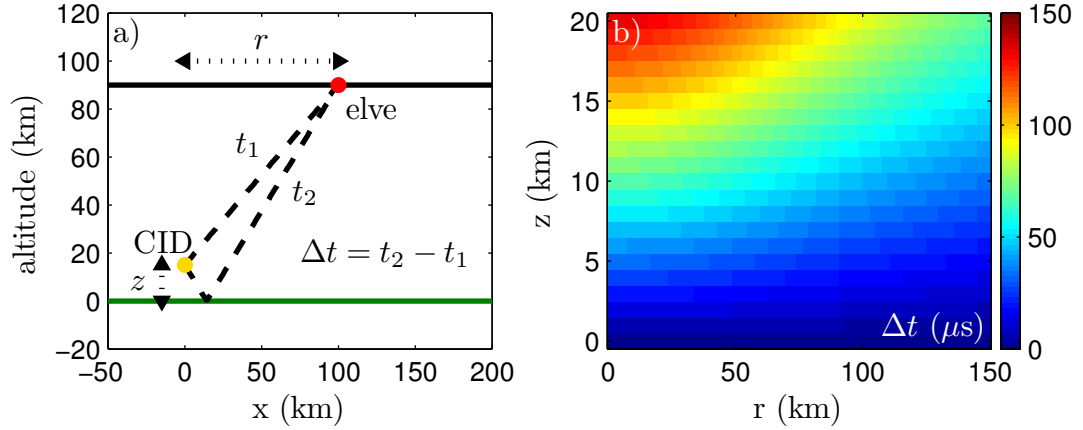


Figure 5.5: (a) IC production of an elve doublet through ground reflection. (b) Separation in arrival time of the direct and reflected EMPs at various elve radii r for various IC source altitudes z .

5.3.4 Compact Intracloud Discharges

Compact intracloud discharges, already established as the source of the suggestively similar TIPP events recorded by satellites, are a natural candidate for being the causative mechanism behind elve doublets. A recent survey of ground-based recordings of 157 CID radio emissions found a high mean CID source altitude of 16 km [Nag et al., 2010], consistent with earlier estimates from smaller observation data sets recorded on the ground (e.g., 8–11 km altitudes [e.g. Smith et al., 1999]) and in space (e.g., 6–15 km altitudes [Light and Jacobson, 2002]). From Figure 5.5b, higher source altitudes are more consistent with the typically-observed $\sim 100 \mu\text{s}$ separation between elves in doublet events.

While CIDs are the strongest known source of RF radiation in thunderstorms [Vine, 1980], they are also known to radiate strongly in the VLF/LF portion of the electromagnetic spectrum [Smith et al., 2004; Zuelsdorf et al., 2000]. While RF radiation interacts only weakly with the lower ionosphere, the VLF/LF frequency range interacts strongly with the lower ionosphere and drives the EMP-heating of free electrons, allowing CIDs to produce elves in the same way that much longer CG return strokes produce elves.

Moreover, CIDs occur at similar rates relative to strong CGs as elve doublets do

to elve singlets. CIDs typically make about about 1% of all lightning activity [[Lapp and Saylor, 2007](#)], while elve doublets typically make up 1-5% of all elve observations. Accounting for the fact that not all lightning activity produces elves, these rates are remarkably similar. Moreover, [Suszcynsky and Lay \[2009\]](#) have made observations much higher CID rates in a small, compact (lightning activity confined to an area 40 km in radius) United States Great Plains storm, similar to the July 30, 2008 storm in West Texas that produced 21% of its elve activity as elve doublets (and for which lightning activity was confined to an area ~ 50 km in radius over a 2 hr period). Generally speaking, CIDs and elve doublets exhibit similar occurrence patterns.

There are a few difficulties in assigning CIDs the role of elve doublet source, however. For instance, NLDN appears to miss lightning discharges that produce elve doublets more often than other lightning discharges (see the reduced NLDN detection rates for elve doublet events in Table 5.1). A similar phenomena has not been reported for CIDs. In fact, for the 157 CIDs studied by [Nag et al. \[2010\]](#) in Florida, 149 (95%) were correctly located and identified as ICs by NLDN.

Additionally, the sferics recorded for elve doublet events (see Figure 5.3) are not immediately suggestive of sferics recorded for CIDs by other researchers. In particular, [Smith et al. \[2002\]](#) have recorded thousands of CID sferics using the Los Alamos Sferic Array (LASA) of VLF/LF receivers. They have noted CID sferics exhibit very strong peaks (that dwarf subsequent ionospheric reflections in magnitude) and <15 μ s rise+fall times. The doublet-associated sferics of Figure 5.3 do not have either of these features.

The difference between the LASA CID sferics and our elve doublet sferics may be due to receiver differences, however. For instance, the minimum rise+fall time recordable by a 50 kHz AWESOME VLF receiver is 20 μ s, which is not small enough to resolve the rise+fall times characteristic of CID sferics. VLF/LF recordings of doublet-associated sferics are needed to clarify the existence of any differences between CID sferics and elve double sferics.

5.4 Summary

Elve doublets are a particular class of elve phenomenon consisting of two elve flashes occurring within 200 μs of each other and associated with a single lightning discharge event. In PIPER observations, elve doublets typically make up 1% to 5% of total elve observations within a storm, but in one compact storm in West Texas they made up 21% of the total activity. PIPER photometric signatures of elve doublets suggest heating by EMPs launched by vertically-oriented current source, and recorded VLF sferics associated with elve doublet events suggest the downward movement of negative charge. The mean time separation between the component elves of an elve doublet is 124 μs . Figure 2 of [Barrington-Leigh and Inan \[1999\]](#) is likely another example of an elve doublet that predates the PIPER instrument, and VHF TIPP events observed on satellites are similar in nature to elve doublets and likely share similar source mechanisms.

Compact intracloud discharges, already identified as the radiation source for VHF TIPP events, are a good candidate for being the source mechanism for elve doublets as well. CIDs are typically located at 10–15 km altitudes, resulting in direct and ground-reflected EMPs arriving at lower ionosphere altitudes $\sim 100 \mu\text{s}$ apart, consistent with elve separation times in elve doublet observations. CIDs are known to generate strong radiation at VLF/LF frequencies, making them capable of efficiently driving ionospheric electron heating. Moreover, CIDs occur at similar rates relative to other lightning activity as elve doublets occur to non-elve-doublet activity. Consistent lack of NLDN detection of lightning discharges associated with elve doublets is contrary to the CID source hypothesis, as CIDs are commonly detected by NLDN. Further VLF/LF sferic recordings will be useful in determining whether or not CIDs cause elve doublets.

Chapter 6

Summary and Suggestions for Future Work

In this work, we have presented three years of the first free-running, ground-based, high-speed observations of elves made by a novel, two-axis, multi-anode photometric array imager called PIPER. The examined data set features high-detection-efficiency recordings of bulk elve activity made over the many-hour lifetimes of elve-producing thunderstorms, as well as large-scale observations of a rarely-reported class of elve we name “elve doublets”. We have used the data set to answer a number of scientific questions about aggregate (as opposed to individual) elve activity in the United States Great Plains region. Prior elve observations have been unable to address these questions due to lack of high detection efficiency (i.e., large numbers of missed events due to missed triggers or low-speed imaging) and/or non-stationary viewing platforms (i.e., orbital trajectories unable to “pause” above an active storm to observe it over the course of its lifetime). This work represents a significant contribution to the body of elve observations and our understanding of the role bulk lightning activity plays in the lower ionosphere.

6.1 Summary

In Chapter 1 we provided the broad context in which our work is set, and in Chapter 2 we provide a detailed overview of the theory of individual elve production. Specifically, we developed the general and model-dependent features of the EMP waveform radiated by CG return strokes and described its propagation into, absorption by, and reflection from the lower ionosphere. We provided a detailed discussion of inelastic electron-neutral collision processes which serve to convey EMP energy to the background neutral population through the EMP electron heating mechanism, resulting the primary effects of electron density modification and photon production (the elve). Finally, we discussed the chemical processes that return the ionosphere back to its background state after an EMP-heating event and examined the timescales on which they take place. Much of the results of the later chapters of this work make heavy use of the facts of individual elve production and ionospheric recovery presented in Chapter 2.

In Chapter 3 we introduced the PIPER photometric array imager, providing a complete description of its construction, operation, and imaging concept complete with example data. We illustrated the difficulties encountered in interpretation of high-speed elve imagery due to the photon delay effect, and we developed the elve “photon emission profile” as an alternative presentation of high-speed elve imagery data that circumvents these difficulties. We then developed an algebraic reconstruction technique for estimating the photon emission profile of an elve directly from PIPER photometric array observations, finding that the technique is most useful in estimating an elve radial extent, initial hole radius, and temporal duration.

In Chapter 4 we examined in detail three years of PIPER elve observations. After describing the individual observation campaigns that produced the data, we studied several features of the overall data set that allowed for new insight into the nature of bulk elve activity. Specifically, we examined storm-time elve occurrence rates, finding that elves occur on average 20 times the globally-averaged background occurrence rate in storm-time scenarios. On few-minute timescales, the elve occurrence rates were seen to rise as high as several hundred times the globally-averaged background

rate. We examined average elve activity as a function of local time of night, finding that the elve activity typically peak near midnight due to the compromise of the thinning nighttime ionosphere (which allows for easier generation of elves as the night progresses) and weakening storms (which allows for fewer elve production opportunities as the night progresses). We also observed that a number of individual nights exhibit an as-yet unexplained increase in elve activity near 11:00 PM local time. We fit our elve observations and associated NLDN-reported causative CG peak current data to a logarithmic regression model and found that, holding peak current magnitude constant, $-$ CGs more readily generate elves than $+$ CGs, likely due to their more impulsive channel current and shorter channel lengths. However, as $+$ CGs produce large peak current events more often, a majority (around 60%) of elves are associated with $+$ CGs. Finally, we compiled statistics on individual elve geometries using reconstructed elve photon emission profiles to find that elve radii average 150 km and on average affect $70 \times 10^3 \text{ km}^2$ areas of the lower ionosphere over sub-millisecond timescales.

In Chapter 5 we studied our elve doublet observations in detail. Elve doublets are pairs of elves occurring within 200 μs of each other apparently in response to a single lightning discharge. The time separation between component elves averaged 124 μs , roughly consistent with an EMP resulting from a high-altitude IC discharge and its subsequent reflection from the ground. Elve doublets typically make up 1–5% of each storm’s total elve observations but made up 21% of the total elve activity in one smaller storm in West Texas. We identify CIDs as a likely causative mechanism for elve doublets due to their ideal source locations (10–15 km altitudes and even higher), efficient generation of VLF/LF radiation, similar occurrence rates, and established link to very similar TIPP events observed on-board satellites. We note, however, that NLDN misses detection of a large number of elve doublet-associated lightning discharges (which is not true for its detection of CIDs) and recorded VLF sferics associated with elve doublets are not obviously similar to recorded VLF/LF sferics associated with CIDs. More work is needed to confirm a link between elve doublets and CIDs.

6.2 Suggestions for Future Work

The work described in this dissertation suggests several avenues for future research. Broadly speaking, continued collection of PIPER elve observations will improve the quality of the data set. While this can be accomplished through more of the same manned observation campaigns, a more useful approach would involve semi-permanent unmanned observation campaigns from multiple sites in simultaneous operation. Two modifications to the existing instrument setup are required: automatic updating of the pointing direction of PIPER determined from a live feed of NLDN return stroke location reports, and inclusion of an infra-red camera and cloud-detection software for the purpose of identifying (and in turn avoiding) pointing locations obscured by cloud cover. These two improvements (combined with automated logging of pointing directions and cloud conditions) eliminate the requirement of constant human supervision in PIPER operation and allow longer observation campaigns and more consistent collection of year-round elve observations. Of course, a human will still be required in the processing and interpretation of collected PIPER data.

More immediate and concrete suggestions for future work include the following:

1. *Development of a VLF/LF receiver.* A VLF/LF receiver will allow for measuring more fully the range of sferic frequencies radiated by a lightning return stroke or CID. This may lead to possible rejection of the hypothesis that CIDs produce elve doublets if VLF/LF recordings of doublet-associated sferics do not match those associated with CIDs. Alternatively, one could coordinate PIPER observations with existing VLF/LF receiver operators (e.g., the Los Alamos Sferic Array).
2. *Improvement of time resolution of PIPER.* At $40 \mu\text{s-sample}^{-1}$, PIPER's time resolution barely resolves the pair of elves in an elve doublet and makes detailed measurement of the pair's temporal separation difficult. The temporal resolution can be immediately improved by a factor of 4 by simply removing three of the four 16-anode photometers (retaining only the red vertical photometer) and increasing the anode sampling rate from 25 kHz to 100 kHz. More accurate

measurement of the separation between elves in a doublet event can allow for more accurate estimation of the source discharge altitude.

3. *Coordination of elve observation with in-storm ionosonde operation.* Ionosonde data taken in the vicinity of an elve-producing storm would provide measurement of the during-storm buildup and post-storm relaxation of the D-region electron density in response to bulk elve activity. Ideally, having data on the elve occurrence rate of a storm and associated D-region electron density history will allow for calibration of models of EMP-ionosphere interaction. Moreover, a more complete empirical understanding of the relationship between elve activity and resulting density modification could eventually lead to accurate estimation of the state of the lower ionosphere based simply on remote observation of elve activity.

Appendix A

Photon Emission Profile Construction Details

A.1 Forming A

The matrix $A \in \mathbb{R}^{N_t(N_v+N_h) \times M_r M_t}$ produces photometric array observation data $y \in \mathbb{R}^{N_t(N_v+N_h)}$ when it multiplies a photon emission profile $x \in \mathbb{R}^{M_r M_t}$. Each column of A is the contribution to y made by the associated element of the photon emission profile x . In this section, to avoid notational collision, we continue using non-bold capitals letter for matrices and non-bold lowercase letters for scalars, but we use bold typeface for vectors.

Consider the geometry of Figure [A.1](#). We define the following quantities:

- r_0 , the range along the ground from the observing instrument to the causative return stroke.
- θ_0 , the elevation angle at which the observing instrument is pointed.
- ϕ_0 , the azimuth angle (relative to the center of the elve) at which the elevation angle is pointed.
- z_0 , the height above sea level at which the observing instrument is located (which we can often assume to be 0).

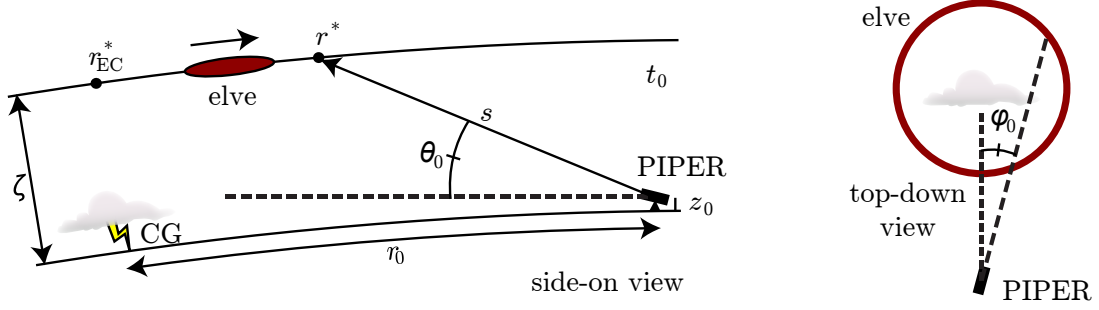


Figure A.1: Definition of viewing geometry parameters r , θ , ϕ , and others. Repeated from Figure 3.13.

- t_0 , the time at which the observing instrument measures the incoming light in its field of view.

We assume that the radius of the Earth is R_E and that the elve occurs at an altitude of ζ . We use a cartesian coordinate system centered at the center of the Earth with z pointing toward the imaging instrument and the causative return stroke confined to the x - z plane.

The elve is assumed to be confined to points whose altitude above the surface of the earth is ζ : that is, to points \mathbf{r} on the sphere where

$$\mathbf{r}^T \mathbf{r} = (R_E + \zeta)^2 \quad (\text{A.1})$$

The imaging aperture of the observing instrument (the surface on which photons are collected) has horizontal and vertical half-angular-widths of α_x and α_y , and we place the points of this surface on a coordinate system $(x', y') \in [-1, 1] \times [-1, 1]$. That is, $(-1, -1)$ denotes the lower left corner of the imaging aperture while $(1, 1)$ denotes the upper right corner. Thus, for any point (x', y') on the imaging aperture, we can define its elevation and azimuth pointing angles as

$$\begin{aligned} \theta(x', y') &= \theta_0 + y' \alpha_y \\ \phi(x', y') &= \phi_0 + x' \alpha_x \end{aligned} \quad (\text{A.2})$$

Assume the observing instrument is located at the point $\mathbf{r}_O = (0, 0, R_E + z_0)$. A ray emanating from a point (x', y') on the imaging aperture in the direction of $\theta(x', y')$ and $\phi(x', y')$ intersects, after a distance $s(x', y')$, the sphere of points on which the elve is confined (those points of altitude ζ) at a point we call $\mathbf{r}^*(x', y')$. That is,

$$\mathbf{r}^*(x', y') = \mathbf{r}_O + s(x', y') \boldsymbol{\Theta}(x', y') \quad (\text{A.3})$$

where

$$\boldsymbol{\Theta}(x', y') = \begin{bmatrix} \cos[\theta(x', y')] \cos[\phi(x', y')] \\ -\sin[\phi(x', y')] \\ \sin[\theta(x', y')] \end{bmatrix} \quad (\text{A.4})$$

is the direction dictated by the choice of x' , y' , θ_0 , ϕ_0 , α_x , and α_y .

To find $s(x', y')$, we note that $\mathbf{r}^*(x', y')$ satisfies Equation A.1. Thus, we can solve the quadratic

$$as^2 + bs + c = 0 \quad (\text{A.5})$$

with

$$\begin{aligned} a &= (\cos^2 \theta) (\cos^2 \phi) + \sin^2 \phi + \sin^2 \theta \\ b &= 2 (R_E + z_0) \sin \theta \\ c &= (R_E + z_0)^2 - (R_E + \zeta)^2 \end{aligned} \quad (\text{A.6})$$

for s . We dropped the explicit dependence of quantities on (x', y') in our notation above for brevity's sake.

We can use $s(x', y')$ to discover our aperture point (x', y') 's location in the (t, r) coordinate system of the photon emission profiles. The elve center location \mathbf{r}_{EC}^* is

$$\mathbf{r}_{\text{EC}}^* = \begin{bmatrix} (R_{\text{E}} + \zeta) \sin \frac{r_0}{R_{\text{E}}} \\ 0 \\ (R_{\text{E}} + \zeta) \sin \frac{r_0}{R_{\text{E}}} \end{bmatrix} \quad (\text{A.7})$$

and we have

$$\begin{aligned} t(x', y') &= t_0 - \frac{s(x', y')}{c} \\ r(x', y') &= (R_{\text{E}} + \zeta) \cos^{-1} \left[\frac{\mathbf{r}^*(x', y')^T \mathbf{r}_{\text{EC}}^*}{R_{\text{E}} + \zeta} \right] \end{aligned} \quad (\text{A.8})$$

In Equations A.8, we have a mapping from observing aperture space to the photon emission profile (t, r) space. To calculate the value of A_{ij} , where $1 \leq i \leq N_{\text{t}} (N_{\text{h}} + N_{\text{v}})$ is the index of a photometric array observation element and $1 \leq j \leq M_{\text{r}} M_{\text{t}}$ is the index of a photon emission profile element, do the following:

1. Partition the cathode referred to by photometer array observation element i into a large number of regions, indexed by k .
2. For each region k associated with observation element i , consider a ray emanating from the center of that region and extending out to the elve altitude. Calculate the amount of atmospheric extinction the ray experiences, τ_{ik} , as

$$\tau_{ik} = \exp \left[- \int_0^s \beta(l, x'_k, y'_k) dl \right] \quad (\text{A.9})$$

where l is the distance along the ray ($l = 0$ corresponds to the origin at the observing instrument), s is the total distance from the observing instrument to the elve location, (x'_{ik}, y'_{ik}) is the ray's starting point on the imaging aperture (which determines its direction of propagation), and $\beta(l, x'_{ik}, y'_{ik})$ is the atmospheric volume-extinction coefficient for the atmospheric altitude of a ray starting at (x'_{ik}, y'_{ik}) and propagating a distance l . For the altitude dependence

of the Rayleigh volume-scattering coefficient, we assume an exponential atmosphere with scale height $H = 7.99$ km:

$$\beta(h) = 10\beta_0 \exp\left(\frac{h}{H}\right) \quad (\text{A.10})$$

where h refers to the altitude above sea level and $\beta_0 = 4.31 \times 10^{-3} \text{ km}^{-1}$ is the Rayleigh volume-scattering coefficient at sea level. The factor of 10 reflects the assumption that Rayleigh scattering makes up around 10% of the total atmospheric extinction [[Bucholtz, 1995](#)].

3. For each region k , find the boundary of its associated region in the (t, r) space of the emission profile using Equations [A.8](#).
4. For photon emission profile element j , estimate the amount of overlap between the element's region in (t, r) space and the previously computed cathode region boundary. Refer to this quantity as η_{jik} .
5. Record the value of A_{ij} as $A_{ij} = \sum_k \eta_{jik} \tau_{ik}$.

A.2 Forming D_u

The matrix $D_u \in \mathbb{R}^{2(M_r-1)(M_t-1) \times M_r M_t}$ is used in the regularization term that promotes smoothness in reconstructed photon emission profiles along directions close to the velocity $u \in \mathbb{R}$. When x is a photon emission profile, $D_u x$ is a vector whose elements are estimates of the directional derivative of the photon emission profile along and perpendicular to the velocity u . We compute D_u by first computing matrices $D_t \in \mathbb{R}^{(M_r-1)(M_t-1) \times M_r M_t}$ and $D_r \in \mathbb{R}^{(M_r-1)(M_t-1) \times M_r M_t}$ (derivatives in the t- and r-directions) with first-order forward-differences and then assembling linear combinations of them into D_u .

Referring to the profile P (with $M_r = 3$ and $M_t = 3$) of Figure [A.2](#), we estimate the derivatives at only the shaded locations. For instance, the derivative in the t-direction of P at element 3 is

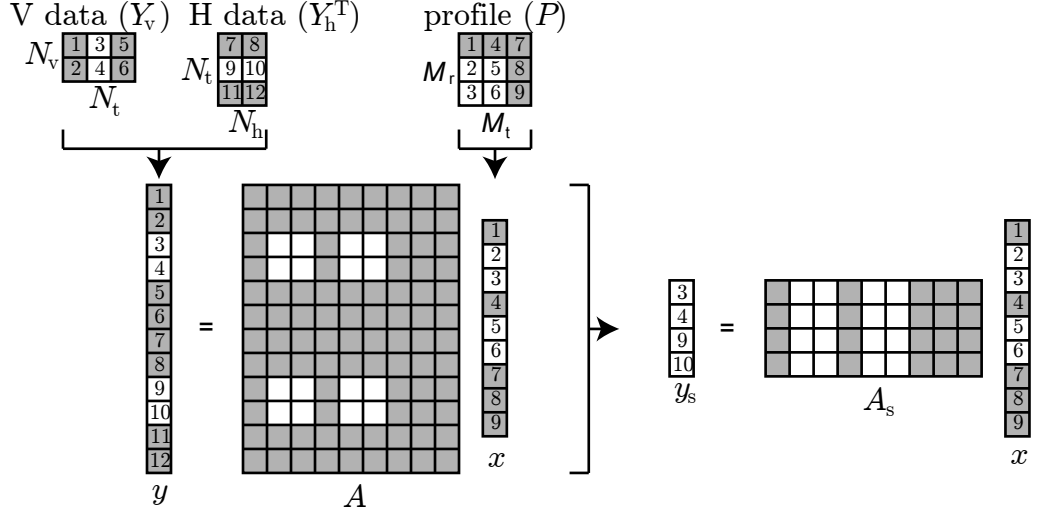


Figure A.2: Formation of x , y , and A for the case of $N_t = 3$, $N_h = N_v = 2$, and $M_r = M_t = 3$. The thresholding process was applied to y and $I = \{3, 4, 9, 10\}$ was the set of y element locations containing the elve signal; y_s and A_s were then constructed from only these elements/rows. Repeated from Figure 3.11.

$$\begin{aligned} \left. \frac{\partial P}{\partial t} \right|_3 &= \frac{1}{\Delta t} (P^6 - P^3) \\ \left. \frac{\partial P}{\partial r} \right|_3 &= \frac{1}{\Delta r} (P^2 - P^3) \end{aligned} \quad (\text{A.11})$$

We form D_t as

$$D_t = \frac{1}{\Delta t} D_{t,\text{pattern}} \otimes D_{t,\text{atom}} \quad (\text{A.12})$$

where Δt is the sampling interval of the emission profile in the t-direction, $D_{t,\text{pattern}} \in \mathbb{R}^{(M_t-1) \times M_t}$ is all zeros except for negative ones on the main diagonal and ones on the first positive diagonal, $D_{t,\text{atom}} \in \mathbb{R}^{(M_r-1) \times M_r}$ is all zeros except for ones on the first positive diagonal, and \otimes refers to the Kronecker tensor product.

We form D_r as

$$D_r = \frac{1}{\Delta r} D_{r,\text{pattern}} \otimes D_{r,\text{atom}} \quad (\text{A.13})$$

where Δr is the sampling interval of the emission profile in the r -direction, $D_{r,\text{pattern}} \in \mathbb{R}^{(M_t-1) \times M_t}$ is all zeros except for ones on the main diagonal, and $D_{r,\text{atom}} \in \mathbb{R}^{(M_r-1) \times M_r}$ is all zeros except for ones on the main diagonal and negative ones on the first positive diagonal.

Next, we use linear combinations of D_t and D_r to form matrices $D_{u,\parallel} \in \mathbb{R}^{(M_r-1)(M_t-1) \times M_r M_t}$ and $D_{u,\perp} \in \mathbb{R}^{(M_r-1)(M_t-1) \times M_r M_t}$, which estimate the directional derivatives along and perpendicular to the direction of the velocity u , respectively. Assuming u is measured in $\text{km-}\mu\text{s}^{-1}$ and that Δt is measured in μs and Δr is measured in km , we have:

$$\begin{aligned} D_{u,\parallel} &= \frac{1}{\sqrt{\left(\frac{1}{\Delta t}\right)^2 + \left(\frac{u}{\Delta r}\right)^2}} \left(\frac{1}{\Delta t} D_t + \frac{u}{\Delta r} D_r \right) \\ D_{u,\perp} &= \frac{1}{\sqrt{\left(\frac{1}{\Delta t}\right)^2 + \left(\frac{u}{\Delta r}\right)^2}} \left(\frac{-u}{\Delta r} D_t + \frac{1}{\Delta t} D_r \right) \end{aligned} \quad (\text{A.14})$$

Finally, we concatenate scalar multiples of $D_{u,\parallel}$ and $D_{u,\perp}$ to form D_u as

$$D_u = \begin{bmatrix} \sqrt{F} D_{u,\parallel} \\ \frac{1}{\sqrt{F}} D_{u,\perp} \end{bmatrix} \quad (\text{A.15})$$

where F is simply a scalar that weights the influences of the two components so that smoothness in the photon emission profile along the u direction is F times as important as smoothness perpendicular to the u direction.

Bibliography

- Barrington-Leigh, C. P., Fast photometric imaging of high altitude optical flashes above thunderstorms, Ph.D. thesis, Stanford University, Stanford, CA, 2000.
- Barrington-Leigh, C. P., and U. S. Inan, Elves triggered by positive and negative lightning discharges, *Geophys. Res. Lett.*, *26*(6), 683–686, 1999.
- Barrington-Leigh, C. P., U. S. Inan, and M. Stanley, Identification of sprites and elves with intensified video and broadband array photometry, *J. Geophys. Res.*, *106*(A2), 1741–1750, 2001.
- Biagi, C. J., K. L. Cummins, K. E. Kehoe, and E. P. Krider, National Lightning Detection Network (NLDN) performance in southern Arizona, Texas, and Oklahoma in 2003-2004, *J. Geophys. Res.*, *112*, D05208, doi:10.1029/2006JD007341, 2007.
- Bilitza, D., International Reference Ionosphere 2000, *Radio Sci.*, *36*(2), 261–275, 2001.
- Boccippio, D. J., E. R. Williams, S. J. Heckman, W. A. Lyons, I. T. Baker, and R. Boldi, Sprites, ELF transients, and positive ground strokes, *Science*, *269*(5227), 1088–1091, 1995.
- Boeck, W. L., O. H. Vaughan, R. Blakeslee, B. Vonnegut, and M. Brook, Lightning induced brightening in the airglow layer, *Geophys. Res. Lett.*, *19*(2), 99–102, 1992.
- Boyd, S., and L. Vandenberghe, *Convex Optimization*, Cambridge University Press, 2004.

- Bruce, C. E. R., and R. H. Golde, The lightning discharge, *J. Inst. Electr. Eng.*, 88(6), 487–505, 1941.
- Bucholtz, A., Rayleigh-scattering calculations for the terrestrial atmosphere, *Appl. Opt.*, 34(15), 2765–2773, 1995.
- Chatterjee, S., and A. S. Hadi, *Regression Analysis by Example*, Wiley Series in Probability and Statistics, 4 ed., John Wiley & Sons, Inc., Hoboken, New Jersey, 2006.
- Chen, A. B., et al., Global distributions and occurrence rates of transient luminous events, *J. Geophys. Res.*, 113, A08306, doi:10.1029/2008JA013101, 2008.
- Cheng, Z., S. A. Cummer, H.-T. Su, and R.-R. Hsu, Broadband very low frequency measurement of D region ionospheric perturbations caused by lightning electromagnetic pulses, *J. Geophys. Res.*, 112, A06318, doi:10.1029/2006JA011840, 2007.
- Chern, J. L., R. R. Hsu, H. T. Su, S. B. Mende, H. Fukunishi, Y. Takahashi, and L. C. Lee, Global survey of upper atmospheric transient luminous events on the ROCSAT-2 satellite, *J. Atmos. Sol.-Terr. Phys.*, 65, 647–659, doi:10.1016/S1364-6826(02)00317-6, 2003.
- Cho, M., and M. J. Rycroft, Computer simulation of the electric field structure and optical emission from cloud-top to the ionosphere, *J. Atmos. Sol.-Terr. Phys.*, 60(7-9), 871–888, 1998.
- Cho, M., and M. J. Rycroft, Non-uniform ionisation of the upper atmosphere due to the electromagnetic pulse from a horizontal lightning discharge, *J. Atmos. Sol.-Terr. Phys.*, 63(6), 559–580, 2001.
- Christian, H. J., et al., Global frequency and distribution of lightning as observed from space by the Optical Transient Detector, *J. Geophys. Res.*, 108(D1), 4005, doi:10.1029/2002JD002347, 2003.

- Cohen, M. B., U. S. Inan, and E. W. Paschal, Sensitive broadband ELF/VLF radio reception with the AWESOME instrument, *IEEE Trans. Geosci. Remote Sens.*, *48*(1), 3–17, doi:10.1109/TGRS.2009.2028334, 2010.
- Cummins, K. L., E. P. Krider, and M. D. Malone, The U.S. National Lightning Detection Network and applications of cloud-to-ground lightning data by electric power utilities, *IEEE Trans. Electromagn. Compat.*, *40*(4), 465–480, 1998.
- Eack, K. B., Electrical characteristics of narrow bipolar events, *Geophys. Res. Lett.*, *31*, L20102, doi:10.1029/2004GL021117, 2004.
- Fernsler, R. F., and H. L. Rowland, Models of lightning-produced sprites and elves, *J. Geophys. Res.*, *101*(D23), 29,653–29,662, 1996.
- Franz, R. C., R. J. Nemzek, and J. R. Winckler, Television image of a large upward electric discharge above a thunderstorm, *Science*, *249*(4964), 48–51, 1990.
- Frey, H. U., et al., Beta-type stepped leader of elve-producing lightning, *Geophys. Res. Lett.*, *32*, L13824, doi:10.1029/2005GL023080, 2005.
- Fukunishi, H., Y. Takahashi, M. Kubota, K. Sakanoi, U. S. Inan, and W. A. Lyons, Elves: Lightning-induced transient luminous events in the lower ionosphere, *Geophys. Res. Lett.*, *23*(16), 2157–2160, 1996.
- Ganot, M., Y. Yair, C. Price, B. Ziv, Y. Sherez, E. Greenburg, A. Devir, and R. Yaniv, First detection of transient luminous events associated with winter thunderstorms in the eastern Mediterranean, *Geophys. Res. Lett.*, *34*, L12801, doi:10.1029/2007GL029258, 2007.
- Gerken, E. A., U. S. Inan, and C. P. Barrington-Leigh, Telescopic imaging of sprites, *Geophys. Res. Lett.*, *27*(17), 2637–2640, 2000.
- Glukhov, V. S., and U. S. Inan, Particle simulation of the time-dependent interaction with the ionosphere of rapidly varying lightning EMP, *Geophys. Res. Lett.*, *23*(16), 2193–2196, 1996.

- Glukhov, V. S., V. P. Pasko, and U. S. Inan, Relaxation of transient lower ionospheric disturbances caused by lightning-whistler-induced electron precipitation bursts, *J. Geophys. Res.*, *97*(A11), 16,971–16,979, 1992.
- Grant, M., and S. Boyd, Graph implementations for nonsmooth convex programs, in *Recent Advances in Learning and Control (tribute to M. Vidyasagar)*, edited by V. Blondel, S. Boyd, and H. Kimura, Lecture Notes in Control and Information Sciences, pp. 95–110, Springer, 2008.
- Grant, M., and S. Boyd, CVX: Matlab software for disciplined convex programming, version 1.21, <http://cvxr.com/cvx>, 2010.
- Hale, L. C., Middle atmosphere electrical structure, dynamics and coupling, *Adv. Space Res.*, *4*(4), 175–186, 1984.
- Hamlin, T., T. E. Light, X. M. Shao, K. B. Eack, and J. D. Harlin, Estimating lightning channel characteristics of positive narrow bipolar events using intrachannel current reflection signatures, *J. Geophys. Res.*, *112*, D14108, doi:10.1029/2007JD008471, 2007.
- Hedin, A. E., Extension of the MSIS thermosphere model into the middle and lower atmosphere, *J. Geophys. Res.*, *96*(A2), 1159–1172, 1991.
- Hedin, A. E., et al., Empirical wind model for the upper, middle and lower atmosphere, *J. Atmos. Terr. Phys.*, *58*(13), 1421–1447, doi:10.1016/0021-9169(95)00122-0, 1996.
- Heidler, F., Traveling current source model for LEMP calculation, in *Proc. 6th Int. Symp. on Electromagnetic Compatibility, Zurich, Switzerland*, pp. 157–162, 1985.
- Holden, D. N., C. P. Munson, and J. C. Davenport, Satellite observations of transitionospheric pulse pairs, *Geophys. Res. Lett.*, *22*(8), 889–892, 1995.
- Inan, U. S., D. C. Shafer, W. Y. Yip, and R. E. Orville, Subionospheric VLF signatures of nighttime D region perturbations in the vicinity of lightning discharges, *J. Geophys. Res.*, *93*(A10), 1455–1472, 1988.

- Inan, U. S., T. F. Bell, and J. V. Rodriguez, Heating and ionization of the lower ionosphere by lightning, *Geophys. Res. Lett.*, *18*(4), 705–708, 1991.
- Inan, U. S., W. A. Sampson, and Y. N. Taranenko, Space-time structure of optical flashes and ionization changes produced by lightning-EMP, *Geophys. Res. Lett.*, *23*(2), 133–136, 1996.
- Inan, U. S., C. Barrington-Leigh, S. Hansen, V. S. Glukhov, T. F. Bell, and R. Rairden, Rapid lateral expansion of optical luminosity in lightning-induced ionospheric flashes referred to as ‘elves’, *Geophys. Res. Lett.*, *24*(5), 583–586, 1997.
- Karl, W. C., Regularization in image restoration and reconstruction, in *Handbook of Image and Video Processing*, edited by A. Bovik, Academic Press Series in Communications, Networking, and Multimedia, chap. 3.6, pp. 141–160, Academic Press, San Diego, CA, 2000.
- Krider, E. P., On the electromagnetic fields, Poynting vector, and peak power radiated by lightning return strokes, *J. Geophys. Res.*, *97*(D14), 15,913–15,917, 1992.
- Kuo, C.-L., et al., Modeling elves observed by FORMOSAT-2 satellite, *J. Geophys. Res.*, *112*, A11312, doi:10.1029/2007JA012407, 2007.
- Lapp, J. L., and J. R. Saylor, Correlation between lightning types, *Geophys. Res. Lett.*, *34*, L11804, doi:10.1029/2007GL029476, 2007.
- Lehtinen, N. G., and U. S. Inan, Possible persistent ionization caused by giant blue jets, *Geophys. Res. Lett.*, *34*, L08804, doi:10.1029/2006GL029051, 2007.
- Light, T. E. L., and A. R. Jacobson, Characteristics of impulsive VHF lightning signals observed by the FORTE satellite, *J. Geophys. Res.*, *107*(D24), 4756, 2002.
- Liu, X.-S., and P. R. Krehbiel, The initial streamer of intracloud lightning flashes, *J. Geophys. Res.*, *90*(D4), 6211–6218, 1985.
- Lyons, W. A., Characteristics of luminous structures in the stratosphere above thunderstorms as imaged by low-light video, *Geophys. Res. Lett.*, *21*(10), 875–878, 1994.

- Lyons, W. A., Sprite observations above the U.S. High Plains in relation to their parent thunderstorm systems, *J. Geophys. Res.*, *101*(D23), 29,641–29,652, 1996.
- Marshall, R., R. Newsome, and U. Inan, Fast photometric imaging using orthogonal linear arrays, *IEEE Trans. Geosci. Remote Sens.*, *46*(11), 3885–3893, doi:10.1109/TGRS.2008.2000824, 2008.
- Marshall, R. A., U. S. Inan, and V. S. Glukhov, Elves and associated electron density changes due to cloud-to-ground and in-cloud lightning discharges, *J. Geophys. Res.*, *115*, A00E17, doi:10.1029/2009JA014469, 2009.
- Mende, S. B., H. U. Frey, R. R. Hsu, H. T. Su, A. B. Chen, L. C. Lee, D. D. Sentman, Y. Takahashi, and H. Fukunishi, D region ionization by lightning-induced electromagnetic pulses, *J. Geophys. Res.*, *110*, A11312, doi:10.1029/2005JA011064, 2005.
- Mika, A., C. Haldoupis, T. Neubert, H. T. Su, R. R. Hsu, R. J. Steiner, and R. A. Marshall, Early VLF perturbations observed in association with elves, *Ann. Geophys.*, *24*(8), 2179–2189, 2006.
- Morgan, W. L., and B. M. Penetrante, ELENDIF: A time-dependent Boltzmann solver for partially ionized plasmas, *Comput. Phys. Comm.*, *58*(1-2), 127–152, 1990.
- Moss, G. D., V. P. Pasko, N. Liu, and G. Veronis, Monte Carlo model for analysis of thermal runaway electrons in streamer tips in transient luminous events and streamer zones of lightning leaders, *J. Geophys. Res.*, *111*, A02307, doi:10.1029/2005JA011350, 2006.
- Nag, A. V., V. A. Rakov, D. Tsalikis, and J. A. Cramer, On phenomenology of compact intracloud lightning discharges, *J. Geophys. Res.*, 2010.
- Nagano, I., S. Yagitani, K. Miyamura, and S. Makino, Full-wave analysis of elves created by lightning-generated electromagnetic pulses, *J. Atmos. Sol.-Terr. Phys.*, *65*, 615–625, doi:10.1016/S1364-6826(02)00324-3, 2003.

- Newsome, R. T., and U. S. Inan, Free-running ground-based photometric array imaging of transient luminous events, *J. Geophys. Res.*, A00E41, doi:10.1029/2009JA014834, 2010.
- Pasko, V. P., Blue jets and gigantic jets: Transient luminous events between thunderstorm tops and the lower ionosphere, *Plasma Phys. Control. Fusion*, 50(12), 124050, doi:10.1088/0741-3335/50/12/124050, 2008.
- Pasko, V. P., and U. S. Inan, Recovery signatures of lightning-associated VLF perturbations as a measure of the lower ionosphere, *J. Geophys. Res.*, 99(A9), 17,523–17,537, 1994.
- Pasko, V. P., U. S. Inan, T. F. Bell, and Y. N. Taranenko, Sprites produced by quasi-electrostatic heating and ionization in the lower ionosphere, *J. Geophys. Res.*, 102(A3), 4529–4561, 1997.
- Pasko, V. P., M. A. Stanley, J. D. Mathews, U. S. Inan, and T. G. Wood, Electrical discharge from a thundercloud top to the lower ionosphere, *Nature*, 416, 152–154, 2002.
- Peter, W. B., Quantitative measurement of lightning-induced electron precipitation using VLF remote sensing, Ph.D. thesis, Stanford University, Stanford, CA, 2007.
- Phelps, A. V., and L. C. Pitchford, Anisotropic scattering of electrons by N_2 and its effect on electron transport, *Phys. Rev. A*, 31(5), 2932–2949, 1985.
- Rakov, V. A., and M. A. Uman, *Lightning: Physics and Effects*, Cambridge University Press, Cambridge, 2003.
- Rees, M. H., *Physics and chemistry of the upper atmosphere*, Cambridge Atmospheric and Space Science Series, Cambridge University Press, New York, 1989.
- Rodger, C. J., M. Cho, M. A. Clilverd, and M. J. Rycroft, Lower ionospheric modification by lightning-EMP: Simulation of the night ionosphere over the United States, *Geophys. Res. Lett.*, 28(2), 199–202, 2001.

- Rodriguez, J. V., and U. S. Inan, Electron density changes in the nighttime D region due to heating by very-low-frequency transmitters, *Geophys. Res. Lett.*, *21*(2), 93–96, 1994.
- Rodriguez, J. V., U. S. Inan, and T. F. Bell, D region disturbances caused by electromagnetic pulses from lightning, *Geophys. Res. Lett.*, *19*(20), 2067–2070, 1992.
- Rowland, H. L., R. F. Fernsler, J. D. Huba, and P. A. Bernhardt, Lightning driven EMP in the upper atmosphere, *Geophys. Res. Lett.*, *22*(4), 361–364, 1995.
- Rowland, H. L., R. F. Fernsler, and P. A. Bernhardt, Breakdown of the neutral atmosphere in the D region due to lightning driven electromagnetic pulses, *J. Geophys. Res.*, *101*(A4), 7935–7945, 1996.
- Russell, C. T., R. S. Zuelsdorf, R. J. Strangeway, and R. Franz, Identification of the cloud pulse responsible for a trans-ionospheric pulse pair, *Geophys. Res. Lett.*, *25*(14), 2645–2648, 1998.
- Sentman, D. D., E. M. Wescott, D. L. Osborne, D. L. Hampton, and M. J. Heavner, Preliminary results from the Sprites94 aircraft campaign: 1. Red sprites, *Geophys. Res. Lett.*, *22*(10), 1205–1208, 1995.
- Smith, D. A., and D. N. Holden, Ground-based observations of subionospheric pulse pairs, *Radio Sci.*, *31*(3), 553–571, 1996.
- Smith, D. A., X. M. Shao, D. N. Holden, C. T. Rhodes, M. Brook, P. R. Krehbiel, M. Stanley, W. Rison, and R. J. Thomas, A distinct class of isolated intra-cloud lightning discharges and their associated radio emissions, *J. Geophys. Res.*, *104*(D4), 4189–4212, 1999.
- Smith, D. A., K. B. Eack, J. Harlin, M. J. Heavner, A. R. Jacobson, R. S. Massey, X. M. Shao, and K. C. Wiens, The Los Alamos Sferic Array: A research tool for lightning investigations, *J. Geophys. Res.*, *107*(D13), doi:10.1029/2001JD000502, 2002.

- Smith, D. A., M. J. Heavner, A. R. Jacobson, X. M. Shao, R. S. Massey, R. J. Sheldon, and K. C. Wiens, A method for determining intracloud lightning and ionospheric heights from VLF/LF electric field records, *Radio Sci.*, *39*, doi:10.1029/2002RS002790, 2004.
- Suszcynsky, D. M., and E. H. Lay, Case study of a strong narrow-bipolar-event-producing storm on July 2-3, 2005, Abstract AE43B-0278, AGU Fall Meeting, San Francisco, 2009.
- Takahashi, Y., R. Miyasato, T. Adachi, K. Adachi, M. Sera, A. Uchida, and H. Fukushima, Activities of sprites and elves in the winter season, Japan, *J. Atmos. Sol.-Terr. Phys.*, *65*, 551–560, doi:10.1016/S1364-6826(02)00330-9, 2003.
- Taranenko, Y. N., U. S. Inan, and T. F. Bell, Optical signatures of lightning-induced heating of the D region, *Geophys. Res. Lett.*, *19*(18), 1815–1818, 1992.
- Taranenko, Y. N., U. S. Inan, and T. F. Bell, Interaction with the lower ionosphere of electromagnetic pulses from lightning: Heating, attachment, and ionization, *Geophys. Res. Lett.*, *20*(15), 1539–1542, 1993a.
- Taranenko, Y. N., U. S. Inan, and T. F. Bell, The interaction with the lower ionosphere of electromagnetic pulses from lightning: Excitation of optical emissions, *Geophys. Res. Lett.*, *20*(23), 2675–2678, 1993b.
- Uman, M. A., and D. K. McLain, Magnetic field of lightning return stroke, *J. Geophys. Res.*, *74*(28), 6899–6910, 1969.
- Vallance-Jones, A., *Aurora*, no. 9 in Geophysics and Astrophysics Monographs, Springer-Verlag New York, LLC, New York, 1974.
- Vaughan, O. H., and B. Vonnegut, Recent observations of lightning discharges from the top of a thundercloud into the clear air above, *J. Geophys. Res.*, *94*(D11), 13,179–12,182, 1989.

- Veronis, G., V. P. Pasko, and U. S. Inan, Characteristics of mesospheric optical emissions produced by lightning discharges, *J. Geophys. Res.*, *104*(A6), 12,645–12,656, 1999.
- Vine, D. M. L., Sources of the strongest RF radiation from lightning, *J. Geophys. Res.*, *85*(C7), 4091–4095, 1980.
- Wescott, E. M., D. Sentman, D. Osborne, D. Hampton, and M. Heavner, Preliminary results from the Sprites94 aircraft campaign: 2. Blue jets, *Geophys. Res. Lett.*, *22*(10), 1209–1212, 1995.
- Wescott, E. M., D. D. Sentman, M. J. Heavner, D. L. Hampton, D. L. Osborne, and O. H. Vaughan, Blue starters: Brief upward discharges from an intense Arkansas thunderstorm, *Geophys. Res. Lett.*, *23*(16), 2153–2156, 1996.
- Willett, J. C., J. C. Bailey, and E. P. Krider, A class of unusual lightning electric field waveforms with very strong high-frequency radiation, *J. Geophys. Res.*, *94*(D13), 16,255–16,267, 1989.
- Williams, E., E. Downes, R. Boldi, W. Lyons, and S. Heckman, Polarity asymmetry of sprite-producing lightning: A paradox?, *Radio Sci.*, *42*, RS2S17, doi:10.1029/2006RS003488, 2007.
- Williams, E. R., The positive charge reservoir for sprite-producing lightning, *J. Atmos. Sol.-Terr. Phys.*, *60*(7-9), 689–692, 1998.
- Wilson, C. T. R., The electric field of a thundercloud and some of its effects, *Proc. Phys. Soc. London*, *37*, 32D–37D, 1924.
- Zuellsdorf, R. S., C. Casler, R. J. Strangeway, C. T. Russell, and R. Franz, Ground detection of trans-ionospheric pulse pairs by stations in the National Lightning Detection Network, *Geophys. Res. Lett.*, *25*(4), 481–484, 1998.
- Zuellsdorf, R. S., R. C. Franz, R. J. Strangeway, and C. T. Russell, Determining the source of strong LF/VLF TIPP events: Implications for association with NPBPs and NNBPBs, *J. Geophys. Res.*, *105*(D16), 20,725–20,736, 2000.